Politecnico di Torino

Master's Degree in Aerospace Engineering

Master's Thesis

High Angle of Attack Manoeuvrability Enhancement in Next-Generation Combat Aircraft through an All-Moving Wing Tip Concept: Aerodynamic and Control-Effectiveness Assessment

Andrea De Marino

331759

Supervisors

Politecnico di Torino

Prof. Paolo Maggiore

Prof. Gioacchino Cafiero

Università di Napoli Federico II

Prof. Anselmo Cecere

Industrial advisors

Ing. Umberto Papa

Ing. Fabrizio Di Donfrancesco

Academic Year

2025/2026

Abstract

Future high performance combat aircraft are increasingly driven by the combined requirements of low observability, high speed operation and high manoeuvrability, together with wide envelope controllability. These requirements introduce a critical design conflict: conventional control surfaces, such as horizontal and vertical tails, elevators, ailerons and rudders, provide effective aerodynamic control, but may introduce penalties in terms of radar signature, integration complexity, aerodynamic efficiency and control effectiveness under complex aerodynamic conditions, especially at high angles of attack. This issue becomes even more relevant for tailless configurations, where the reduction of conventional stabilizing surfaces requires alternative solutions capable of preserving control authority over a wide flight envelope.

This thesis investigates innovative aerodynamic control effectors for advanced fighter aircraft, with specific focus on the All-Moving Tip (AMT) concept. The AMT consists of a fully movable outer wing-tip surface able to rotate as a rigid body and modify the local aerodynamic loading in the outboard region of the wing. Owing to its spanwise position and large lateral lever arm with respect to the aircraft centreline, even moderate force increments generated by the AMT can produce relevant rolling and yawing moments. At the same time, its wing-integrated nature makes it an attractive candidate for low-observable configurations, provided that its aerodynamic benefits can be achieved with acceptable drag, actuation and structural penalties.

The work is developed through a preliminary theoretical and bibliographic analysis of high angle of attack and high-speed aerodynamics, conventional control surfaces limitations, and the state of the art of passive and active flow-control technologies. The selected AMT configuration is then assessed through Computational Fluid Dynamics simulations on a swept, low aspect-ratio semi-wing equipped with a movable tip. The numerical campaign evaluates the aerodynamic response of the configuration for different angles of attack and AMT deflection angles, analysing global aerodynamic coefficients, pressure fields, spanwise lift distributions, velocity fields, control effectiveness and hinge-moment behaviour.

The device proves to be more effective in the lateral-directional domain than in the longitudinal one. Differential use of the movable tips can generate useful rolling-moment increments, while the associated asymmetric drag contribution provides a promising yaw-control mechanism, especially at high incidence, where conventional rudders may suffer from wake blanketing and loss of local dynamic pressure. Conversely, the pitch-control authority of the AMT is limited by its reduced longitudinal lever arm with respect to the centre of gravity.

The comparison with reference fighter configurations suggests that the AMT, in the analysed layout, should not be interpreted as a standalone replacement for conventional primary control surfaces, but rather as an auxiliary effector capable of contributing to multi-axis control within a broader control-allocation strategy.

The hinge-moment analysis identifies large AMT deflections in the pre-stall, high incidence regime as the most demanding condition for actuator sizing. It also provides a design criterion for the hinge axis placement: the axis should be located close to the AMT centre of pressure under the most critical aerodynamic condition, while still preserving a restoring hinge-moment tendency, namely a tendency of the aerodynamic loads to reduce the AMT deflection. For the present AMT layout, this trade-off suggests an optimal hinge-axis position around 40% of the AMT root chord.

Overall, the AMT emerges as a promising complementary control effector for advanced low-observable aircraft, particularly when integrated within a multi-effector control architecture. Its main value lies in its capability to provide compact, wing-integrated, multi-axis aerodynamic control, maintaining useful effectiveness at high angles of attack while contributing to the reduction of conventional tail-surface dependence. Its main limitations are related to system-level integration, since the wing-tip location introduces critical aeroelastic constraints and demanding actuation requirements within a structurally flexible region with limited available volume.

Future developments should include grid-convergence studies, sideslip and Mach-number sensitivity analyses, unsteady simulations, aeroelastic assessment, experimental validation and full-aircraft modelling, in order to move from the present preliminary CFD assessment toward a complete evaluation of the AMT concept for next-generation fighter aircraft.

Contents

List of Figures

List of Tables

Chapter 1

Introduction

1.1 Introduction

The thesis addresses the study of innovative aerodynamic control solutions for high-speed aircraft, with particular attention to the improvement of manoeuvrability and control authority under demanding aerodynamic conditions. The subject is placed at the intersection of aircraft configuration aerodynamics, high-angle-of-attack flow physics, flight mechanics and computational fluid dynamics. The main objective is to investigate how non-conventional control effectors can contribute to the manoeuvrability of advanced fighter aircraft configurations, especially when conventional control surfaces become less effective or less compatible with low-observable design constraints.

The motivation of the work arises from a fundamental design conflict in future combat aircraft. On one hand, low observability requirements need smooth external shapes, with the possible elimination or reduction of vertical and horizontal tail surfaces and reduced discontinuities, in addition to the need for internal carriage of weapons and sensors. On the other hand, high manoeuvrability requirements need sufficient aerodynamic control authority, even at high angles of attack, where the flow field is separated, nonlinear and dominated by vortical structures. These two requirements are not independent: the same geometric features that improve stealth may reduce natural stability and control effectiveness.

In this context, innovative control effectors represent a key enabling technology. They are intended to provide the required aerodynamic moments while limiting the penalties associated with conventional control surfaces. The present thesis focuses on the *All Moving Wing Tip* (AMT), a movable outboard wing-tip surface capable of modifying the local aerodynamic loads and generating control moments due to its large spanwise distance from the aircraft centreline. The AMT is therefore analysed as a possible solution for improving lateral-directional control and manoeuvrability in highly swept and tailless configurations.

The methodological framework of the thesis is organized in four main steps. First, the operational and aerodynamic requirements of future fighter aircraft are introduced, with emphasis on low observability, high manoeuvrability and high-angle-of-attack flight. Second, the main aerodynamic phenomena associated with increasing angle of attack are discussed, including flow separation, vortex-dominated aerodynamics and the loss of conventional control effectiveness. Third, the state of the art of passive and active flow-control technologies is reviewed, with particular attention to non-conventional aerodynamic effectors. Finally, the selected AMT configuration is investigated through numerical simulations, evaluating its influence on aerodynamic forces, moments and control authority.

1.2 Evolution of Fighter Aircraft Generations

Throughout the history of aviation, military aircraf have played a pivotal role in determining the course of warfare and establishing air superiority, and major powers vigorously pursued advancements in fighter aircraft technology, leading to a series of generational evolutions. Transitions between fighter aircraft generations are driven by breakthroughs in technology, limitations in modernizing existing platforms, and intensifying military competition. Figure 1.1 illustrates the progression of fighter aircraft generations and their defining technologies, based on the fifth-generation framework.

The first fighter jets were introduced during the World War II, with the Messerschmitt Me 262 (developed in Germany), which marked a paradigm shift in aerial combat, offering superior speed and maneuverability compared to conventional propeller-driven aircraft.

The second generation (1955-1960) was marked by the advent of the first supersonic fighters, capable to reach also Mach 2. Usually, they were equipped with air-to-air missiles and radar. The F-104 Starfighter, operated also by the Italian Air Force, is a perfect example of second generation fighter aircraft.

The third generation (1960-1970) saw the introduction of large improvements in avionics and of systems like variable geometry or vectored thrust to gain more efficiency in a broader flight regime. These aircraft were designed to carry a lot of weapons, including air to guide missiles and laser-guided bombs. The F-4 Phantom, symbol of American air superiority during the Vietnam War, is an example of third generation fighter aircraft.

The fourth generation of fighters (1970-1990) brought great developments in terms of multi-role concept, which led to the development of jets able to perform different missions thought for different necessities, such as air-to-air combat or air-to-ground support or recognition. Fourth generation aircraft were the first to equip fly-by-wire technology. In this generation, the technical improvement focus was on maneuverability rather than high-speed, as a decisive property to succeed in air-to-air combat. An example of a 4th generation fighter is the Panavia Tornado, still in service for the Italian Air Force.

After the fourth generation, the generation 4.5 (1990-2000) brought sophisticated avionics, advanced electronic and software features, in order to enable an autopilot system, capable of managing all the possible manoeuvres, according to the pilot's requirements during the flight. The multi-role concept was enhanced with the development of the swing-role capability, meaning the ability of quick role change, either at short notice, or even within the same mission. An example of a 4.5 generation fighter is the Eurofighter Typhoon, currently operated by the German, the Spanish, the UK and the Italian Air Forces.

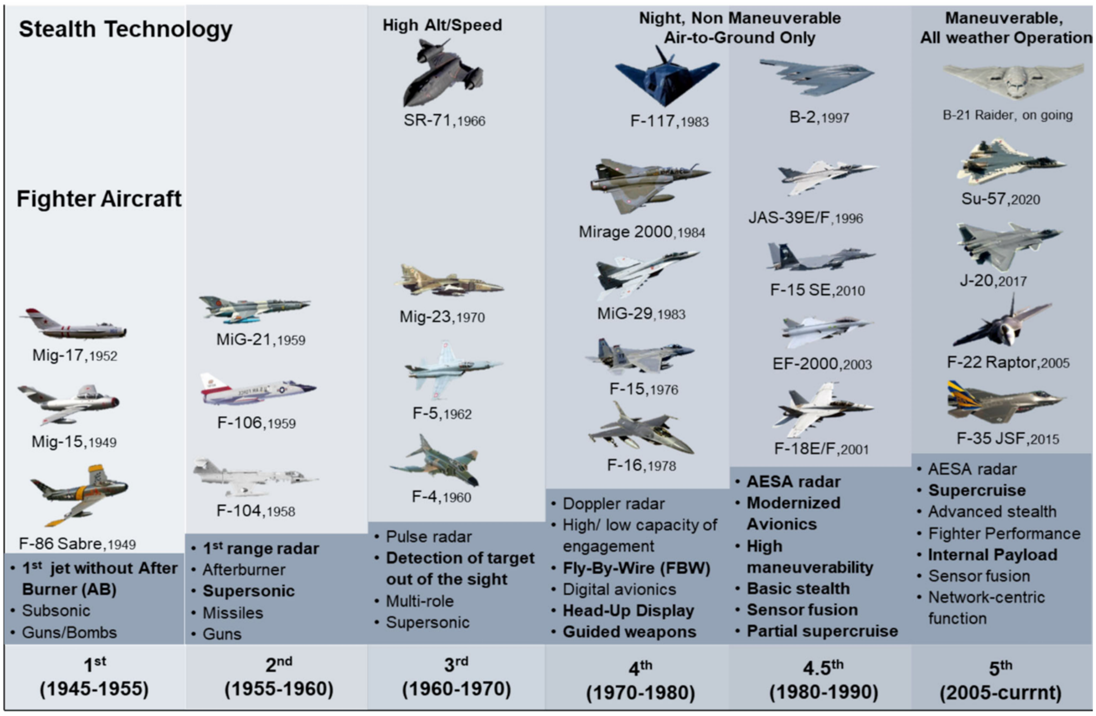

Figure 1.1: Progression of fighter aircraft generations and their defining technologies [1].

Despite these technological achievements, the development of next-generation fighter aircraft remains a strategic priority for military powers, as fighter aircraft performance is not only a determinant of battlefield superiority but also a symbol of a nation's scientific, technological, and defense-industrial capabilities.

1.3 6th-Generation Fighter Aircraft

Sixth-generation fighter aircraft are envisioned to operate at a qualitatively different level than their predecessors. These future platforms are expected to survive and operate effectively in highly contested anti-access/area-denial (A2/AD) environments, where advanced integrated air defence systems, long-range sensors, networked threats and increasingly capable airborne platforms impose demanding requirements on survivability, lethality, mission adaptability and operational autonomy. Therefore, next-generation combat aircraft are conceived as highly integrated systems combining advanced airframe design, propulsion, sensing, control, communication and autonomy technologies [1].

In this scenario, air dominance is no longer associated only with the performance of a single aircraft, but with the ability of a broader system of systems to sense, decide, communicate and act faster than the opponent. Key enabling technologies under development for sixth-generation fighter aircraft include artificial intelligence (AI), advanced sensors and data fusion, network-centric warfare, cloud-based data sharing, electronic warfare (EW), high-performance propulsion systems, directed energy weapons (DEW), autonomous robotic flight and manned-unmanned teaming (MUM-T). AI is expected to support real-time decision-making and autonomous mission execution; advanced sensor fusion is intended to enhance situational awareness; and network-centric operations are expected to enable real-time data exchange and collaborative missions across multiple manned and unmanned platforms. Together, these technologies aim to improve survivability, lethality, operational speed and mission precision.

Within this technological framework, low observability remains one of the most critical design drivers. Military aircraft achieve low-observable capability through a combination of radar-absorbing materials (RAM), configuration-optimized shaping, internal weapon carriage, careful management of outer mold lines (OML), and alignment of control-surface edges with external airframe features in order to reduce radar cross-section (RCS). Historically, faceted shaping techniques and RAM coatings were used to reduce radar reflections by minimizing isotropic and randomly scattering surfaces. More advanced stealth aircraft further exploit smooth external geometries, blended wing-body layouts and tailless configurations to reduce both radar signature and aerodynamic drag.

However, low observability alone is not sufficient for an advanced fighter aircraft. High manoeuvrability remains a fundamental requirement because the aircraft must be able to rapidly and controllably modify its attitude, trajectory and pointing direction during both offensive and defensive manoeuvres. This requirement becomes particularly demanding at high angles of attack, where separated flow, vortex interactions, asymmetric loads and unsteady aerodynamic phenomena may strongly affect the available control authority and the aerodynamic response.

High manoeuvrability should therefore be interpreted not only as the ability to generate large accelerations or high turn rates, but also as the ability to preserve controllability throughout a wide flight envelope. A highly manoeuvrable aircraft must maintain sufficient control authority, avoid departure from controlled flight, withstand strong aerodynamic coupling and recover from highly nonlinear flow conditions.

This introduces a major design trade-off. Conventional aircraft generally rely on horizontal tails, vertical tails, elevators, ailerons and rudders to provide stability and control. These surfaces are effective because they provide aerodynamic forces with favourable moment arms, but they also introduce external surfaces, gaps, discontinuities and radar-scattering features. Conversely, low-observable configurations tend to reduce or eliminate vertical and horizontal tails, resulting in improved stealth but reduced natural stability and control margins. Consequently, future fighter aircraft require innovative control strategies and non-conventional aerodynamic effectors capable of providing the required manoeuvrability without compromising the low-observable character of the platform.

For this reason, the development of innovative passive and active control solutions is a central research topic for future combat aircraft. Passive solutions can improve the baseline aerodynamic behaviour by controlling separation, vortex formation or vortex breakdown, while active effectors can generate commanded aerodynamic or propulsive moments according to the flight-control demand. In the present thesis, this general problem is narrowed to the analysis of the All Moving Wing Tip, investigated as a possible aerodynamic effector for improving control authority and manoeuvrability in advanced high-speed fighter configurations.

1.3.1 Tailless configurations

In terms of airframe design, sixth-generation fighter aircraft are expected to feature increasingly integrated and innovative configurations. Among these, the tailless configuration is emerging as a key enabler of extreme stealth performance, since the elimination of vertical and horizontal stabilizers contributes to reducing radar cross-section.

The term “tailless” aircraft, sometimes referred to as a “flying wing” aircraft, is defined as an aircraft having no auxiliary horizontal stabilizing plane, deriving lift and controlling moment solely from the main plane. In this type of configuration, the conventional separation between wing, fuselage and tail is partially or completely removed. As a result, the main plane must provide not only lift, but also trim, stability and control authority.

The elimination of the tail offers important advantages in terms of low observability and aerodynamic efficiency, while introducing significant stability and control challenges, requiring advanced flight control techniques to ensure stability and maneuverability.

Figure 1.2 shows two representative tailless aircraft platforms, namely the ICE and SACCON configurations. Both layouts highlight the absence of conventional horizontal and vertical tail surfaces.

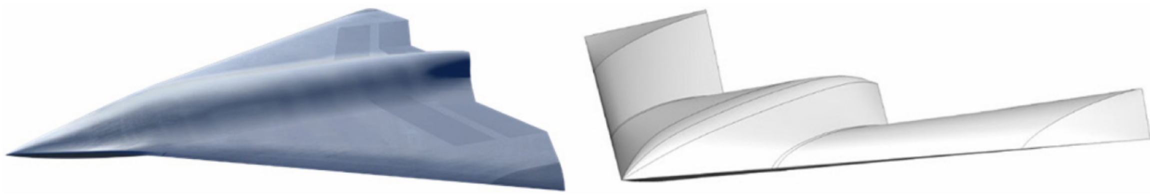

Figure 1.2: ICE and SACCON tailless platforms [2].

Benefits of tailess configuration

This configuration allows for a compact design that reduces wetted area, subsequently decreasing both skin-friction and parasitic drag, thereby lowering total aerodynamic drag. Moreover, a higher aspect ratio can enhance lift, potentially reducing stall speed. The increase lift and reduction of drag improve lift-to-drag (L/D) ratio and aerodynamic efficiency.

There are also design advantages, such as weight savings and increased structural efficiency, due to the eliminated tail and reduced number of components. Furthermore, the internal volume of a tailless airframe is greater than that of a conventional tube fuselage, enabling increased payload capacity.

In addition, tailless configurations can also offer environmental advantages: reduced noise (acoustic signature), lower fuel consumption, and enhanced propulsion efficiency, all of which contribute to lower pollutant emissions.

Stability and control problems

In theory, to ensure a naturally stable configuration, the center of gravity (CG) should be forward of the neutral point (NP). However, cambered main wings intensify the movement of the neutral point as the angle of attack (AoA) changes. This may introduce instability, which is further compounded by CG shifts during flight due to payload movement, payload release, or fuel consumption from multiple tanks.

These main wing instabilities are conventionally mitigated by a horizontal and vertical tail planes, which provides stabilizing aerodynamic moments. Without them, tailless aircraft face challenges in achieving stability and trim (equilibrium), in addiction to control coupling issues. Furthermore, some particular conditions such as high AoA flight, weapon bay door effects, or fuel sloshing, can add further instabilities.

Therefore, while tailless configurations are highly attractive for future low-observable aircraft, they require advanced flight control systems, control allocation strategies and innovative aerodynamic effectors to guarantee adequate maneuverability, stability and controllability throughout the flight envelope. This becomes particularly important at high angles of attack, where the flow field becomes strongly nonlinear and dominated by separated flow and vortex interactions. In this context, innovative control effectors represent a critical enabling technology for making tailless configurations viable for highly maneuverable new fighter generation aircraft.

Chapter 2

Theoretical framework

2.1 Aircraft reference frame

Figure 2.1 shows the aircraft body reference frame adopted in this thesis (following the standard aircraft-body reference frame), in which:

- the longitudinal x-axis is directed along the main direction of the aircraft, from the tail toward the nose, and is associated with the roll motion;
- the lateral y-axis is transverse to the aircraft, extending from one wing half to the other, and is associated with the pitch motion;
- the vertical z-axis is perpendicular to the plane formed by the longitudinal and lateral axes, and is associated with the yaw motion.

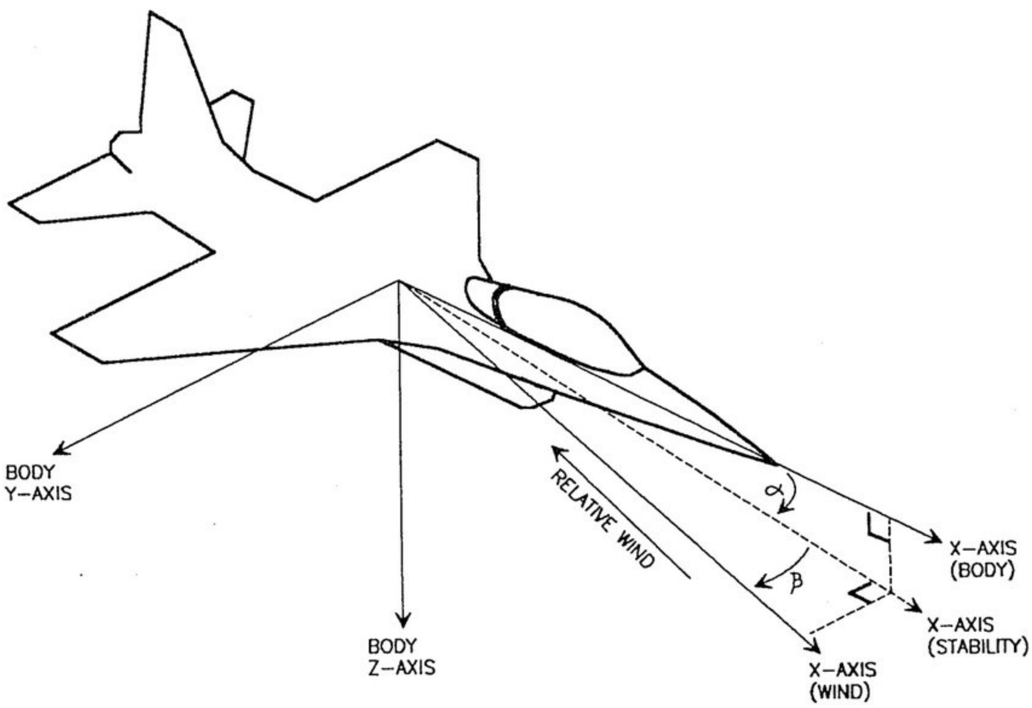

Figure 2.1: Aircraft body reference frame adopted [3].

2.2 Aerodynamic coefficients

The angle of attack (AoA) α is the angle between the free-stream velocity vector and the aircraft longitudinal axis projected onto the longitudinal plane. The angle of sideslip (AoS) β is the angle between the free-stream velocity vector and the aircraft symmetry plane (Figure 2.1).

The reference planform area is denoted by S or S_{ref}, the reference wingspan by b, and the reference mean aerodynamic chord by $\bar{c}$. These quantities are used to make aerodynamic forces and moments dimensionless.

The reference free-stream dynamic pressure is defined as:

$$q_\infty = \frac{1}{2}\rho_\infty V_\infty^2$$

where ρ_∞ is the free-stream air density and V_∞ is the free-stream velocity.

2.2.1 Force coefficients

The aerodynamic force coefficients are defined as

$$C_L = \frac{L}{q_\infty S}$$
$$C_D = \frac{D}{q_\infty S}$$
$$C_Y = \frac{Y}{q_\infty S}$$

where C_L is the lift coefficient, C_D is the drag coefficient, and C_Y is the side-force coefficient.

Lift L is defined as the aerodynamic force component perpendicular to the free-stream direction in the longitudinal plane, drag D is the component parallel to the free-stream direction, while side force Y is the lateral component perpendicular to both lift and drag.

2.2.2 Moment coefficients

The aerodynamic moment coefficients are defined as

$$C_l = \frac{\mathcal{L}}{q_\infty S b}$$
$$C_m = \frac{M}{q_\infty S \bar{c}}$$
$$C_n = \frac{N}{q_\infty S b}$$

where C_l, C_m, C_n are respectively the rolling, pitching and yawing moment coefficients. The dimensional aerodynamic moments are evaluated with respect to the aircraft center of gravity. The rolling moment $\mathcal{L}$ is the moment component about the longitudinal x-axis, the pitching moment M is the component about the lateral y-axis, and the yawing moment N is the component about the vertical z-axis.

It should be noted that lift and drag are defined with respect to the wind axes, whereas the aerodynamic moments are expressed about the body-fixed axes.

All the aerodynamic forces and moments are generated by the pressure distribution over the surface of the aircraft, integrated over the entire surface.

For the present thesis, the most relevant quantities are the incremental force and moment coefficients produced by the control effector deflection. If δ_{AMT} denotes the deflection angle, the aerodynamic increment associated with the control surface can be expressed as

$$\Delta C_i = C_i(\delta) - C_i(\delta = 0^\circ)$$

where C_i may represent any force or moment coefficient.

2.3 Aerodynamic phenomenology at increasing angle of attack

Considering a generic wing or lifting surface, immersed in an aerodynamic (subsonic) flow, the present section aims to studying how the flow phenomenology evolves as the angle of attack α progressively increases.

2.3.1 Attached flow and linear aerodynamic response

At low and moderate angles of attack, the flow remains mostly attached over the upper and lower surfaces, and the pressure distribution varies smoothly as the incidence changes. An increase in angle of attack strengthens the flow acceleration over the upper surface, increasing the pressure difference between the lower and upper sides of the wing, producing a corresponding increase in suction peak and therefore in lift.

In this regime, the aerodynamic behaviour of the lifting surface can be described through a linear relation between the lift coefficient C_L and the angle of attack α:

$$C_L \simeq C_{L_0} + C_{L_\alpha}\alpha$$

where C_{L_0} is the lift coefficient at zero angle of attack and C_{L_α} is the lift-curve slope. Both parameters depend on the airfoil geometry and wing planform.

The drag coefficient C_D is mainly composed of skin-friction drag, pressure drag and lift-induced drag (associated with the finite-span vortex system). The drag polar can often be approximated by the parabolic relation:

$$C_D = C_{D_0} + kC_L^2, \tag{2.1}$$

where C_{D_0} is the drag coefficient at zero lift and k is the lift-induced drag factor, usually expressed as

$$k = \frac{1}{\pi e AR}, \tag{2.2}$$

with $AR = b^2/S$ being the aspect ratio and e the Oswald factor, which takes into account how much the actual lift distribution along the span deviates from the ideal elliptical one.

At small angles of attack, since the boundary layer remains attached over most of the surface, the wake is limited and the pressure recovery toward the trailing edge occurs without major flow reversal, so the aerodynamic efficiency (lift-to-drag ratio) remains high.

2.3.2 Onset of separation and nonlinear effects

As the angle of attack increases, the suction demand on the upper surface becomes stronger and the adverse pressure gradient becomes more severe. The boundary layer, characterized by lower momentum than the external inviscid flow, may no longer be able to overcome this pressure rise. When this occurs, the near-wall flow decelerates, the boundary layer thickens and, eventually, flow reversal may appear close to the surface. This marks the onset of boundary layer separation.

The beginning of separation does not necessarily imply an immediate loss of lift. In most of the cases, the separated region first appears locally, near the trailing edge or in specific spanwise regions of the wing. Therefore, the effective aerodynamic shape seen by the outer flow is no longer coincident with the physical geometry of the aircraft, because the separated boundary layer and the associated wake modify the apparent contour of the body. As a result, small changes in angle of attack may produce disproportionately large changes in the pressure field.

In this transition region, the aerodynamic response then starts to deviate from the linear trend. The lift coefficient may still increase with angle of attack, but at a reduced rate; the drag coefficient begins to rise more rapidly; and the pitching moment may exhibit significant changes due to the displacement of the effective pressure distribution.

The onset of separation also introduces three-dimensional effects. On a finite wing, the local separation pattern is influenced by spanwise pressure gradients, tip effects and their interaction. Therefore, the flow field must be considered as a coupled three-dimensional system in which local separation may trigger global changes in the aerodynamic loads.

2.3.3 Separated flow and vortex dominated aerodynamics

At sufficiently high angles of attack, separated flow becomes one of the dominant features of the aerodynamic field. The separated shear layers may roll up into vortical structures, while the wake behind the aircraft becomes wider, more unsteady and more sensitive to perturbations. In this regime, the aerodynamic loads are governed by the position, strength and stability of separated vortices.

Vortical structures can have both beneficial and detrimental effects. On one hand, coherent vortices may generate low-pressure regions over portions of the wing, contributing to additional lift and sometimes delaying complete loss of aerodynamic effectiveness. On the other hand, vortex motion, vortex interaction and vortex breakdown can produce abrupt variations of pressure distribution, unsteady loads, buffet, asymmetric forces and strongly nonlinear characteristics, that may be highly unpredictable.

A further complication is that the flow may become asymmetric even when the wing geometry and the free-stream conditions are nominally symmetric. Small disturbances or geometric imperfections may cause one separated structure to become stronger or differently positioned than its counterpart on the opposite side. This can generate side force, rolling moment and yawing moment without a corresponding commanded control input.

For these reasons, high angle of attack regime represents a critical design area for advanced combat aircraft. The problem is not limited to achieving high lift, but also includes preserving stability, maintaining control authority and preventing departure from controlled flight. A proper understanding of separated and vortex-dominated flows is therefore essential before analysing the influence of wing geometry and, subsequently, the effectiveness of innovative control effectors.

2.4 High-speed aerodynamic phenomenology

High-speed aerodynamics refers to flight conditions in which compressibility effects become relevant. The relative importance of compressibility effects is primarily governed by the Mach number, defined as:

$$M = \frac{V}{a}$$

where V is the flow velocity and a is the local speed of sound. For a perfect gas, the speed of sound is given byn $a = \sqrt{\gamma RT}$, where γ is the ratio of specific heats, R is the gas constant and T is the absolute temperature.

The free-stream Mach number is therefore $M_\infty = V_\infty / a_\infty$ and represents the main non-dimensional parameter used to classify the flow regime. For practical aerodynamic purposes, the flow may be broadly classified as:

- Incompressible subsonic: $0 \leq M_\infty \lesssim 0.3$
- Compressible subsonic: $0.3 \lesssim M_\infty \lesssim 0.8$
- Transonic: $0.8 \lesssim M_\infty \lesssim 1.2$
- Supersonic: $1.2 \lesssim M_\infty \lesssim 5$
- Hypersonic: $M_\infty \gtrsim 5$

At low Mach numbers the density variations of the flow are usually small, so density is assumed to remain approximately constant and pressure variations are mainly associated with changes in velocity. This approximation is generally acceptable at low Mach numbers.

When the Mach number increases, pressure disturbances are accompanied by density and temperature variations, and the coupling between pressure, density and temperature becomes increasingly important. This coupling introduces new phenomena, related to compressibility effects, such as local supersonic regions, shock-wave formation, and shock-wave/boundary-layer interaction, that modify the pressure distribution around the aircraft and affect the onset of separation.

In subsonic flight, the local Mach number remains below unity over the entire flow field. Compressibility effects become progressively important already in the high-subsonic regime. A conventional practical threshold is $M_\infty \simeq 0.3$, above which density variations may no longer be negligible for accurate aerodynamic prediction.

As the Mach number further increases, the acceleration of the flow around the aircraft can make the local Mach number reach unity even if the free-stream Mach number is still lower than one. This marks the beginning of the transonic regime, in which both subsonic and supersonic regions coexist around the aircraft. In supersonic flight, the free-stream Mach number is greater than unity.

2.4.1 Transonic flow and critical Mach number

The critical Mach number M_{cr} of an airfoil or aircraft configuration is the free-stream Mach number for which the local Mach number first reaches unity somewhere on the surface:

$$M_{local} = 1$$

Although the free-stream flow is still subsonic, local accelerations over the wing (or fusolage) can produce sonic conditions in regions of high velocity. For a given airfoil, the first sonic point typically appears near the region of maximum suction, often on the upper surface.

When $M_\infty < M_{cr}$, the flow remains entirely subsonic and no shock wave is present. When M_∞ becomes slightly larger than M_{cr}, a small supersonic pocket appears on the airfoil. This supersonic region is terminated downstream by a shock wave, through which the flow returns to subsonic conditions. As the free-stream Mach number increases further, the supersonic region extends over a larger portion of the chord and the shock wave becomes stronger.

The transonic regime is therefore characterized by the coexistence of subsonic regions, supersonic pockets and shock waves. This makes the aerodynamic response highly nonlinear. Small changes in Mach number, angle of attack or control-surface deflection may produce large changes in shock position and intensity, with corresponding changes in pressure distribution, lift, drag and pitching moment.

For a given airfoil at a fixed angle of attack, the critical Mach number may be interpreted qualitatively by comparing the pressure coefficient required to produce sonic conditions with the minimum pressure coefficient reached on the airfoil. The pressure coefficient corresponding to local sonic conditions is

$$C_p^*(M_\infty) = \frac{2}{\gamma M_\infty^2}\left[\left(\frac{1+\frac{\gamma-1}{2}M_\infty^2}{1+\frac{\gamma-1}{2}}\right)^{\frac{\gamma}{\gamma-1}} - 1\right]$$

The critical Mach number is reached when the minimum pressure coefficient on the airfoil becomes equal to this critical pressure coefficient:

$$C_{p_{min}} = C_p^*$$

This relation shows that M_{cr} depends on the geometry of the airfoil, on the lift condition and therefore on the angle of attack. Thinner airfoils, lower camber and reduced suction peaks generally help increase the critical Mach number.

2.4.2 Wave drag and drag rise

As the Mach number increases beyond the critical value, the shock waves generated by the local supersonic regions modify the pressure distribution and introduce irreversible losses. The corresponding drag contribution is called *wave drag*. The total drag coefficient in compressible flow can be conceptually written as

$$C_D = C_{D_{inc}} + \Delta C_{D_w}$$

where $C_{D_{inc}}$ represents the drag contribution that would be present in the corresponding incompressible (or weakly compressible) flow, while ΔC_{D_w} is the additional wave-drag contribution due to compressibility and shock waves.

In the high-subsonic and transonic regimes, wave drag is responsible for the so-called *drag rise*. The Mach number at which the drag coefficient begins to increase rapidly is usually called the *drag-divergence Mach number* M_{DD}. This value is higher than the critical Mach number, because the first appearance of a local sonic point does not necessarily produce a large drag penalty; the severe drag rise occurs only when the supersonic region and the associated shock wave become sufficiently strong.

For a complete aircraft, wave drag depends on the global distribution of volume and lift, on the integration between wing and body and on the presence of stores, nacelles, inlets or other protuberances. For this reason, high-speed aircraft design requires careful control of the entire external shape.

2.4.3 Shock-induced separation and buffet

Across a shock wave, the static pressure increases abruptly, and this sudden pressure rise acts as a strong adverse pressure gradient for the boundary layer. If the near-wall flow does not have enough momentum to overcome this pressure rise, the boundary layer may separate immediately downstream of the shock.

This phenomenon is called *shock-induced separation*. It produces a thicker wake, increasing pressure drag, reduces lift and may cause significant changes in pitching moment, because it causes a sudden change in the pressure distribution. Since the shock position can oscillate in time and interact with the separated region, shock-induced separation may also generate buffet, namely unsteady aerodynamic loads and pressure fluctuations.

The boundary-layer state plays an important role in this process. A laminar boundary layer has lower skin-friction drag, but it is more sensitive to adverse pressure gradients and tends to separate more easily. Instead, a turbulent boundary layer has higher skin-friction drag, but it contains more near-wall momentum and is therefore more resistant to separation. For this reason, devices such as vortex generators may be used to energize the boundary layer and delay separation, but this benefit is obtained at the cost of increased viscous drag.

For control surfaces, shock-induced separation is particularly relevant because it can reduce or distort the effectiveness of the control input. A deflected surface may generate a shock wave, move an existing shock, or cause the shock to interact with a separated region. The resulting incremental forces and moments may be strongly nonlinear functions of Mach number, angle of attack and deflection angle, and can therefore affect the control effectiveness in a way that is difficult to predict.

2.4.4 Aerodynamic-center shift and pitching-moment effects

Compressibility also affects the location of the aerodynamic center and the resulting pitching moment. In incompressible subsonic theory, the aerodynamic center of a thin airfoil is approximately located at the quarter-chord point; in supersonic thin-airfoil theory, the aerodynamic center moves approximately toward the mid-chord point.

In the transonic regime, the situation is more complex because the shock waves alter the pressure distribution over the airfoil. As the Mach number increases and the shock system develops, the center of pressure generally tends to move rearward. This rearward displacement may produce a nose-down pitching-moment variation, often referred to as *Mach tuck*.

2.4.5 Implications for control effectiveness at high speed

For stability and control reasons, a control surface that is effective in subsonic flight may require larger deflections at transonic speed if the baseline pitching moment changes significantly. Moreover, if shock-induced separation occurs near the control surface, the relationship between deflection angle and generated moment may become strongly nonlinear or even lose effectiveness over part of the flight envelope.

So, high-speed flow phenomena have direct consequences on control-surface effectiveness. At low speed, the incremental force or moment generated by a control surface can often be interpreted mainly as a consequence of the local change in camber or incidence. At transonic and supersonic speeds, the same deflection may also generate shock waves, expansion waves, shock-boundary-layer interactions and additional wave drag. On one side of the surface, the flow may experience compression and generate an oblique shock; on the opposite side, the flow may experience expansion and generate an expansion fan. The resulting pressure difference produces the desired control force or moment, but it may also introduce strong nonlinearities and additional drag.

In the transonic regime, the effectiveness of a control surface is particularly sensitive to shock position. A small deflection can move a shock wave, strengthen it or cause shock-induced separation. As a result, in some cases, increasing the deflection may not produce a proportional increase in control authority, because the local flow separates or because the control surface becomes immersed in a low-energy separated region.

2.5 Influence of wing geometry on high angle of attack and high speed performance

At high AoA and high speed, due to the complex phenomena that have been seen to characterise these regimes, the wing geometry becomes even more important in determining its aerodynamic behavior. While at low incidence the lift generation mechanism can often be interpreted mainly through airfoil characteristics and attached-flow assumptions, at high incidence the global three-dimensional geometry of the lifting surface becomes dominant.

Parameters such as aspect ratio, sweep angle, taper ratio, leading-edge sharpness, thickness distribution and planform shape determine how the flow separates, where vortical structures are generated, and how these structures interact with the rest of the aircraft, improving or worsening high AoA and high speed performance, which are essential for sixth-generation fighters.

The influence of wing geometry is twofold. On one hand, the geometry defines the baseline aerodynamic performance of the aircraft, including lift, drag and moment characteristics. On the other hand, it also determines the quality of the flow field in which control effectors operate. A control surface located in a region of attached or coherent vortical flow may retain useful authority, whereas the same surface may become ineffective if immersed in a separated, highly unsteady or low-energy wake.

2.5.1 Aspect ratio

The aspect ratio (AR), one of the most important geometric parameters governing the aerodynamic behaviour of a wing, is defined as

$$AR = \frac{b^2}{S} \tag{2.3}$$

where b is the wing span and S is the reference planform area. For a rectangular wing, the aspect ratio can also be interpreted as the ratio between span and chord.

High-aspect-ratio wings are generally associated with efficient lift generation and reduced induced drag, because the influence of the wing-tip vortices is relatively confined when compared with the total span. Instead, in low-aspect-ratio wings, since the span is relatively small compared with the chord, three-dimensional effects become more important. The wing-tip vortices influence a larger portion of the lifting surface, and this makes the wing's aerodynamic load generation less efficient. As a consequence, the lift-curve slope is usually lower than that of a high-aspect-ratio wing, as shown in Figure 2.2. In other words, for the same small variation of angle of attack, a low-aspect-ratio wing generally produces a smaller increment of lift coefficient.

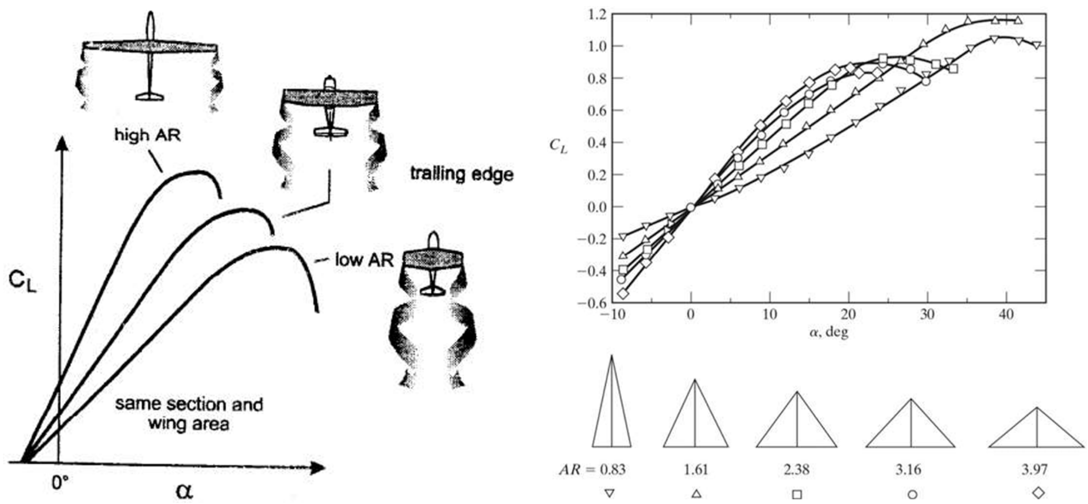

Figure 2.2: Aspect ratio effect on the lift curve slope [4] [5].

Despite their general less efficient aerodynamics, low-aspect-ratio wings may exhibit favourable characteristics at high angles of attack. Their strong vortical flow can make the stall more gradual than in some higher-aspect-ratio wings: instead of an abrupt stall affecting a large portion of the span, the flow may reorganize into coherent vortical structures that continue to contribute to lift and control, even in post stall regime.

2.5.2 Sweep angle

The sweep angle Λ is the angle between a characteristic wing line, usually the quarter-chord line, and the lateral axis of the aircraft (y_b). Wing sweep also plays a central role, because it determines the component of the free-stream velocity normal to the leading edge. For a swept wing, the velocity component normal to the leading edge is lower than the total free-stream velocity. This is one of the reasons why sweep is widely used in high-speed aircraft: by reducing the effective normal Mach number, sweep helps delay compressibility effects and the associated drag rise in transonic and supersonic flight, as shown in Figure 2.3

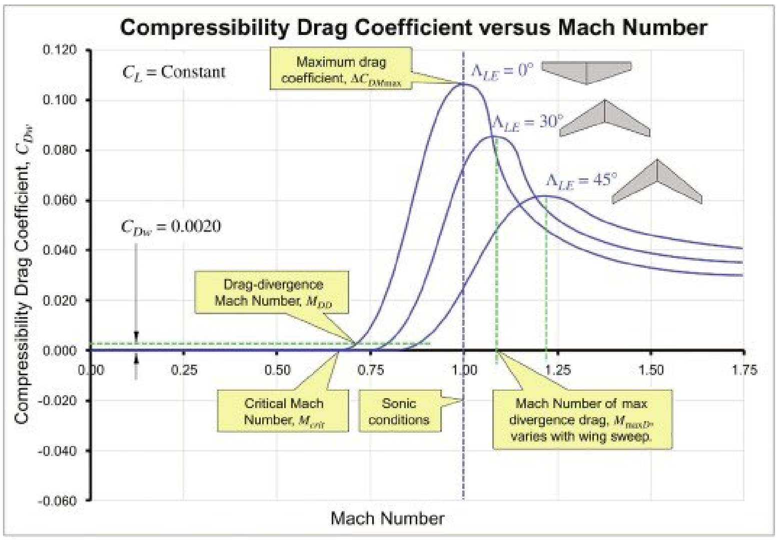

Figure 2.3: Sweep angle effect on the compressibility drag coefficient as a function of Mach number [6].

At high sweep angles, the leading edge becomes a dominant flow feature, and separation from the leading edge may organize into coherent vortical structures rather than immediately producing a fully stalled flow. These vortices can generate strong suction over the upper surface and provide an additional lift contribution. Therefore, while sweep reduces the conventional attached-flow lift-curve slope, it can also enable vortex lift mechanisms at higher angles of attack.

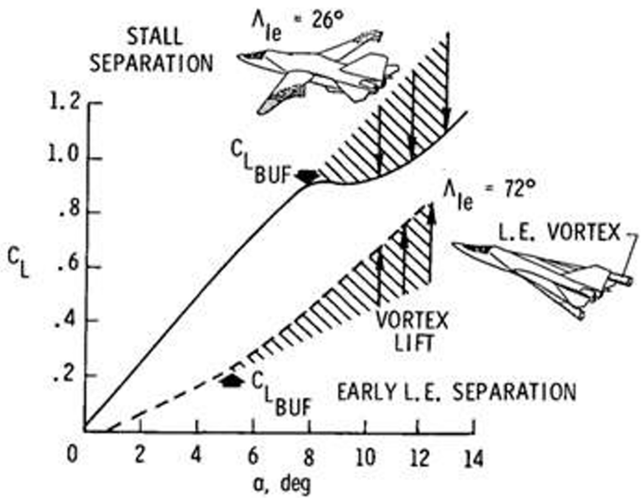

Figure 2.4: Effect of leading-edge sweep on lift generation and buffet onset for a variable-sweep fighter configuration [7].

The combined effect of low aspect ratio and high sweep is therefore particularly relevant for fighter aircraft. Such wings may be less efficient in the low speed and low AoA regimes, but they can provide favourable high angle of attack performance, compact planform integration, reduced wave-drag penalties at high speed, and compatibility with low-observable configurations. This explains why highly swept and low aspect-ratio wings are particularly suitable for advanced combat aircraft and tailless configurations.

2.5.3 Planform effects and spanwise flow

The wing planform determines how aerodynamic loading is distributed both chordwise and spanwise. At high angles of attack, this distribution is strongly coupled with separation and vortex formation.

A swept wing promotes spanwise flow and changes the way in which separation develops. Because the pressure field is not uniform along the span, the boundary-layer flow tends to acquire an outward component. This outward motion can transport low-momentum fluid toward the wing tip, making the outer wing more prone to separation. Outboard separation is often undesirable because it can reduce aileron effectiveness, produce wing drop and generate nonlinear rolling and pitching moments.

Furthermore, at the wing tip, the pressure difference between the lower and upper surfaces drives the formation of the tip vortex, which interacts with the local loading and with any control surface installed near the outer wing. At high angles of attack, the tip region may be affected simultaneously by local separation, tip-vortex effects and leading-edge vortex structures. Therefore, an outboard control effector can produce complex coupled effects on controlling moments.

2.5.4 Transonic and supersonic airfoils

In supersonic flight, the flow around the aircraft is governed by shocks and expansion waves, and a lifting surface generates pressure differences through a sequence of compressions and expansions associated with its thickness, camber and angle of attack.

For supersonic flight, the use of airfoils with small thickness-to-chord ratios is beneficial because it reduces the strength of the shocks generated by the thickness distribution and consequent flow deflection. Sharp leading edges can also help avoid detached bow shocks and promote weaker attached shocks, provided that the local flow deflection is compatible with attached-shock conditions. Typical supersonic airfoil concepts include double-wedge and biconvex sections.

Supercritical airfoils, which are mainly designed for high-subsonic and low-transonic flight use a relatively flat upper surface, aft camber and a modified pressure recovery to delay and weaken the shock wave on the upper surface. Their objective is to increase the drag-divergence Mach number and reduce shock-induced separation in transonic cruise.

2.5.5 Leading-edge profile and separation behaviour

The leading edge defines how the incoming flow meets the front part of the wing and, therefore, how separation begins when the incidence increases. The fundamental geometric parameter is the leading edge radius, which helps to define the leading edge sharpness.

A rounded leading edge tends to allow the flow to remain attached over a wider range of small and moderate angles of attack. The stagnation point can move smoothly around the leading edge as the angle of attack changes, and the suction peak develops progressively. This behaviour is generally favourable for attached flow and low speed performance and for delaying the onset of leading edge separation.

A sharp leading edge behaves differently. Since the flow cannot smoothly turn around a sharp geometric discontinuity at high incidence, separation may occur directly from the leading edge. This separation can be detrimental if it produces a broad, disorganized separated region; however, in highly swept wings, a sharp leading edge helps the separated shear layer to roll up into a coherent leading-edge vortex. In this case, separation is used as a controlled mechanism to generate vortex lift.

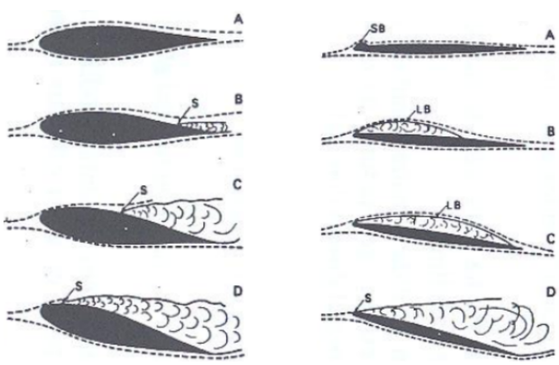

Figure 2.5: Comparison of separation mechanisms for rounded and sharp leading-edge airfoils [8].

For a fighter aircraft, the leading edge must be designed not only to generate lift, but also to control the development of separated and vortical flow structures, in particular when control effectors are located downstream or outboard of the leading edge, because their effectiveness depends on the local flow quality created by the upstream geometry.

A rounded leading edge may exhibit a separation point that moves with the flight condition, making the aerodynamic response more dependent on boundary-layer state and local pressure gradients. Conversely, a sharp leading edge help to fix the separation line more geometrically, making the initial separation location more predictable. This makes sharp leading edge airfoils even more suitable for fighter aircraft.

2.5.6 Slender Delta wings

Based on the previous considerations, highly swept low-aspect-ratio wings, with sharp leading edge and thin airfoil, represent one of the most suitable configurations for high-speed fighter aircraft capable of operating at high speed and high angles of attack.

In this context, slender delta wings offer several favourable characteristics, providing a useful compromise between high-speed requirements and high-angle-of-attack manoeuvrability. Their high sweep angle reduces the velocity component normal to the leading edge, which is beneficial for high-speed flight because it delays compressibility-related effects and drag rise. At the same time, their low aspect ratio and sharp leading edges promote controlled leading-edge separation at high incidence. Rather than producing an immediate and complete stall, the separated shear layers can roll up into coherent leading-edge vortices that, with them core characterized by high rotational velocity and low pressure, generate low-pressure regions over the upper surface and provide an additional lift contribution, called *vortex lift*.

For this reason, highly swept and low aspect ratio wings, although they generally exhibit a lower lift curve slope at low speeds compared with high aspect ratio wings, can maintain useful aerodynamic performance at angles of attack much higher, as shown in Figure 2.6.

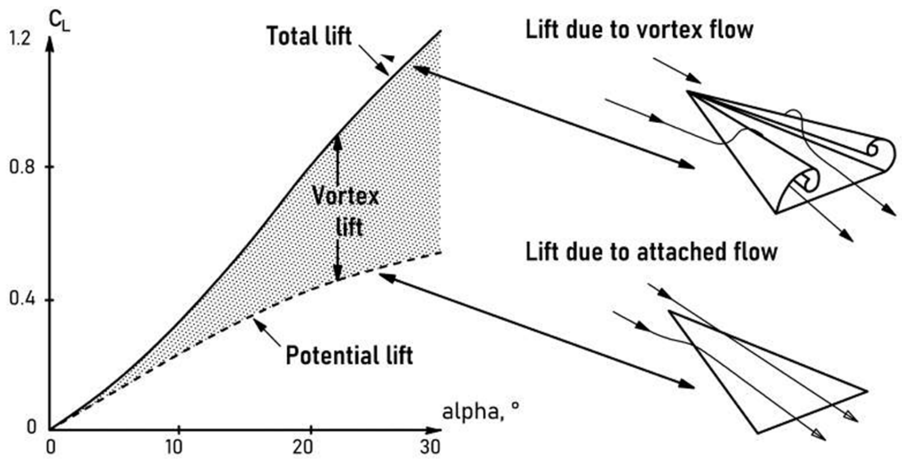

Figure 2.6: Vortex lift generated by slender delta wing [9].

The low-pressure footprint associated with the vortex core may delay conventional boundary-layer separation in some regions of the wing, while the spanwise pressure gradients induced by the vortex can promote secondary separation and additional vortex structures in other regions.

The vortex has a viscous core, but the flow around it is largely governed by inviscid rotational motion. Experimental observations on slender delta wings show that, even though the initial separation is viscous in nature, the main vortex structure behaves largely as an inviscid phenomenon outside the viscous core, with the principal features of the vortical flow, such as vortex position and overall topology, relatively insensitive to Reynolds number over a significant range [10].

As the angle of attack increases further, the vortex system may become asymmetric even in nominally symmetric conditions, generating side force, rolling moment and yawing moment. At still higher incidence, the beneficial vortex-lift mechanism reaches its limit. The leading-edge vortices grow in strength and size, but they may eventually undergo *vortex breakdown*: the coherent vortex core loses its stability, expands, and transforms into a more disordered separated flow (Figure 2.8). As the angle of attack increases, the breakdown location generally moves upstream. The suction generated by the vortex is reduced, leading to lift loss, increased drag, unsteady loads and abrupt changes in moment coefficients.

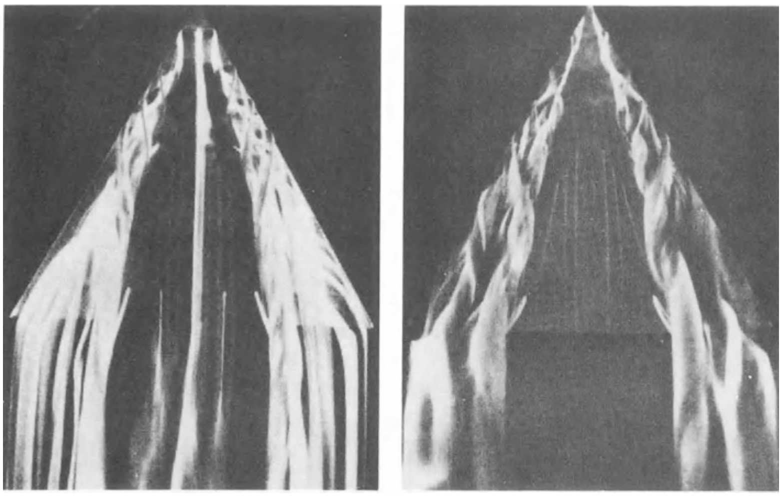

a. Small angle of attack – bubble separation case, $\alpha = 3^o$

b. Moderate angle of attack – rolled-up vortices case, $\alpha = 12^o$

Figure 2.7: Top view of the flow over delta wings with sharp leading edges [10].

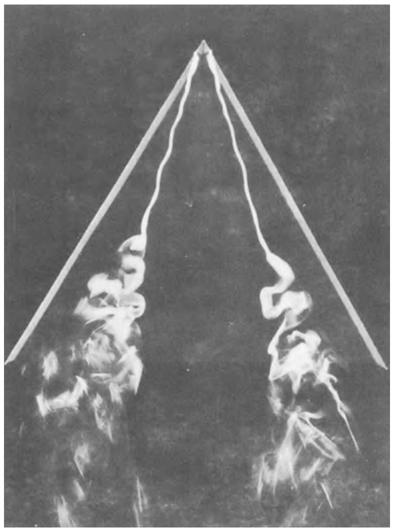

Figure 2.8: Top view of the breakdown of the leading edges vortices on a delta wing [10].

Chapter 3

State of the Art of Flow Control Technologies

3.1 Flight control system

A flight control system is the set of devices, mechanisms, actuators, sensors and control laws that allows the pilot or the automatic control system to command the aircraft motion. Its fundamental purpose is to convert a command input into aerodynamic or propulsive forces and moments capable of trimming, stabilizing and manoeuvring the aircraft.

From a functional point of view, the flight control system forms the link between the desired aircraft response and the physical control effectors installed on the airframe. A command generated by the pilot, the autopilot or the flight control computer is transmitted to one or more actuators. The actuators move the control surfaces or activate the control devices. These devices modify the pressure distribution, circulation, drag, side force or propulsive force acting on the aircraft, thereby producing the required pitching, rolling or yawing moments.

In a simplified form, the control chain can be represented as:

$$\text{Command} \rightarrow \text{Control law} \rightarrow \text{Actuator} \rightarrow \text{Control effector} \rightarrow \text{Aerodynamic moment} \rightarrow \text{Aircraft response} \rightarrow \text{Feedback}$$

3.1.1 Reversible flight control system

The simplest flight control systems are mechanical and reversible. In a reversible mechanical control system, the pilot is connected to the control surface through cables, rods, pulleys, bellcranks or push-pull linkages. The same mechanical line transmits both the position command from the cockpit to the surface and the aerodynamic hinge moment from the surface back to the pilot. Therefore, the pilot directly feels the aerodynamic loads acting on the control surface.

In this case, the force required at the cockpit depends strongly on the hinge moment of the control surface. The dimensional hinge moment can be written as:

$$H = q_\infty S_c c_c C_h, \tag{3.1}$$

where H is the hinge moment, q_∞ is the free stream dynamic pressure, S_c is the control surface reference area, c_c is a characteristic chord of the control surface and C_h is the hing moment coefficient. The hinge moment coefficient is generally a function of angle of attack, control deflection, Mach number, Reynolds number and local flow conditions:

$$C_h = C_h\left(\alpha, \delta, M_\infty, Re, \text{flow state}\right). \tag{3.2}$$

To reduce the force required to move the surface, aerodynamic and mass balancing devices are often introduced in reversible systems.

Static or mass balancing consists in placing suitable balancing masses so that the center of gravity of the movable surface lies close to the hinge axis. This reduces the inertial reactions transmitted to the pilot and helps prevent control surface flutter. Aerodynamic balancing, instead, aims to reduce the aerodynamic hinge moment by modifying the geometry of the control surface or by adding auxiliary surfaces.

Typical aerodynamic balancing solutions include horn balances, inset hinges, internal balances and balance tabs. A horn balance places a portion of the movable surface ahead of the hinge line. The aerodynamic force generated on this forward portion produces a hinge moment opposite to the hinge moment generated by the rest of the surface. As a result, the pilot force required to deflect the surface is reduced. However, excessive aerodynamic balancing must be avoided, because it can reduce the natural feel of the control and may lead to overbalanced or unstable control behaviour.

Another common solution is the use of tabs. A tab is a small auxiliary surface located near the trailing edge of a main control surface. Depending on its function, it may be used as a trim tab, balance tab, servo tab or anti-servo tab. A balance tab deflects in such a way as to reduce the hinge moment of the main surface, whereas a trim tab allows the pilot to maintain a steady control surface position with reduced or zero control force.

3.1.2 Irreversible flight control system

In powered or irreversible flight control systems, the pilot no longer provides the mechanical power required to move the control surface. The pilot command is transmitted to a servomechanism, while hydraulic, electrohydraulic or electromechanical actuators provide the power necessary to overcome the aerodynamic hinge moments. In this architecture, the aerodynamic loads acting on the surface are not directly fed back to the pilot through the control linkage.

Powered controls are essential for large aircraft, high speed aircraft and high performance combat aircraft, where the required control forces can exceed human capability. They also provide important advantages in terms of stiffness and control surface positioning. With the control command fixed, the actuator can hold the surface against external aerodynamic loads. With the command released, the artificial feel and centering system can bring the control device toward a neutral or trimmed position.

Since irreversible powered systems remove the natural aerodynamic feedback that would be felt by the pilot, an artificial feel system is required. The artificial feel system recreates a force displacement relationship at the cockpit control in order to provide the pilot with an appropriate perception of speed, load factor, manoeuvre intensity and control margin. Without artificial feel, the pilot could overcontrol the aircraft, especially at high dynamic pressure, where small control surface deflections can generate large aerodynamic loads.

Modern aircraft often use fly-by-wire flight control systems. In a fly-by-wire system, the pilot input is converted into an electrical signal and sent to one or more flight control computers. The computers process the command according to predefined control laws, sensor feedback, stability augmentation requirements, flight envelope protections and control allocation logic. The resulting commands are then sent to the actuators that move the control surfaces.

Fly-by-wire systems provide several advantages. They allow artificial stability to be introduced in aircraft with relaxed or negative static stability, improve handling qualities, reduce pilot workload, filter undesirable commands, prevent exceedance of structural or aerodynamic limits and coordinate multiple control effectors. In highly integrated aircraft, the flight control computer can also allocate the requested moment among several surfaces in order to minimize drag, avoid saturation, reduce structural loads or preserve low observability constraints.

The trim function is also part of the flight control system. Trim systems allow the aircraft to maintain a prescribed flight condition without requiring a continuous control force from the pilot. In reversible systems, trim can be achieved by using trim tabs or adjustable stabilizers to reduce or cancel the hinge moment felt at the cockpit. In powered or fly-by-wire systems, trim can be implemented by modifying the neutral position of the artificial feel system, by changing the actuator command bias or by scheduling the control laws according to the selected flight condition.

3.2 Conventional control surfaces

In a conventional aircraft configuration, stability and control are primarily achieved through dedicated aerodynamic surfaces. These devices operate by changing the local pressure distribution over the aircraft: a control surface deflection modifies the local camber or incidence of the lifting surface, generating an aerodynamic force increment which, through its moment arm with respect to the centre of gravity, produces the required pitching, rolling or yawing moment. Conventional control surfaces are divided into:

- Primary control surfaces, namely those that act directly on the control of the aircraft attitude:
  - Ailerons: control the rolling motion (roll, rotation about the longitudinal x-axis)
  - Elevators: control the pitching motion (pitch, rotation about the lateral y-axis)
  - Rudder: controls the yawing motion (yaw, rotation about the vertical z-axis)
- Secondary control surfaces, namely those that do not act directly on the control of the aircraft attitude but modify its management:
  - High lift devices: allow the lifting capability of the wing to be increased
    * Leading edge high lift devices (slats): allow the airfoil to stall at higher angles of attack by energizing the flow over the upper surface.
    * Trailing edge high lift devices (flaps): modify the camber of the airfoil and therefore provide an increase in lift
  - Spoilers: cause a loss of lifting capability on the wing, thus reducing the aerodynamic efficiency of the aircraft. They are used during descent before landing or once on the ground, to press the aircraft onto the runway and increase the effectiveness of the brakes. They assist lateral control when actuated independently and jointly with the ailerons.
  - Airbrakes: are used to decelerate the aircraft by increasing drag.

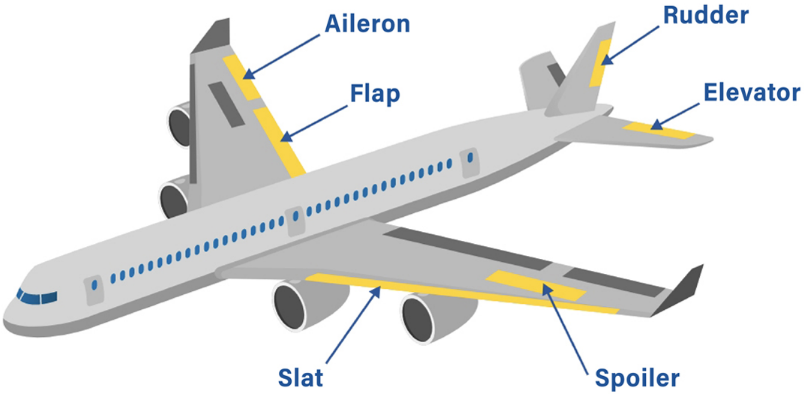

Figure 3.1: Scheme of conventional control surfaces.

3.2.1 Pitch stability and control

In the longitudinal plane, pitch stability and control are mainly governed by the capability of the aircraft to generate an adequate pitching moment about the center of gravity. In conventional and highly swept configurations, this pitching moment can be produced either by an aft horizontal tail or by a forward canard surface. Although both devices can provide longitudinal control, their effectiveness at high angle of attack is strongly affected by their position with respect to the separated flow field generated by the wing and fuselage.

For an aft-tail configuration, the local flow reaching the horizontal tail is influenced by the wing downwash. If ε_H denotes the downwash angle at the tail location and η_H the tail incidence or control angle, the effective angle of attack seen by the tail can be written as:

$$\alpha_{H,\text{eff}} = \alpha - \varepsilon_H + \eta_H. \tag{3.3}$$

The tail can generate an effective pitching moment only as long as its local effective angle of attack remains within the aerodynamic operating range of the surface. By imposing the limit condition:

$$-\alpha_{\text{eff,max}} \leq \alpha_{H,\text{eff}} \leq \alpha_{\text{eff,max}}, \tag{3.4}$$

the admissible range of tail incidence can be expressed as:

$$\eta_{H,\max} = -(\alpha - \varepsilon_H) + \alpha_{\text{eff,max}}, \tag{3.5}$$

$$\eta_{H,\min} = -(\alpha - \varepsilon_H) - \alpha_{\text{eff,max}}. \tag{3.6}$$

These two limits define the longitudinal trimmability region of the aft-tail configuration. Inside this region, the tail can still produce a useful aerodynamic load and therefore a useful pitching moment. Outside this region, the required tail incidence would force the tail beyond its effective aerodynamic range; consequently, the aircraft may no longer be trimmable in pitch.

At low and moderate angles of attack, the downwash angle generally increases with α, and the tail remains sufficiently effective. At high angles of attack, however, the wing flow becomes increasingly separated and the wake is displaced relative to the tail. As a result, the local flow at the tail may become highly distorted, with a reduction in local dynamic pressure and a strong variation of ε_H. This can lead to a loss of pitch control authority even if the tail surface itself has a large geometric deflection range.

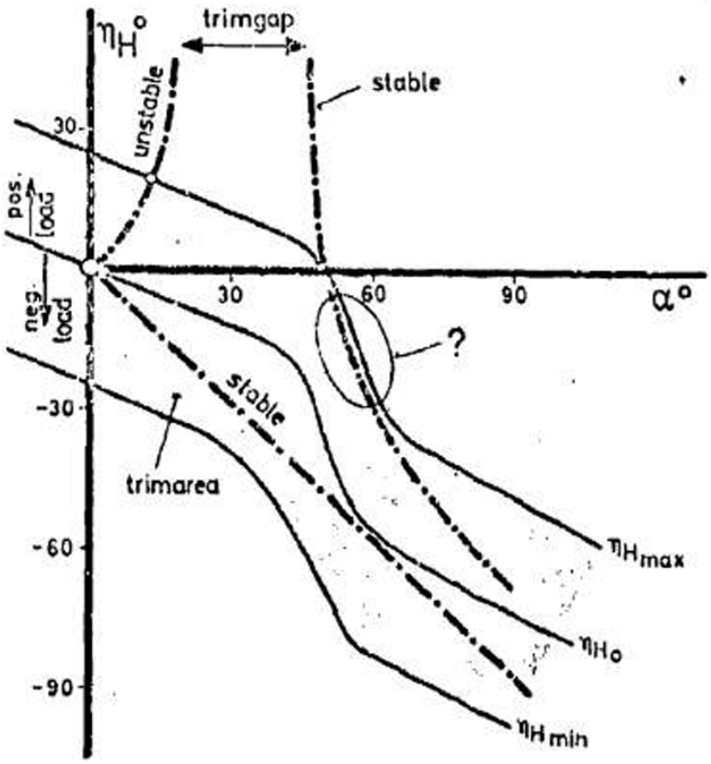

Figure 3.2: Region of trimmability for a trapezoidal wing with aft tail, considering 5% stable and 5% unstable center of gravity locations [11].

The comparison between stable and unstable center of gravity locations highlights the compromise between trim capability and aerodynamic efficiency. A statically stable configuration, with the center of gravity ahead of the neutral point, generally provides better natural pitch stability and maintains a wider trimmability margin at high angles of attack. However, it usually requires a larger balancing tail load in the conventional angle of attack regime, which increases trim drag.

By contrast, a statically unstable or relaxed stability configuration can reduce trim drag and improve maneuverability at conventional angles of attack, since smaller stabilizing tail loads are required. Nevertheless, when the angle of attack increases and the tail becomes affected by the separated wake of the wing, the available pitch control margin can decrease rapidly. Therefore, for an aft-tail aircraft, the configuration that is aerodynamically preferable from a drag point of view may not be the same configuration that guarantees pitch controllability over the whole high angle of attack range.

A different behavior is obtained when the longitudinal control surface is placed ahead of the wing, as in a canard configuration. In this case, the surface is not immersed in the wake of the main wing. The key aerodynamic parameter is no longer the downwash at the tail, but the upwash field induced at the canard position. The canard therefore operates in a cleaner flow environment and can retain a significant control effectiveness even when the main wing is already dominated by separated flow structures and leading edge vortices.

From a pitching moment point of view, the canard produces a moment contribution with an opposite lever arm arrangement compared with an aft tail. Since it is located ahead of the center of gravity, a positive lift increment on the canard tends to generate a nose up pitching moment, whereas a positive lift increment on an aft tail generally produces a nose down contribution. For this reason, the trim trends of canard configurations are essentially reversed with respect to aft-tail configurations.

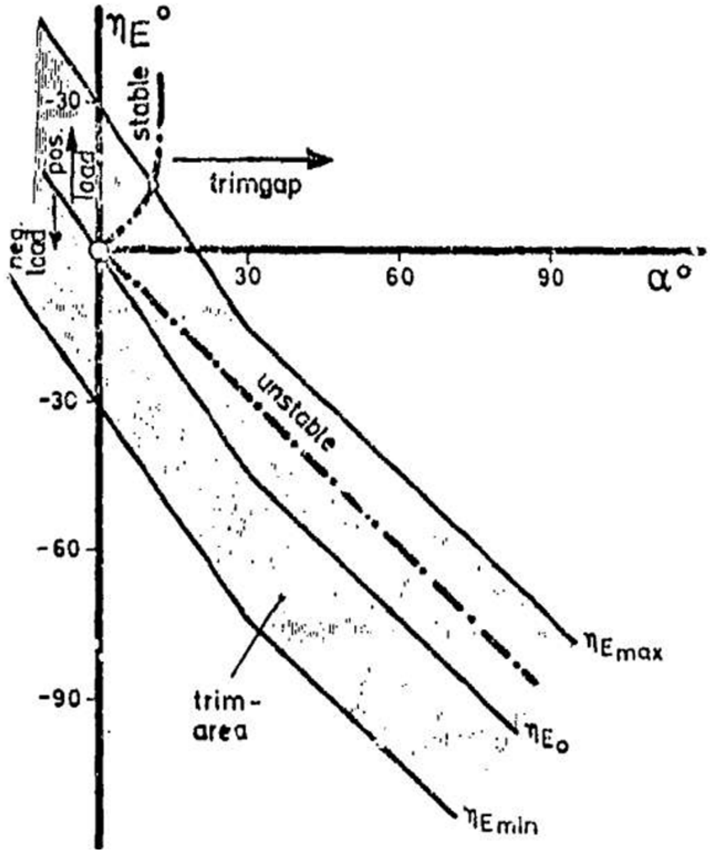

Figure 3.3: Region of trimmability for a delta wing with canard, considering 5% stable and 5% unstable center-of-gravity locations [11].

For the canard case, the stable configuration may become difficult to control at medium and high angles of attack, while the unstable configuration can maintain satisfactory trim and control margins over a wider incidence range. This result is particularly relevant for high performance combat aircraft, where relaxed static stability can be accepted if adequate artificial stability is provided by the flight control system.

An additional advantage of the canard arrangement is that the trailing edge of the main wing can be used more effectively for trim and control purposes, without relying on an aft tail immersed in the wing wake. This can improve the induced drag polar at conventional angles of attack while preserving longitudinal control capability at higher incidence. However, the canard also introduces additional aerodynamic interactions with the main wing, especially through its vortex system, and its integration must therefore be carefully optimized in terms of position, size, incidence range and compatibility with the overall aircraft layout.

In summary, pitch control at high angle of attack is not governed only by the maximum deflection capability of the control surface, but also by the local flow quality at the surface location. Aft tails can suffer from wake immersion and loss of dynamic pressure, whereas canards may preserve control authority by operating upstream of the main separated flow. This explains why nonconventional longitudinal control arrangements are of particular interest for highly maneuverable aircraft operating beyond the conventional linear aerodynamic regime.

3.2.2 Roll stability and control

Roll stability and control are associated with the capability of the aircraft to generate and regulate a rolling moment about the longitudinal axis. In conventional aircraft, roll control is mainly provided by the ailerons, which are deflected differentially in order to modify the lift distribution between the two wing halves. The resulting lift imbalance produces a rolling moment and allows the aircraft to change its bank angle.

The roll control effectiveness can be expressed through the derivative:

$$C_{l_{\delta_a}} = \frac{\partial C_l}{\partial \delta_a}, \tag{3.7}$$

where C_l is the rolling moment coefficient and δ_a is the aileron deflection angle. In attached flow conditions, ailerons usually provide a sufficiently linear and predictable roll response. However, at high angle of attack, their effectiveness can decrease significantly because the outer part of the wing may be affected by separation, vortex interaction or local stall.

This limitation is particularly important for delta and highly swept wings. In these configurations, the flow field at high incidence is dominated by leading edge vortices and by their possible breakdown over the wing. Since ailerons are generally located near the trailing edge and toward the outer part of the wing, they may operate in a strongly separated and distorted flow region. As a result, the expected lift increment due to aileron deflection can be strongly reduced.

For a delta wing configuration, ailerons were found to lose a large part of their effectiveness after stall, with the available roll control power decreasing to a small fraction of its initial value. Beyond stall, the down going aileron may further promote local separation instead of producing the desired lift increase, while the up going aileron can still reduce lift locally and therefore contribute to the rolling moment. Consequently, the rolling moment available in post stall conditions may be produced mainly by the up going aileron, making conventional ailerons insufficient as the only roll control device.

Alternative roll control strategies can therefore become necessary. One promising solution is differential tail deflection. If the horizontal tail remains in a sufficiently effective flow region along the trimmed flight condition, a differential deflection of the two tail halves can generate an asymmetric aerodynamic load and therefore a useful rolling moment. Compared with ailerons, this solution can retain good effectiveness over a wider range of incidence, provided that the tail is not completely immersed in separated wake flow.

Differential canard deflection can also be considered as a possible roll control mechanism. However, its effectiveness may be limited by the aerodynamic interaction between the canard and the main wing. In particular, the rolling moment generated directly by the canard can be partially cancelled by the modification of the downwash and vortex field at the wing location. Therefore, differential canards do not necessarily provide a strong net roll control contribution, unless their position and aerodynamic coupling with the wing are carefully optimized.

Another effective concept is represented by differential wingeron deflection, namely the rotation of wing portions rather than the deflection of a conventional hinged surface. Since a larger part of the lifting surface is directly involved in the motion, wingerons can generate significant rolling moments. Nevertheless, their use may introduce longitudinal trim penalties because a wing rotation also modifies the overall lift and pitching moment characteristics of the aircraft. Therefore, wingerons can be a suitable roll control solution only if the associated trim effects can be compensated.

Roll stability is instead related to the tendency of the aircraft to generate a restoring rolling moment after a sideslip disturbance. It is commonly described through the derivative:

$$C_{l_\beta} = \frac{\partial C_l}{\partial \beta}, \tag{3.8}$$

where β is the sideslip angle. Depending on the adopted sign convention, roll stability corresponds to the sign of C_{l_β} that produces a restoring rolling moment. In conventional aircraft, this stabilizing tendency is usually obtained through positive wing dihedral, a high wing arrangement or suitable vertical tail and fuselage contributions. In the presence of sideslip, one wing half experiences a different effective incidence than the other, producing a lift imbalance that tends to reduce the disturbance.

At high angle of attack, however, the conventional interpretation based on dihedral effect becomes less sufficient. For highly swept wings, delta wings and strake wing configurations, the flow field is dominated by leading edge vortices. The roll stability characteristics are then strongly influenced by the position, strength and breakdown of these vortices. In sideslip, the vortex system can become asymmetric: the vortex on one side may burst earlier or closer to the apex than the vortex on the opposite side. This asymmetric vortex breakdown produces an asymmetric pressure distribution over the wing and can generate destabilizing rolling moments.

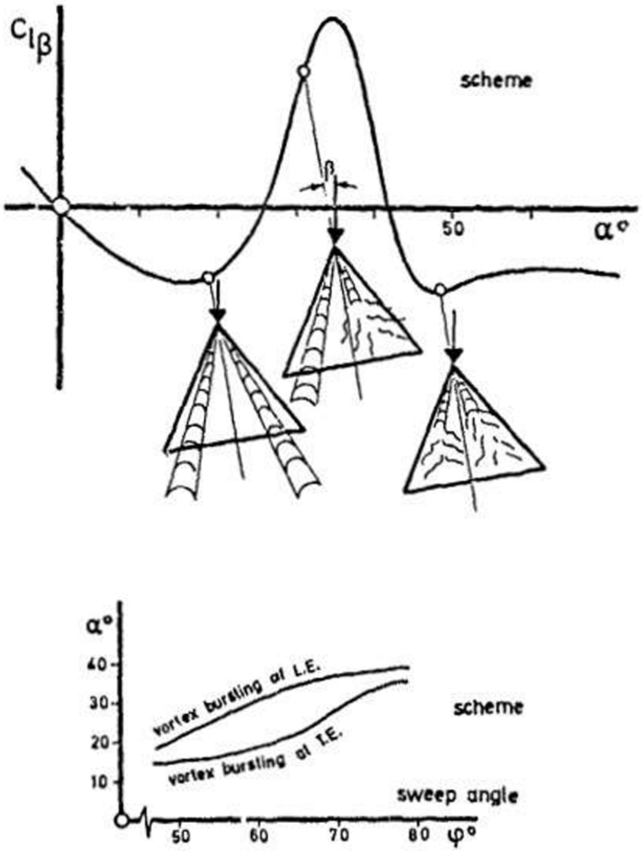

Figure 3.4: Roll instability of a delta wing caused by asymmetric vortex breakdown in sideslip conditions [11].

The typical trend of the roll stability derivative with angle of attack is therefore highly nonlinear. A destabilizing peak can appear slightly beyond stall, when the breakdown of the leading edge vortices becomes asymmetric. This phenomenon is particularly critical because it may occur in the same incidence range in which the aircraft requires large control authority to remain controllable. Consequently, roll instability at high angle of attack is not only a static stability issue, but also a control problem, since the available control surfaces must be able to counteract nonlinear vortex induced moments.

From a physical point of view, any device capable of controlling the vortex breakdown position can contribute to roll stability improvement. A suitable device may force an earlier and more symmetric vortex breakdown on both sides of the wing, delay the breakdown on the more critical side, or modify the local flow topology in order to reduce the asymmetry generated by sideslip. In this sense, roll stability at high incidence is closely connected to vortex management.

One possible solution consists in using spoilers placed ahead of the trailing edge flaps and deployed at high deflection angles near the maximum angle of attack. Spoilers locally disturb the upper surface flow and can promote a more controlled vortex breakdown. As shown schematically in Figure 3.5, this produces a stabilizing effect on the roll stability curve, reducing the destabilizing peak associated with asymmetric vortex bursting.

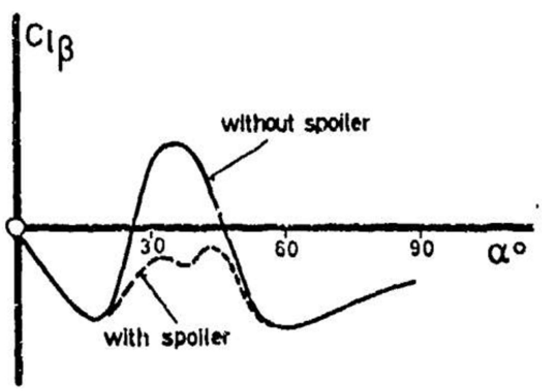

Figure 3.5: Effect of spoiler deployment on the roll stability characteristics at high angle of attack [11].

The main drawback of spoiler deployment is the associated drag penalty. Since spoilers intentionally disturb or separate the flow, they can improve roll stability but at the cost of a significant increase in drag and a possible loss of lift. A similar stabilizing effect can be obtained by rotating the trailing edge flaps upward, which reduces the local lift and modifies the vortex breakdown pattern. However, this solution also introduces a lift penalty and must therefore be evaluated in relation to the required maneuvering condition.

Leading edge flaps represent another possible solution. By modifying the leading edge separation process, they can delay vortex breakdown and reduce the tendency toward asymmetric bursting. Their effectiveness, however, can be influenced by the simultaneous use of trailing edge devices. In fact, an increase in circulation generated by trailing edge flaps may alter the vortex system and partially neutralize the stabilizing effect of the leading edge flaps.

Finally, additional concepts such as wingerons and vented fins can also contribute to roll stability and control. Wingerons act directly on the lifting surface and can generate strong rolling moments, while vented fins can modify the coupled yaw roll response of the aircraft. Since roll and yaw are strongly coupled at high incidence, devices that primarily improve yaw control may also produce beneficial effects on roll behavior, provided that the associated rolling moment is favorable and can be integrated within the flight control logic.

In summary, roll control at high angle of attack cannot rely exclusively on conventional ailerons, because their effectiveness may decrease drastically after stall and their response may become nonlinear. At the same time, roll stability is strongly affected by asymmetric vortex breakdown, especially on delta and highly swept wings. For this reason, effective high incidence roll control requires the combined management of aerodynamic control power and vortex behavior, through solutions such as differential tail deflection, wingerons, spoilers, leading edge flaps and properly integrated yaw roll control devices.

3.2.3 Yaw stability and control

Yaw stability and control are associated with the capability of the aircraft to generate a yawing moment about the vertical axis. In conventional configurations, directional stability is mainly provided by the vertical tail, while yaw control authority is generated by the rudder. When a sideslip perturbation occurs, the vertical tail produces an aerodynamic side force which, acting behind the center of gravity, generates a restoring yawing moment and tends to realign the aircraft with the incoming flow.

The directional static stability of the aircraft can be expressed through the derivative:

$$C_{n_\beta} = \frac{\partial C_n}{\partial \beta}, \tag{3.9}$$

where C_n is the yawing moment coefficient and β is the sideslip angle. With the usual aircraft sign convention, a positive value of C_{n_β} indicates a stable weathercock tendency, namely the tendency of the aircraft nose to rotate back toward the relative wind after a sideslip disturbance.

Yaw control authority, instead, is related to the yawing moment increment generated by a rudder deflection:

$$C_{n_{\delta_r}} = \frac{\partial C_n}{\partial \delta_r}, \tag{3.10}$$

where δ_r is the rudder deflection angle. The rudder produces a side force increment on the vertical tail and, due to the longitudinal distance between the tail and the center of gravity, this side force generates a yawing moment. Therefore, the effectiveness of the rudder depends on the local dynamic pressure at the tail, on the degree of flow attachment over the fin and rudder, and on the available moment arm.

At high angles of attack, conventional vertical tails and rudders may suffer a strong loss of effectiveness. As the incidence increases, the forebody, fuselage and wing generate separated wakes and vortex structures which can partially or totally immerse the vertical tail. The local dynamic pressure at the fin may decrease, the flow may become highly non uniform and the rudder may no longer be able to produce a predictable side force. As a consequence, the yaw control power can decrease rapidly and the directional stability of the aircraft can be degraded.

This limitation is particularly critical for highly maneuverable aircraft, because yaw control is essential not only for heading control, but also for preventing departure from controlled flight. At high angle of attack, small sideslip perturbations can produce asymmetric vortex patterns over the forebody and wing, resulting in nonlinear side force, yawing moment and rolling moment. Therefore, a sufficient yaw control margin is required to suppress sideslip growth and to maintain controllability in post stall or near post stall conditions.

Several alternative vertical surface arrangements can be considered to improve yaw stability and control at high incidence. The use of twin fins or canted fins may improve integration and reduce some aerodynamic penalties, but simply changing the dihedral angle or the longitudinal position of the fins does not necessarily guarantee a significant improvement in yaw control power over the whole angle of attack range. If the fins remain immersed in the separated wake, their effectiveness is still limited by the poor local flow quality.

For delta wing configurations, a more effective solution consists in placing fins and rudders below the wing, approximately at an intermediate spanwise position. In this region, the surfaces can operate in a flow field less affected by the upper surface separated wake and can therefore experience a more nearly constant local dynamic pressure even at high angles of attack. This arrangement can provide a beneficial contribution both to directional stability and to yaw control authority.

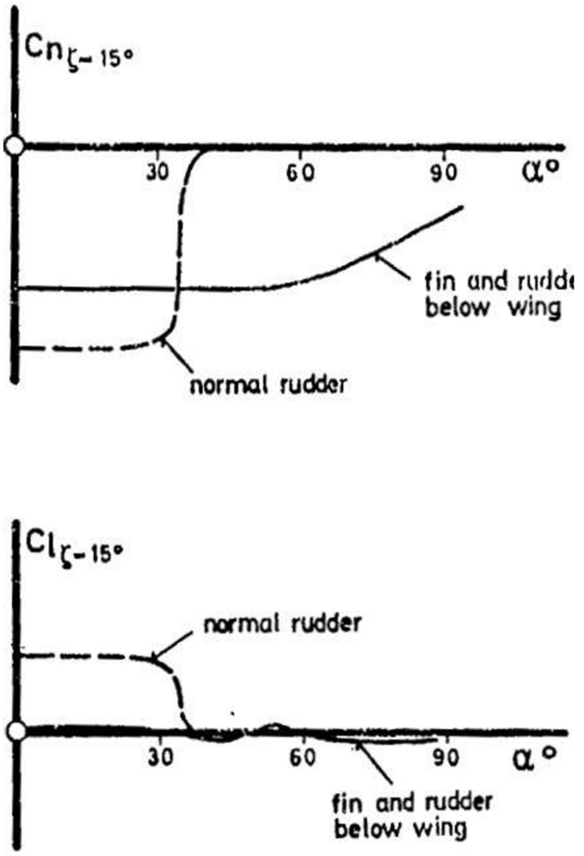

Figure 3.6: Yaw control power and rolling moment generated by fins and rudders located below a delta wing [11].

The comparison with a conventional rudder shows that the below wing fin arrangement can preserve yaw control effectiveness at higher angles of attack, where a normal rudder tends to lose authority. Moreover, the associated rolling moment can be favorable for the maneuver, producing a proverse roll contribution rather than a strong adverse coupling. This aspect is important because, at high incidence, yaw and roll are strongly coupled: a yaw control input that generates an excessive adverse rolling moment may become difficult to use effectively within the flight control system.

Despite these aerodynamic advantages, the installation of fins below the wing introduces important integration constraints. In particular, the presence of lower vertical surfaces may create difficulties in terms of ground clearance during takeoff and landing. For this reason, although the concept is aerodynamically attractive, its practical implementation must also consider landing gear height, rotation angle during takeoff, structural integration and operational constraints.

For trapezoidal wing configurations, another solution consists in using a vented fin connecting the wing and the horizontal tail. In this arrangement, the tail can be rotated downward at high angles of attack for trim purposes, so that the fin and rudder may still receive a relatively attached flow. However, the effectiveness of the lower rudder can decrease at high incidence because of the sweep of the rudder hinge line and the local orientation of the flow. To overcome this limitation, an additional rudder can be installed on the upper part of the fin, ensuring yaw control capability when the lower rudder becomes progressively less effective.

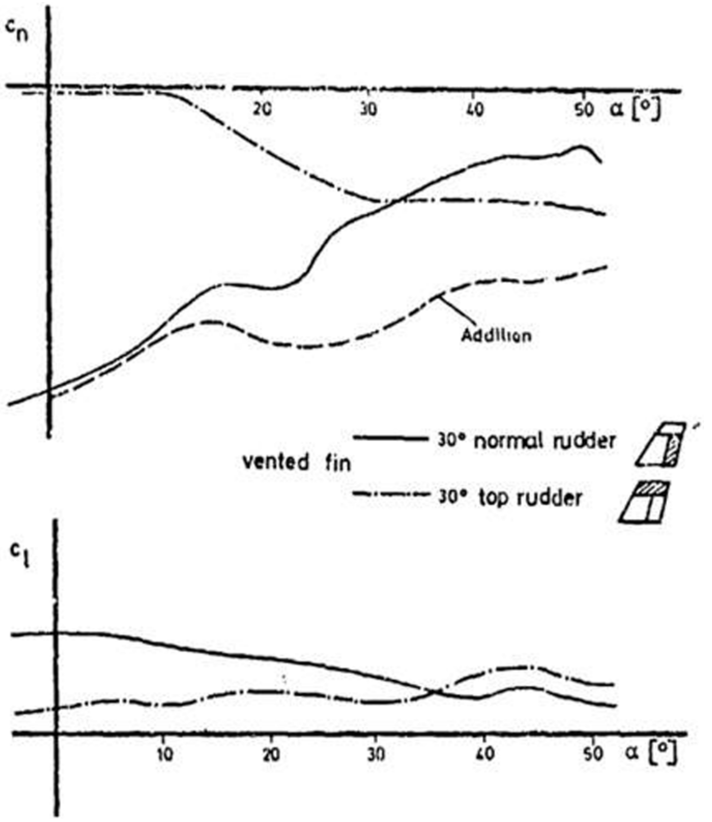

Figure 3.7: Yaw control characteristics of a vented fin configuration with lower and upper rudder contributions [11].

The vented fin configuration therefore provides an interesting compromise between directional stability and yaw control authority. The lower rudder can be effective over part of the angle of attack range, while the upper rudder contributes when the lower surface loses effectiveness. The combined use of the two rudders increases the available yawing moment and extends the controllable range of the aircraft.

Yaw control capability can also be improved by using canards with positive dihedral and differential deflection. In this case, the differential canard deflection produces asymmetric aerodynamic loads on the two sides of the aircraft, generating both side force and yawing moment. When coupled with the rudder, this solution can improve yaw control effectiveness over a wide angle of attack range. However, the canard contribution must be carefully evaluated because it also introduces additional rolling moments and modifies the vortex interaction with the main wing.

Leading edge flaps can also influence directional behavior. By modifying the leading edge separation process and delaying the onset of strongly asymmetric vortex patterns, they can improve directional stability and postpone the angle of attack at which the aircraft becomes directionally unstable. However, their effect is mainly associated with the stability characteristics of the configuration rather than with a direct increase in yaw control power.

In summary, yaw stability and control at high angle of attack depend strongly on the location of the vertical surfaces relative to the separated flow field. Conventional vertical tails and rudders may lose effectiveness when immersed in the wake of the wing and fuselage. Alternative arrangements, such as below-wing fins, vented fins with multiple rudders, differential canards and leading-edge devices, can improve the directional behavior of the aircraft by preserving local dynamic pressure, reducing wake blanketing effects and increasing the available yawing-moment margin.

3.2.4 Limitations of conventional control surfaces

The effectiveness of a conventional control surface depends mainly on three factors: the local dynamic pressure, the degree of flow attachment, and the available moment arm.

Since the aerodynamic force generated by a deflected surface scales with the dynamic pressure, control authority naturally decreases at low speeds. At the same time, at high speeds or high dynamic pressure, the maximum allowable deflection may be limited by structural loads, hinge moments and aeroelastic constraints. Therefore, even before considering high-angle-of-attack effects, conventional control surfaces are intrinsically constrained by the flight condition and by structural integration requirements.

A more severe limitation appears when the control surface is immersed in separated or highly distorted flow. In attached-flow conditions, a deflection produces a predictable change in the pressure distribution. The control-surface effectiveness is usually high and approximately linear. A deflection of an elevator, aileron, rudder, elevon or other aerodynamic effector produces a predictable modification of the local pressure distribution. But, if separation occurs upstream of the surface, however, the control surface may no longer be able to effectively modify the outer flow field. As a result, the generated force and moment increments can decrease drastically, become nonlinear, or even change sign.

Elevators and horizontal tails may lose effectiveness when they are affected by the separated wake of the wing or fuselage. In conventional aft-tail configurations, the horizontal tail may experience a strong reduction of local dynamic pressure and a highly non-uniform inflow at high angles of attack. This reduces pitch-control authority and may limit the ability of the aircraft to trim at high incidence. Although all-moving tails can improve control power compared with hinged elevators, they still remain sensitive to the local flow quality and to the available moment arm.

Ailerons are also strongly affected by high-angle-of-attack conditions. Since they are usually located near the outer wing, their performance depends on the state of the flow in a region where tip effects, local separation and vortex interactions may be significant. When the outer wing approaches stall, a downward-deflected aileron may promote further separation instead of increasing lift. Consequently, the expected rolling moment may be reduced, while the associated drag imbalance can generate adverse yaw.

The vertical tail and rudder's effectiveness relies on the presence of sufficient dynamic pressure at the tail location and on a reasonably attached flow over the fin and rudder. At high angles of attack, however, the vertical tail can be partially immersed in the wake of the forebody, wing and fuselage. The resulting reduction of local dynamic pressure causes a loss of rudder effectiveness. In addition, the flow reaching the tail may be highly asymmetric and unsteady, producing nonlinear yawing-moment behaviour.

From a low-observability perspective, conventional control surfaces introduce additional penalties. Vertical and horizontal tails increase the external cross-sectional area of the aircraft and generate strong radar-scattering features. Hinged surfaces also introduce gaps, seams and discontinuities in the outer mold line, which must be carefully treated to reduce radar reflections. When such surfaces are deflected, the external shape of the aircraft changes and may become less compatible with stealth requirements. For this reason, low-observable aircraft tend to minimize vertical surfaces, align control-surface edges with planform features, and reduce discontinuities in the external geometry.

3.3 Passive flow-control solutions

Passive flow-control solutions are based on fixed geometric features which modify the natural development of the flow without requiring external energy input, sensors or actuators [11]. Their purpose is not to generate a directly commanded control moment, as in the case of movable control surfaces, but rather to improve the baseline aerodynamic behaviour of the aircraft by influencing separation, vortex formation, vortex position and vortex breakdown.

A properly designed passive feature can promote a more stable and repeatable vortex system, delay outboard separation, reduce abrupt pitch-up tendencies and preserve the effectiveness of downstream control effectors. However, since passive solutions are fixed, their effect cannot be adapted in real time to different flight conditions. Therefore, they are generally useful for improving the aerodynamic characteristics of the basic configuration, but they cannot fully replace active control effectors when large commanded manoeuvring moments are required.

For low-observable aircraft, passive solutions must also be evaluated from a configuration and signature perspective. Any discontinuity, protrusion or sharp geometric feature may alter the outer mold line and potentially introduce radar-scattering contributions. For this reason, passive flow-control devices for future fighter aircraft should be integrated as smoothly as possible within the planform, preferably by exploiting existing leading-edge breaks, chines, sweep changes or blended forebody-wing junctions.

3.3.1 Leading-edge shaping solutions

Leading-edge shaping solutions act directly on the mechanism that generates the leading-edge vortex. By modifying the local leading-edge sweep, radius, sharpness or continuity, it is possible to control where the flow separates, how the vortex forms and how it interacts with the rest of the wing.

The main objective of leading-edge shaping is to obtain a controlled and beneficial separation pattern. In particular, the designer may seek to stabilize the primary leading-edge vortex, delay vortex breakdown, reduce the growth of separated regions near the wing tip, or prevent the outboard portion of the wing from stalling prematurely. In this sense, leading-edge shaping is a passive method for influencing vortex lift and high-angle-of-attack stability.

Typical leading-edge shaping solutions include dogtooths, leading-edge root extensions, strakes, leading-edge cuffs and planform cranks. Although they differ geometrically, they share the same physical principle: they introduce a deliberate change in the local flow topology, forcing the formation of a controlled vortex or modifying the path of an existing one. Their effectiveness strongly depends on the wing sweep, aspect ratio, leading-edge radius, Reynolds number, Mach number and angle of attack.

Leading-edge cranks: Dogtooth

A dogtooth [12] is a localized discontinuity or notch in the leading edge of the wing as shown in the figure .

Figure 3.8: A dog's tooth on the wing of an unmanned aircraft [12].

It is usually placed at an intermediate spanwise station and produces a concentrated vortex that develops over the upper surface of the wing. This vortex behaves like a passive aerodynamic barrier: it reduces the tendency of the boundary layer and separated flow to move spanwise toward the tip and can therefore delay outboard separation. By generating a localized vortex, the dogtooth can energize the flow over the outer panel and preserve the effectiveness of ailerons, elevons or other outboard control devices.

The aerodynamic role of the dogtooth is particularly important at moderate and high angles of attack. In these conditions, the outer wing is often more vulnerable to separation because of the combined effect of local loading, tip vortex influence and spanwise flow.

From a control perspective, the dogtooth does not directly generate a commanded moment. Instead, it improves the quality and repeatability of the flow field in which the control effectors operate. Its contribution is therefore indirect: a more stable vortex system reduces abrupt nonlinearities and can make the aircraft response more predictable.

The main limitation of the dogtooth is that its effect is fixed by geometry. A dogtooth optimized for a certain range of angles of attack may be less beneficial, or even penalizing, in other regimes. It can also introduce additional drag and local radar-scattering features if it is not carefully aligned with the planform. For this reason, in a low-observable design, the dogtooth concept must be integrated with the overall edge-alignment strategy of the aircraft.

Leading Edge Extensions: LERX and Strakes

Leading-edge root extensions [13] (LERX) and strakes are highly swept extensions located near the wing root or along the forebody-wing junction. Their main function is to generate strong, stable vortices that pass over the upper surface of the wing and create a low-pressure region that contributes to lift generation and delays massive separation at high angles of attack.

Figure 3.9: McDonnell Douglas F/A-18 Hornet [13].

At low and moderate angles of attack, the aerodynamic effect of a LERX may be limited. As the angle of attack increases, however, the flow separates from the sharp or highly swept extension and rolls up into a coherent vortex. This vortex can interact with the main wing leading-edge vortex, increasing suction over the inboard and mid-span portions of the wing. The result is an increase in vortex lift and a smoother progression toward high-angle-of-attack conditions.

In tailless and low-observable configurations, the use of LERX-like devices must be considered carefully. Classical protruding strakes may be incompatible with strict stealth requirements if they introduce additional edges or discontinuities. However, the same aerodynamic principle can be exploited through smoother forebody-wing blending, leading-edge cranks or chined geometries that preserve a continuous outer mold line while still promoting controlled vortex generation.

3.3.2 Forebody shaping solutions

When the nose and forward fuselage are highly inclined with respect to the free stream, the flow may separate along the forebody and form a pair of vortices [11]. In perfectly symmetric conditions these vortices should be symmetric, but in practice small disturbances, geometric imperfections or instability mechanisms can cause one vortex to become stronger than the other, generating an asymmetric pressure distribution that produces side force and yawing moment even when the aircraft has zero sideslip.

Forebody shaping solutions aim to control this phenomenon by influencing the formation, position and symmetry of the forebody vortices. The cross-sectional shape of the fuselage, the nose radius, the presence of chines, and the blending between forebody and wing all affect the way in which the separated flow develops.

A flattened or elliptical forebody can reduce the side area ahead of the centre of gravity and contribute to directional stability.

Chines are especially relevant for low-observable aircraft because they can serve both aerodynamic and signature-related purposes. Aerodynamically, they provide sharp or semi-sharp edges along which the flow can separate in a more controlled manner, generating controlled vortical structures that remain attached to the forebody edges and interact with the wing leading-edge vortices. From a stealth perspective, they can be aligned with the global planform edges, reducing uncontrolled geometric discontinuities and helping to preserve a coherent outer mold line.

Figure 3.10: Chined fuselage of an SR-71 Blackbird.

3.4 Active solutions: Innovative Control Effectors

Active solutions are control technologies capable of generating commanded aerodynamic or propulsive effects in response to flight-control inputs. Unlike passive devices, active control effectors can be scheduled, combined and allocated by the flight-control system according to the instantaneous flight condition, manoeuvre requirement and available control authority.

This feature is essential for tailless fighter aircraft, where the absence of horizontal and vertical tails strongly reduces the natural stability and control margins. Active solutions objective is to provide sufficient pitch, roll and yaw control while preserving stealth, reducing external discontinuities, limiting hinge moments and maintaining effectiveness at high angles of attack. They can be broadly divided into two families: mechanically actuated aerodynamic control effectors and flow-control effectors.

3.4.1 Aerodynamic Control Effectors

Aerodynamic control effectors generate control moments by modifying the pressure distribution over the airframe through mechanical deflection or deployment. They are conceptually close to conventional control surfaces, but their geometry, location and operating principle are adapted to the requirements of tailless and low-observable aircraft. In particular, they are designed to provide lateral-directional control without relying on a vertical tail.

The most relevant aerodynamic effectors for tailless fighter configurations include clamshells, all-moving wing tips, spoiler slot deflectors, deployable rudders and differential leading-edge flaps. These devices exploit different physical mechanisms: drag generation, local lift modification, vortex manipulation, spoiler-induced separation, or deployable side-force generation. Since each effector has advantages and limitations, the final aircraft configuration generally requires a combination of multiple effectors managed by a control allocation system.

Clamshell

The clamshell [1], also referred to as a drag rudder, is a split control surface usually located near the outer wing or wing tip. When deployed, the two panels open in a way that increases the local drag on one side of the aircraft. The resulting drag imbalance produces a yawing moment about the centre of gravity.

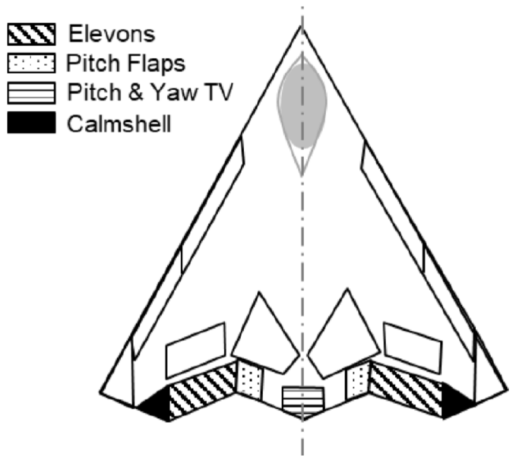

Figure 3.11: Configuration of clamshells and yaw control effectiveness at varying hinge-line sweep angles [1].

The main advantage of the clamshell is that it can provide yaw control without requiring a vertical tail, making it attractive for tailless and flying-wing configurations. Furthermore, since the clamshell is based primarily on drag generation, its yaw-control authority can remain relatively stable at high angles of attack and is less directly dependent on lift production than a conventional rudder.

However, the clamshell introduces important penalties. First, because it generates control through drag, its use is associated with an efficiency loss. Second, the drag increment may also produce an adverse rolling moment, particularly at high angle of attack, where lateral-directional coupling is strong. In addition, when deployed, the clamshell modifies the external shape of the aircraft and may introduce radar-signature penalties. For this reason, it is generally useful as a robust yaw-control device, but it is not necessarily the most efficient solution for highly agile low-observable fighters.

All Moving Wing Tip (AMT)

The All Moving Wing Tip (AMT) is an aerodynamic control effector in which the entire outer wing-tip portion rotates as a movable surface. This produces a significant modification of the local lift, drag and pressure distribution over the outboard wing.

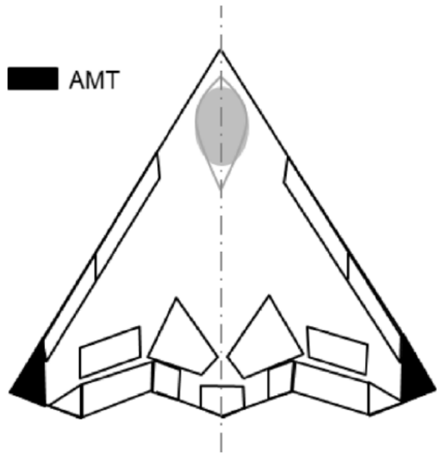

Figure 3.12: Configuration of AMT and yaw control effectiveness at varying deflection and AoA [1].

The AMT can contribute to both roll and yaw control. A differential deflection between the left and right tips produces an asymmetric lift distribution and therefore a rolling moment. At the same time, the modified lift and induced drag at the wing tip also generate a yawing moment. Because the AMT is located far from the aircraft centreline, even moderate aerodynamic force increments can generate significant control moments.

For tailless aircraft, the AMT is especially attractive because it provides lateral-directional authority without introducing a vertical surface. Its effectiveness can remain significant at high angles of attack, where conventional rudders may be immersed in separated flow or may not exist at all. Moreover, the AMT can be integrated into thin wing sections and may offer relatively low hinge moments compared with conventional rudder-type solutions. If the hinge line is properly sealed and aligned with the planform, the AMT can also be compatible with low-observable design requirements.

Nevertheless, the AMT introduces non-negligible design challenges. The first is control coupling: since the AMT modifies both lift and drag at the wing tip, a yaw-control input may also generate a rolling moment, and a roll-control input may also generate yaw. At low angles of attack, this coupling may be adverse and must be compensated by the flight-control system. The second challenge is structural. The moving tip must withstand aerodynamic loads, aeroelastic effects and actuation requirements while maintaining a precise external shape. Finally, at large deflections, the aerodynamic response may become nonlinear, especially when the local flow is separated.

For these reasons, the AMT is a multi-axis control effector. Its design requires careful selection of spanwise extension, hinge location, deflection range, actuation rate and integration with other control surfaces. It represents a promising solution for improving the manoeuvrability of tailless or highly swept configurations while preserving the low-observable advantages associated with the absence of conventional vertical tails.

AMT limitations

Although the All Moving Tip represents a promising non-conventional control effector, its limited diffusion in operational fighter aircraft is not mainly related to a lack of aerodynamic effectiveness. On the contrary, previous studies and the present numerical results show that the AMT can generate significant control moments, especially for lateral-directional control. Its limited adoption is instead mainly due to the fact that its integration introduces several critical issues at aircraft-system level.

A first limitation is associated with the aeroelastic behaviour of the wing-tip region. Since the AMT is installed at the outer portion of the wing, where the structure is generally more flexible than near the fuselage, its motion can strongly interact with wing bending and torsion. As a result, flutter, divergence and dynamic stability constraints may become design-driving aspects. This makes the AMT more critical than conventional all-moving surfaces, such as horizontal stabilators or canards, which are usually mounted on structurally stiffer regions of the aircraft.

A second important limitation concerns actuation. The AMT must rotate a relatively large movable surface located in a high-dynamic-pressure region and subjected to significant aerodynamic loads. Therefore, the required actuator must provide high torque, sufficient bandwidth, low weight, compact installation, redundancy and fail-safe behaviour. These requirements are particularly demanding in the wing-tip region, where the available volume is limited and where structural and system-integration constraints are severe.

Another relevant aspect is the strong coupling between the control axes. An asymmetric AMT deflection can generate yawing moment, but it usually also produces a rolling-moment contribution. Similarly, when the device is used for roll control, a non-negligible yawing-moment increment may appear because of the associated asymmetric drag. This means that the AMT cannot be treated as a pure single-axis control surface. Its use requires a proper control-allocation strategy, in which the AMT is coordinated with the other available effectors in order to obtain the desired aircraft response while limiting undesired coupling, saturation and excessive drag penalties.

From a low-observability perspective, the AMT also presents both advantages and drawbacks. On the one hand, it may help reduce or replace conventional vertical tails, which are usually penalizing for radar signature. On the other hand, a large moving wing-tip introduces gaps, hinge lines, discontinuities and deflected-edge orientations that may affect the radar cross section, especially during manoeuvres. Therefore, its stealth benefit is not automatic, but depends on a careful integration within the complete aircraft geometry.

For these reasons, the AMT should not be interpreted as a direct replacement for conventional control surfaces in existing fighter configurations. Its real potential appears stronger in future highly integrated, tailless or low-observable configurations, where several unconventional effectors may be combined within a multi-effector flight-control architecture. In this sense, the AMT is better regarded as an auxiliary or complementary control device, particularly suited to lateral-directional control, rather than as a universal primary control surface.

Spoiler Slot Deflector (SSD)

The Spoiler Slot Deflector (SSD) [1] is an aerodynamic control effector derived from the conventional spoiler concept. A standard spoiler operates by protruding into the flow over the upper wing surface, locally reducing lift and increasing drag. The SSD modifies this principle by combining a spoiler-like element with a slot-deflector arrangement, improving the pressure redistribution and making the control response more effective and more linear.

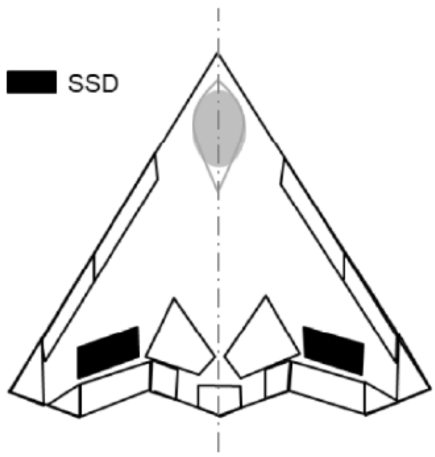

Figure 3.13: Configuration of SSD and lateral–directional control effectiveness of both SSD and conventional spoilers at varying AoA [1].

When the deployment is asymmetrical, this generates rolling and yawing moments. In tailless aircraft, this is useful because the SSD can provide lateral-directional control without requiring a conventional vertical tail. It can also reduce the risk of control reversal and improve the linearity between commanded deflection and generated aerodynamic moment.

The main disadvantage of the SSD is integration complexity. The system requires cutouts and internal volume within the wing, which can affect structural layout, stiffness and manufacturing complexity. Moreover, because the SSD modifies the flow over the wing, it may interact with elevons, trailing-edge flaps or other nearby effectors. In tailless aircraft, where pitch-control authority is often limited, any reduction in elevon effectiveness or increase in trim requirement must be carefully assessed. Therefore, the SSD is a promising lateral-directional effector, but its use must be evaluated together with the complete control-effector suite.

Deployable Rudder (DRUD)

The Deployable Rudder (DRUD) [1] is a control effector designed to provide yaw control by deploying a vertical or nearly vertical surface from the aircraft body or wing. When stowed, the surface remains hidden or integrated within the airframe, preserving the external low-observable shape. When deployed, it behaves similarly to a rudder or directional plate, generating side force and drag that produce a yawing moment.

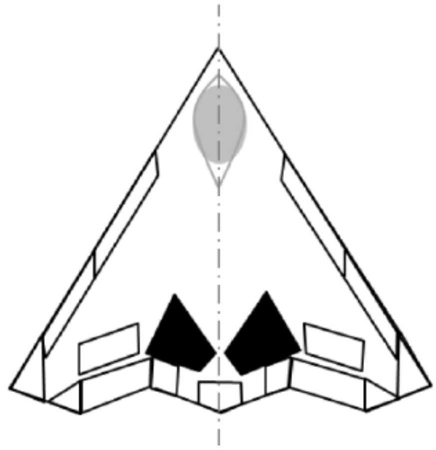

Figure 3.14: DRUD configuration, yawing moment generation principle, and lateral–directional control effectiveness at varying deflections and AoA [1].

The DRUD is particularly suited to low-speed, takeoff, landing and high-angle-of-attack conditions, where additional yaw authority may be required and where conventional aerodynamic control surfaces can be less effective. The generated yawing moment arises from the combination of lateral force (DRUD's lift) and axial force (DRUD's drug) acting at a certain distance from the centre of gravity. If the device is properly located, it can produce a relatively isolated yawing moment with limited rolling-moment contribution, especially at low and moderate angles of attack.

The effectiveness of a DRUD depends strongly on its placement. An aft location generally increases the yawing moment arm, while an inboard position may reduce undesirable interactions with leading-edge vortices and wing-tip flow. However, at high angles of attack the surrounding flow can be highly separated and vortical, so the deployed rudder may interact with the leading-edge vortex system. This can modify the local dynamic pressure and produce nonlinear variations in control effectiveness.

However, when deployed, it introduces a vertical surface and therefore a potential radar-signature penalty. Other design issues include actuator loads, structural stiffness, hinge integration, ground clearance for lower-surface installations, and the possible degradation of authority on the windward side at large sideslip or high angle of attack. The DRUD should therefore be considered as a supplementary yaw-control device rather than as a universal replacement for all directional-control requirements.

Differential Leading-Edge Flap (DLEF)

The Differential Leading-Edge Flap (DLEF) [1] is an active aerodynamic control effector based on asymmetric deflection of leading-edge flaps. Unlike a conventional leading-edge flap used only to improve lift or delay stall, the DLEF is used differentially between the two wings to manipulate the leading-edge vortex system and generate lateral-directional control moments.

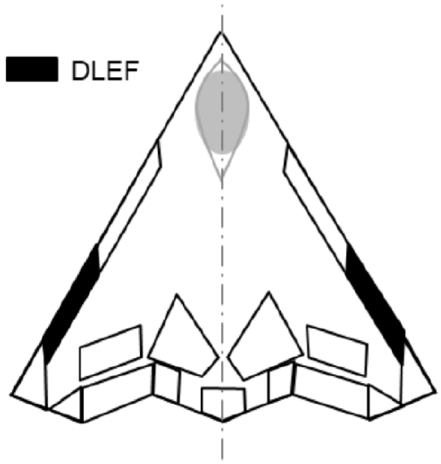

Figure 3.15: Configuration of DLEF and directional stability [1].

By deflecting the leading-edge flap on one side differently from the other, the aircraft can modify the strength, position and breakdown behaviour of the vortices over the two wings. This produces an asymmetric suction distribution, which can generate rolling and yawing moments.

The effectiveness of the DLEF is most relevant in the high-angle-of-attack regime, where vortical flow dominates the aircraft response. In this regime, the DLEF can reduce instability, improve roll performance and contribute to spin prevention or recovery.

The main limitation of the DLEF is that its behaviour is nonlinear and strongly dependent on the flight condition. A deflection that is beneficial at one angle of attack may have a different or weaker effect at another. For this reason, the DLEF requires careful gain scheduling and integration within the flight-control laws. In addition, negative deflections or large leading-edge gaps may be unfavourable from a low-observability perspective, because they can disturb the outer mold line and create additional scattering features. Therefore, the DLEF's practical use requires careful aerodynamic, structural and signature integration.

3.4.2 Flow Control Effectors

Flow control effectors generate control forces and moments by directly manipulating the flow field around the aircraft. They inject momentum, modify circulation, alter boundary-layer behaviour or deflect the engine jet. This makes them attractive for low-observable aircraft, because they can reduce the number, size or deflection of conventional moving surfaces.

Active flow control requires an external energy source, usually compressed or bleed air, and therefore introduces additional system-level constraints. Ducts, valves, nozzles, pressure losses, thermal effects, mass-flow requirements and reliability must be considered from the earliest design stages. However, flow control effectors can be highly responsive and can be integrated conformally into the aircraft surface, making them promising candidates for future tailless fighters.

Thrust Vectoring Control (TVC)

Thrust Vectoring Control (TVC) [1] consists of changing the direction of the propulsive jet in order to generate control forces and moments. If the thrust vector is deflected with respect to the aircraft centre of gravity, it produces a pitching, yawing or rolling moment depending on the direction of deflection and on the engine installation.

Unlike conventional aerodynamic surfaces, TVC does not require attached flow over the wing or tail to remain effective. This makes it particularly valuable at high angles of attack and in post-stall condition, where the propulsive jet can still be redirected to generate a useful control moment. In this sense, TVC can act as a complementary control effector that extends the controllable flight envelope.

TVC can be implemented through mechanical or fluidic concepts.

- Mechanical thrust vectoring uses movable nozzles [14], vanes or paddles to redirect the exhaust jet. This approach can provide large control authority, but it introduces weight, thermal and structural penalties, as well as moving parts in a region of high temperature and high mechanical loading. It may also be unfavourable for low observability because it modifies the external aft-body geometry.

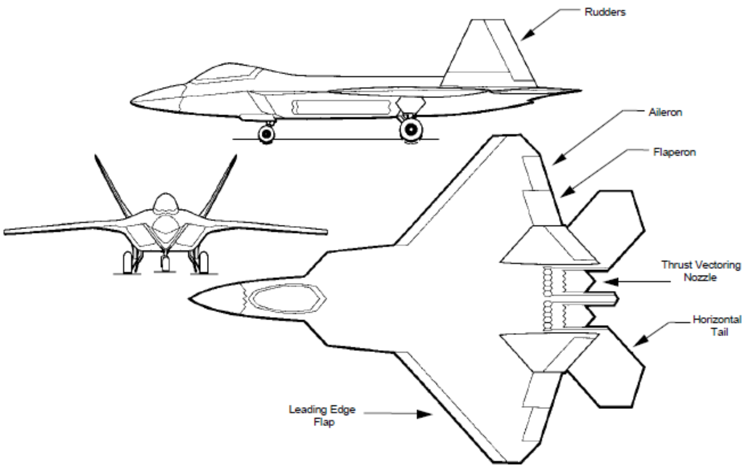

Figure 3.16: F-22 Three View [14].

- Fluidic thrust vectoring [1] uses secondary air injection to deflect the primary jet without large moving mechanical components. The secondary flow can modify the pressure distribution inside or near the nozzle, causing the exhaust jet to turn. In some concepts, the Coanda effect is exploited to make the jet attach to a curved or inclined reaction surface. Since the external geometry can remain more continuous, fluidic TVC is attractive for stealth-sensitive aircraft. It may also reduce mechanical complexity and maintenance requirements.

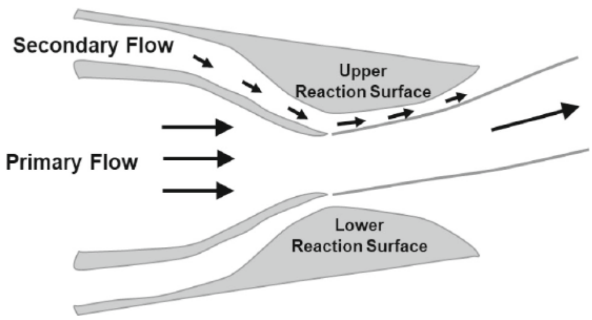

Figure 3.17: Fluidic thrust vectoring nozzle assembly and key features [1].

The main limitation of TVC is that its effectiveness is not uniform throughout the flight envelope. At high Mach number and high dynamic pressure, nozzle loads, thermal constraints and allowable vector angles may limit the available control moment. In addition, fluidic TVC requires pressurized air, ducting and valves, which impose propulsive and integration penalties. Therefore, its greatest value is obtained when it is combined with aerodynamic effectors through an integrated control allocation strategy.

Surface-Integrated Slot-Jets

Surface-integrated slot-jets [1] are active flow-control effectors based on the injection of high-pressure air through narrow slots embedded in the aircraft surface. The jets are generally oriented tangentially or nearly tangentially to the local surface, so that they interact with the boundary layer, separated shear layer or local vortical flow. By adding momentum to selected regions of the flow, they modify the local pressure distribution and generate control forces and moments.

A representative arrangement for a tailless configuration consists of slot-jet pairs located at the apex, along the mid-span leading edge and near the outboard trailing edge.

- Apex slot-jets can influence the forebody or leading-edge vortex system and are mainly associated with yaw control.
- Mid-span leading-edge slot-jets can modify the spanwise lift distribution and generate side-force contributions.
- Trailing-edge slot-jets can alter circulation over the aft portion of the wing, in a way that is analogous to a virtual flap deflection, and can therefore contribute to pitch and roll control.

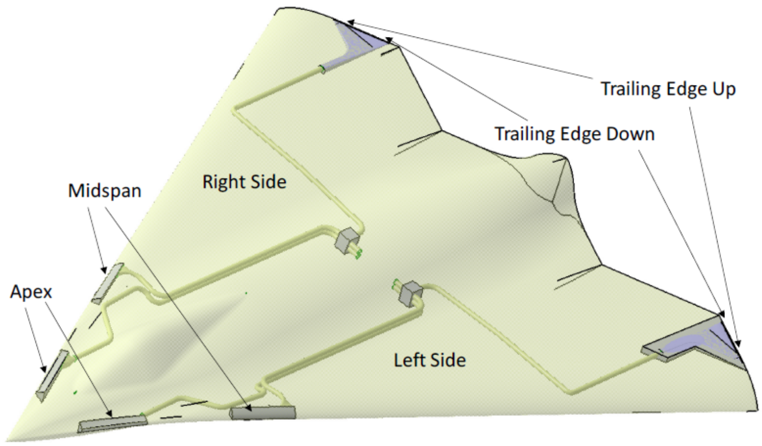

Figure 3.18: The ICE Simulation Model is Expanded to Include Active Flow Control Effectors [1].

The effectiveness of a slot-jet is commonly related to the momentum coefficient C_μ, which measures the jet momentum relative to the free-stream dynamic pressure and reference area. Increasing C_μ generally increases the control effect, but also increases the required mass flow and energy cost. For this reason, the design problem is not only aerodynamic, but also system-level: the aircraft must provide sufficient compressed air through ducts, valves and nozzles without unacceptable penalties in weight, volume, thermal management or engine performance.

Surface-integrated slot-jets are particularly attractive for low-observable aircraft because they can be conformal with the outer mold line and do not require large external deflections. When active, the aircraft shape can remain almost unchanged, because the control action is produced by the flow itself, offering great advantages in terms of radar signature.

However, several challenges remain. The jet performance depends strongly on slot geometry, jet orientation, pressure ratio, local boundary-layer state, Mach number and angle of attack. The system also requires reliable high-speed valves, internal ducting and an available source of pressurized air. In addition, the interaction between multiple slot-jets can be highly coupled: a jet intended for yaw control may also affect roll or pitch, especially at high angle of attack. For this reason, surface-integrated slot-jets require detailed aerodynamic characterization and must be managed by a robust control allocation system.

Overall, slot-jets represent one of the most promising active flow-control technologies for future tailless fighter aircraft. They can provide rapid, distributed and stealth-compatible control authority, especially when combined with aerodynamic effectors and thrust vectoring. Their practical implementation, however, depends on demonstrating sufficient control power with acceptable bleed-air demand, integration complexity and reliability.

Chapter 4

Case study: CFD Assessment of an All-Moving Tip Control Surface

4.1 Purpose of the numerical investigation

The present chapter is devoted to the numerical assessment of an All-Moving Tip (AMT) control surface installed on a swept semi-wing, representative of a high-performance combat aircraft configuration. The analysis is intended to provide a first aerodynamic evaluation of the AMT concept. The objective is not limited to the prediction of the global aerodynamic performance of the wing, but is mainly focused on the incremental effect produced by the AMT deflection on the aerodynamic loads and moments generated by the configuration.

The interest in the AMT control surface is closely related to the design of tailless or reduced-tail aircraft, where conventional vertical and horizontal tail surfaces may be reduced or eliminated in order to decrease radar observability and improve aerodynamic integration. In such configurations, the generation of adequate control moments becomes more complex, since the same set of lifting surfaces must often provide longitudinal, lateral and directional control. For this reason, innovative flow-control effectors have been investigated as possible means to recover control authority while preserving a compact and low-observable external shape.

Among these solutions, the AMT is particularly attractive because it is located in the outer portion of the wing, where the aerodynamic force generated by a deflected surface acts with a large moment arm with respect to the aircraft centreline, so even a relatively limited force increment may produce a significant contribution to the rolling and yawing moments.

Computational Fluid Dynamics (CFD) simulations are used in this work as a preliminary investigation tool, that allows the aerodynamic behaviour of the concept to be studied for different combinations of angle of attack α and AMT deflection angle δ_{AMT}. The resulting study is aimed to clarify how the AMT modifies the flow topology around the outer wing, to identify the main trends in the aerodynamic coefficients and to assess the control effectiveness.

A further objective of the numerical investigation is to relate the integral aerodynamic coefficients to the corresponding flow-field modifications, and interpret the origin of the force and moment increments with the pressure distribution on the wing and on the AMT, while velocity and vorticity fields are examined to understand the influence of the AMT on the vortex-flow structures.

The analysis presented in this chapter should therefore be interpreted as a first numerical validation of the AMT concept, that provides the aerodynamic foundation required to assess whether the selected AMT layout can generate meaningful control effects and whether its behaviour remains sufficiently regular over the investigated range of angles of attack.

4.2 Reference geometry and control-surface layout

The numerical investigation is carried out on a highly swept and low aspect ratio semi-wing, equipped with an All Moving Tip (AMT) control surface. The geometry was selected to represent, in a simplified form, the outer lifting surface of a combat aircraft, in which lateral-directional control is partly transferred from conventional tail surfaces to non-conventional wing-mounted effectors.

The following analysis is deliberately restricted to the isolated contribution of the AMT, in order to identify its main aerodynamic effects before considering more complex multi-effector control strategies.

4.2.1 Semi-wing CAD model

The reference geometry consists of a single semi-wing model, generated in the CAD environment of Ansys (DesignModeler) and subsequently imported into the CFD workflow of Ansys Fluent.

The wing planform is characterized by a highly swept leading edge and a tapered outer region, resulting in a slender configuration representative of high-speed aircraft layouts. The airfoil adopted for the whole wing is the NACA 0008, a symmetric and relatively thin profile. The use of a symmetric airfoil avoids the introduction of an intrinsic camber effect and makes the interpretation of the aerodynamic increments due to AMT deflection more direct.

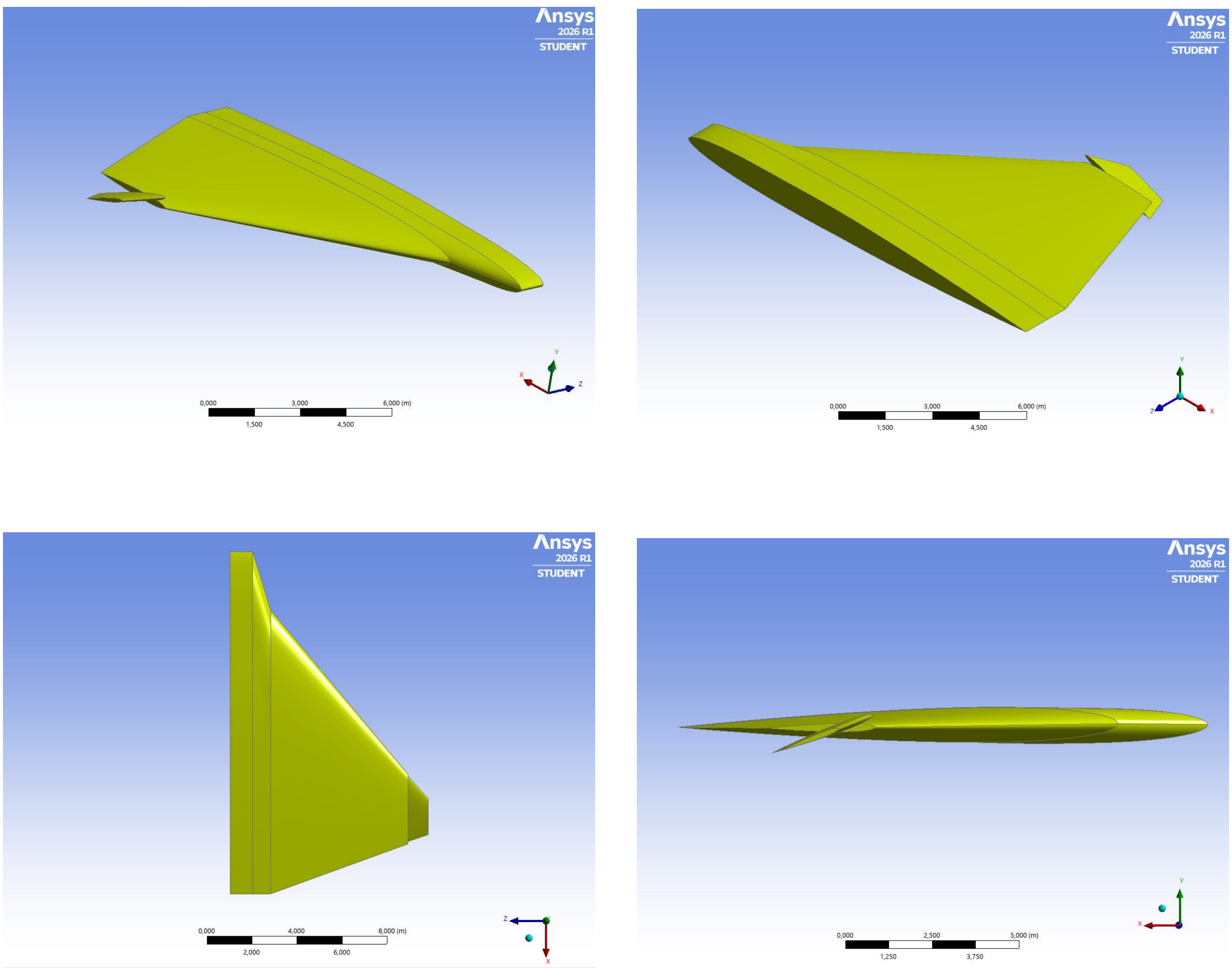

Figure 4.1: CAD Model visualization, with the AMT deflected at 20°.

The model is composed of a fixed inboard portion, representative of a wing-fuselage connection characterized by a leading edge extension, a fixed wing, representing the baseline lifting surface, and an outer movable tip that covers the final outboard portion of the semi-wing planform. The main geometric quantities of the CAD model, used in the CFD simulations, are summarized in Table 4.1.

Table 4.1: Main geometric parameters of the reference semi-wing and AMT layout.

Parameter	Symbol	Value
Semi-wing reference area	$S_{\mathrm{ref}}/2$	50 m^2
Semi-wing span	$b/2$	8.80 m
Root chord, including inboard extension	c_r	15.20 m
Tip chord	c_t	1.69 m
Mean aerodynamic chord	$\bar{c} = S_{\mathrm{ref}}/b$	5.68 m
AMT planform area	S_{AMT}	2.15 m^2
AMT spanwise extension	b_{AMT}	0.90 m
AMT-to-semi-wing area ratio	$S_{\mathrm{AMT}}/S_{\mathrm{ref}}$	4.30%

The reference area used for the aerodynamic coefficients corresponds to the planform area of the investigated semi-wing, excluding the inboard portion (wing-fuselage connection). Since the analysis is focused on incremental effects, the same reference area, reference length and moment reference point (the center of gravity of the entire body, considering both semi-wings, shown in Figure 4.2) are kept constant for all AMT deflections and all angles of attack.

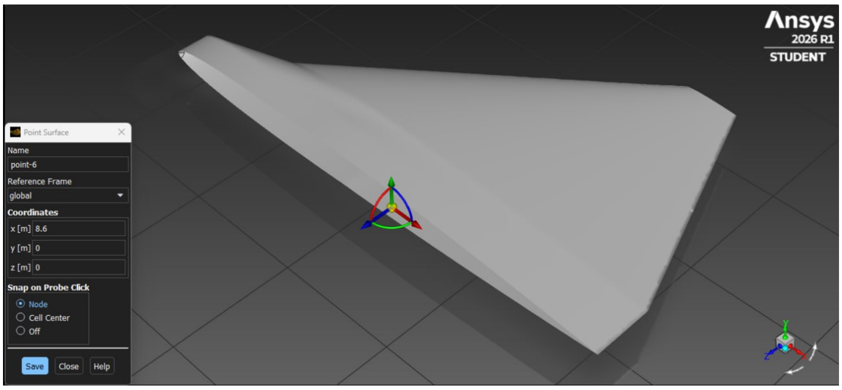

Figure 4.2: Fluent Reference Frame with moment reference point

The reference frame used for the numerical setup was defined with the origin positioned in the most upstream point of the wing. The X-axis is aligned with the main chordwise direction, from the leading edge towards the trailing edge, the Y-axis lies on the symmetry plane and is oriented in the vertical direction of the computational setup, while the Z-axis is normal to the symmetry plane and approximately aligned with the spanwise direction of the semi-wing. With this convention, the incoming flow direction can be prescribed by imposing the desired angle of attack through the velocity components at the far-field boundaries.

4.2.2 All-Moving Tip geometry and deflection convention

The All-Moving Tip (AMT) is located at the outer end of the semi-wing and occupies the final spanwise portion of the planform. It is modelled as a fully movable surface: an AMT deflection corresponds to a rigid rotation of the entire outboard panel about its hinge axis.

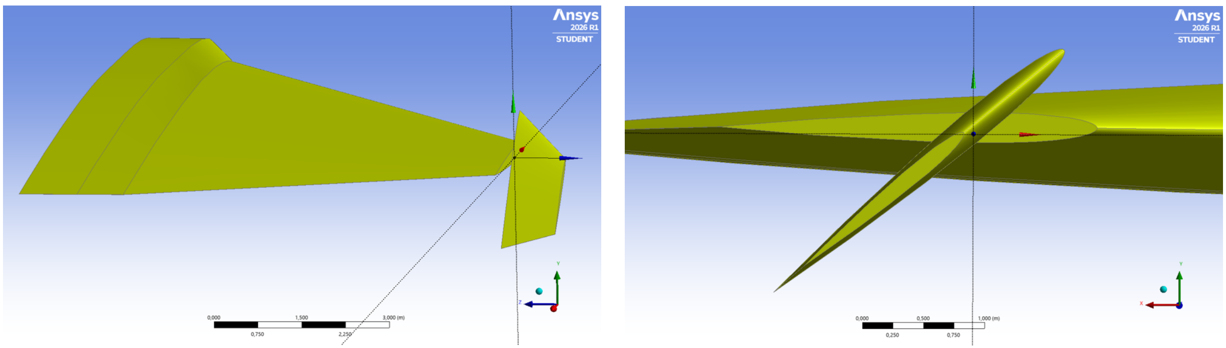

Figure 4.3: AMT hinge axis and reference frame used for the deflection convention.

The hinge line separates the fixed inboard wing from the rotating tip and it's shown in Figure 4.3. In the original Fluent coordinate system adopted for the CFD model, the hinge-axis reference point is located at $\mathbf{x}_H = (X_H,\ Y_H,\ Z_H) = (10.9,\ 0,\ -7.9)$ m. This point identifies the spanwise station at which the movable tip starts and was later used as the geometric reference for the AMT rotation in the CAD and mesh-generation process.

The AMT deflection angle is denoted by δ_{AMT} and is defined as the angular rotation of the movable tip with respect to the undeflected baseline configuration. According to the adopted convention, a positive AMT deflection corresponds to an upward rotation of the AMT leading edge. The undeflected condition, $\delta_{\mathrm{AMT}} = 0°$, corresponds to the clean wing geometry, in which the AMT is aligned with the fixed wing surface.

Although the AMT is analysed at different deflection angles, each deflected configuration is treated as a steady fixed geometry: the movable surface is rotated during the CAD and mesh setup and then kept stationary during the CFD calculation. Therefore, the simulations do not reproduce the transient motion of the AMT, but only the steady aerodynamic loads associated with prescribed deflection angles.

4.3 CFD methodology

4.3.1 Computational domain

The CFD simulations were performed by embedding the semi-wing geometry in a three-dimensional external-flow computational domain. The domain must be sufficiently large to prevent the outer boundaries from artificially influencing the pressure field, the wake development and the tip-vortex structure.

The adopted domain, shown in Figure 4.4, consists of an enclosure surrounding the semi-wing, defined by combining a rounded upstream cap with a cylindrical downstream region, starting from the most upstream point of the wing geometry. The upstream region is rounded, generated as a quarter-spherical surface, in order to provide a smooth far-field boundary and avoid sharp upstream corners in front of the wing. The downstream part is cylindrical, with the same radius of the spherical part, and extends in the streamwise direction to allow the wake and the vortical structures generated by the wing to develop without interacting prematurely with the outlet boundary. The domain was generated as a half-domain with respect to the wing root plane, which lies on the symmetry plane. In this way, only one half of the physical configuration is computed, reducing the computational cost. The main dimensions of the computational domain are summarized in Table 4.2.

Table 4.2: Main dimensions of the computational domain.

Quantity	**Symbol**	**Value**
Upstream rounded cap radius	R_{inlet}	170 m $\approx$ 11.18 c_r
Downstream domain length	L_{down}	300 m $\approx$ 19.74 c_r
Total streamwise domain length	L_{dom}	470 m $\approx$ 30.92 c_r

Using the Student license of ANSYS Fluent, the maximum number of mesh elements was limited to approximately 1 million. Therefore, the domain size was chosen as a compromise between physical accuracy and number of computational cells available. Increasing the distance between the wing and the far-field boundaries reduces the risk of artificial blockage effects and boundary-induced distortions of the aerodynamic loads, but also increases the number of cells required to discretize the peripheral regions of the domain, losing discretization and precision in the region around the wing.

The semi-wing was subtracted from the surrounding fluid volume, so that the final computational domain corresponds only to the air region around the solid geometry. A schematic representation of the computational domain is shown in Figure 4.4, that highlights the main external boundaries.

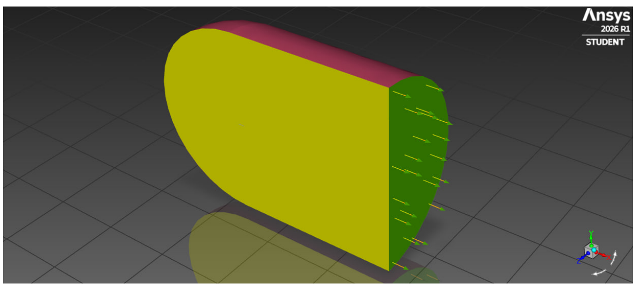

Figure 4.4: Computational domain adopted for the CFD simulations

4.3.2 Mesh generation strategy

The computational mesh was generated in ANSYS Meshing after the definition of the external fluid domain and of the main boundary zones. The aim was to obtain a discretization capable of resolving the main aerodynamic features of the semi-wing equipped with AMT, while keeping the total number of elements compatible with the limitations of the student version of ANSYS Fluent, which is about one million. For this reason, the mesh was not generated with a uniform element size throughout the whole domain, but through a local refinement strategy concentrated in the regions where the strongest gradients of the flow variables were expected.

From a physical point of view, the most relevant mesh-sensitive regions are the leading edge, the wing tip, the AMT hinge area, and the wake. The leading edge controls the initial development of the separated/vortical flow at moderate and high incidence; the wing tip is responsible for the formation of the tip vortex, whose strength and trajectory are directly affected by the AMT deflection; the hinge region may introduce local changes in pressure distribution, further development of vortices and in some cases blowing; finally, the wake region influences the prediction of drag and of the global momentum balance around the semi-wing.

The adopted mesh is an unstructured three-dimensional grid with local refinements around the wing, the AMT and the wake development region. An unstructured approach is suitable for the present geometry because the AMT introduces a geometric discontinuity at the junction between the fixed wing and the movable tip, and the highly swept planform makes a fully structured mesh more difficult to generate without a significant increase in manual preprocessing. The unstructured topology also allows the cell size to be varied locally, so that the near-body region can be refined while keeping a coarser discretization in the far-field part of the domain.

A first level of refinement was introduced around the entire wing through an influence body, used to increase the mesh density in the near field, where the pressure distribution, the development of the boundary layer, and the three-dimensional flow structures generated by the wing are concentrated, in the portion of the flow field that has the greatest impact on the calculated aerodynamic loads. Additional local refinements were applied along the leading edge and the trailing edge of the wing.

Particular attention was also paid to the AMT region: the mesh was locally refined near the hinge line, over the AMT surface and in the volume immediately downstream of the wing tip.

To account for the viscous effects close to the solid surfaces and to improve the resolution of the boundary layer, an *inflation layer* was generated on the wing and AMT walls. The inflation layer has a total thickness of 10 mm and was divided into seven layers. This choice represents a compromise between the need to describe the near-wall gradients and the need to keep the total number of elements below the maximum allowed by the available Fluent license.

Table 4.3: Main mesh-generation settings adopted for the CFD simulations.

Mesh feature	**Adopted strategy**
Mesh type	Three-dimensional unstructured mesh.
Near-wing refinement	Body of influence around the semi-wing and AMT.
Leading-edge refinement	Reduced element size to capture suction peak, flow acceleration and possible separation.
Trailing-edge refinement	Reduced element size to improve wake resolution.
AMT-region refinement	Local refinement near the movable tip, hinge region and downstream tip-vortex zone.
Wall treatment	Inflation layer on wing and AMT walls.
Inflation thickness	10 mm.
Number of inflation layers	7.
Mesh-size constraint	Total element number kept below the ANSYS Fluent Student limit.

The mesh density was gradually reduced when moving away from the wing towards the far-field boundaries. The far-field region does not require the same level of refinement as the near-wall region because the flow is expected to remain close to the imposed free-stream condition. Conversely, the downstream wake region was kept more refined than the outer far field because the wing and the AMT generate vortical structures that are convected downstream and may influence the resulting drag and moment coefficients.

A view of the generated mesh is reported in Figure 4.6 and 4.6, which highlights the refinement around the semi-wing, the local discretization of the AMT region and the inflation layers applied on the solid surfaces.

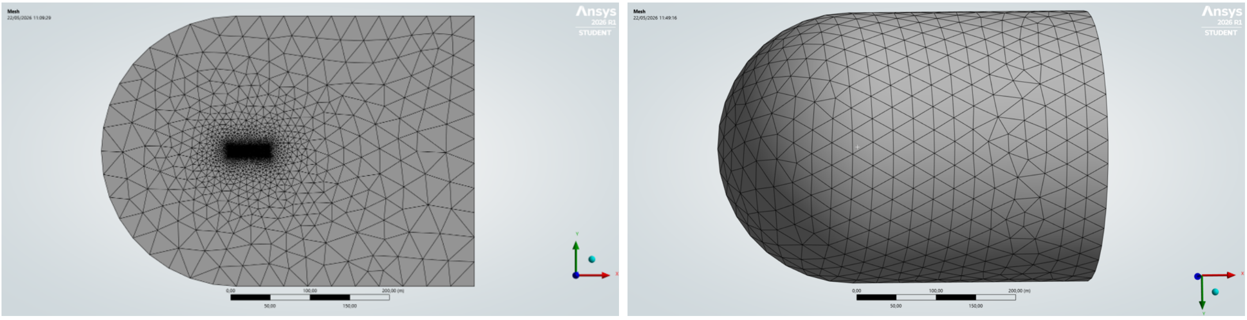

Figure 4.5: Mesh generated for the CFD simulations of the semi-wing equipped with AMT.

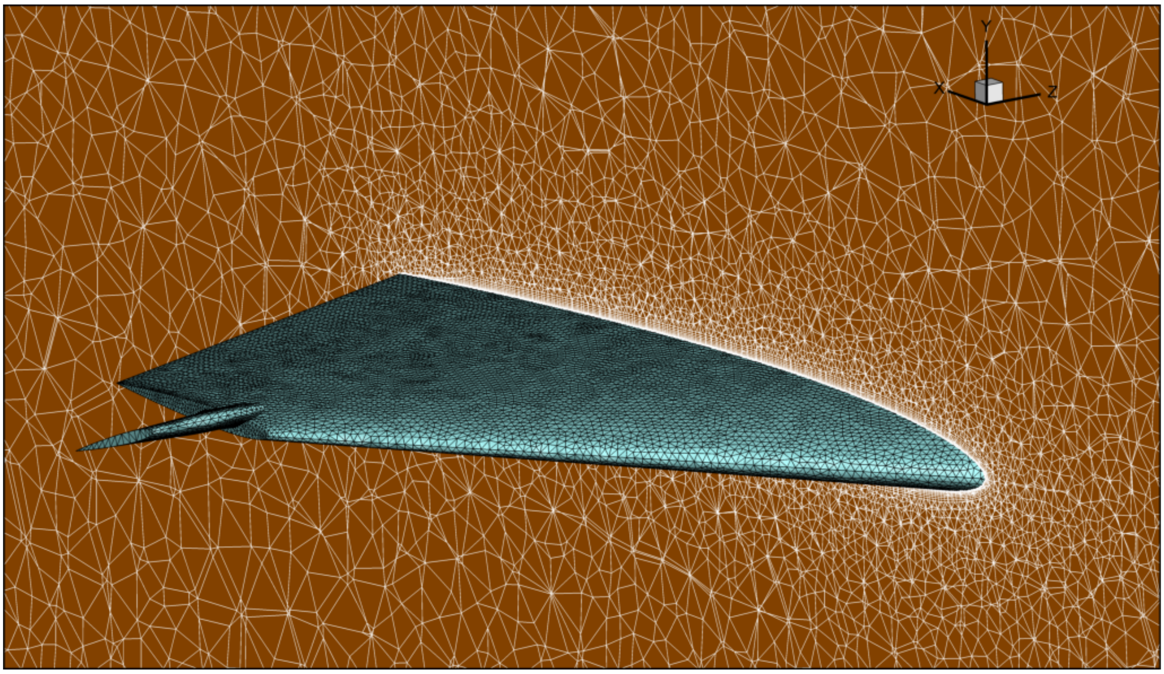

Figure 4.6: Mesh generated for the CFD simulations on the semi-wing and AMT surfaces.

The present mesh strategy was primarily constrained by the maximum number of cells available in the student version of ANSYS Fluent. So, the simulations must be interpreted as a preliminary numerical assessment of the AMT aerodynamic effect rather than as an high-fidelity CFD campaign. A complete verification of the numerical discretization would require a dedicated grid-independence study, based on progressively refined meshes and on the comparison of the resulting aerodynamic coefficients. Nevertheless, the adopted mesh provides a consistent basis for the parametric comparison among different AMT deflections, since the same meshing strategy was used for all the simulated configurations.

After mesh generation, the grid quality was checked before starting the CFD calculations. In particular, the mesh was inspected in terms of element distribution, local refinement around the wing and AMT, continuity of the inflation layers and absence of highly distorted cells in the near-wall region.

4.3.3 Boundary conditions

The adopted boundary conditions are summarized in Table 4.4.

Table 4.4: Boundary conditions adopted for the CFD simulations.

Boundary zone	Boundary condition	Physical meaning
Inlet / upstream far field	Pressure far-field	Imposition of the undisturbed free-stream conditions upstream of the wing.
Far-side external surface	Pressure far-field	Representation of the far-field region sufficiently far from the aerodynamic disturbance generated by the wing.
Outlet	Pressure outlet	Downstream boundary through which the wake and vortical structures leave the computational domain.
Root plane	Symmetry	Symmetry plane corresponding to the semi-wing root section.
Fixed wing surface	Wall	Solid viscous wall with no-slip condition.
AMT surface	Wall	Solid viscous wall corresponding to the deflected all-moving tip.

The inlet and far-field boundaries allow the free-stream Mach number, static pressure, static temperature and flow direction to be prescribed at a boundary located far from the body. According to the selected test condition, the Mach number was fixed at 0.3, while the pressure and temperature were set equal to the standard sea-level values: $p_{amb} = 101325$ Pa and $T_{amb} = 300$ K. The air was modelled as an ideal gas, so that the density was evaluated consistently from the imposed thermodynamic state. The free-stream thermodynamic conditions were kept constant for all the cases.

The angle of attack was introduced by prescribing the direction of the incoming flow at the pressure far-field boundaries: each value of α is obtained by rotating the incoming flow direction with respect to the fixed semi-wing. Since the simulations were carried out at zero sideslip angle, the free-stream velocity vector lies in the longitudinal plane of the semi-wing and no spanwise component of the incoming velocity is imposed.

In general form, the free-stream velocity components can be expressed as

$$V_x = V_\infty \cos\alpha, \qquad V_y = V_\infty \sin\alpha, \qquad V_z = 0, \tag{4.1}$$

where V_∞ is the free-stream velocity, which was defined from the prescribed Mach number through $V_\infty = M_\infty a_\infty$, and the speed of sound is given by $a_\infty = \sqrt{\gamma R T_\infty}$. Assuming standard sea-level temperature and air properties, the resulting velocity for $M_\infty = 0.3$ is approximately 102 m/s. This value is used by Fluent as the reference free-stream velocity for the computation of the aerodynamic coefficients.

The downstream boundary of the domain was defined as a pressure outlet, that imposes the static pressure at the outlet and allows the flow variables to adjust according to the solution inside the domain.

The root plane of the semi-wing was modelled as a symmetry plane, that imposes zero normal velocity and zero normal gradients of the flow variables across the plane, thereby reproducing the behaviour of a mirrored configuration without explicitly modelling the opposite half-wing. This choice reduces the number of computational cells and is consistent with the purpose of the present study, but also implies that the simulations do not faithfully reproduce the complete asymmetric flow field of a full wing with differential left-right AMT deflections.

The fixed wing surface and the AMT surface were both treated as stationary solid walls. This corresponds to imposing the no-slip condition at the wall, essential to capture the development of the boundary layer over the wing and over the AMT. Namely

$$\mathbf{u}_{\text{wall}} = \mathbf{0}, \tag{4.2}$$

where $\mathbf{u}_{\text{wall}}$ is the fluid velocity at the solid surface.

The same boundary condition strategy was adopted for all the simulated cases in the test matrix. Therefore, the only parameters varied from one simulation to another were the angle of attack α and the AMT deflection angle δ_{AMT}, while the external thermodynamic conditions, the far-field pressure and temperature, the sideslip angle and the type of boundary conditions were kept unchanged.

4.3.4 Solver settings and turbulence modelling

The CFD simulations were performed in ANSYS Fluent by solving the Reynolds-Averaged Navier–Stokes (RANS) equations for a viscous turbulent flow around the semi-wing equipped with AMT. Since the objective of the analysis is a comparison among several steady configurations, the simulations were treated as steady-state calculations, with the AMT fixed at a prescribed deflection angle for each case.

Note that the use of a steady RANS approach introduces some limitations. The flow over an highly swept and low aspect-ratio wing at moderate and high angles of attack may contain unsteady separated structures, vortex wandering or vortex breakdown phenomena. A steady RANS simulation cannot fully resolve these time-dependent features, because the turbulent and unsteady components of the flow are modelled rather than directly computed. Therefore, the results obtained in this work should be interpreted primarily in terms of mean aerodynamic loads and qualitative flow-field trends. A more detailed investigation of unsteady vortex dynamics would require higher-fidelity approaches, such as unsteady RANS, Detached Eddy Simulation or Large Eddy Simulation, together with a significantly higher computational cost.

The governing equations solved by the CFD solver include conservation of mass, momentum and energy. The energy equation was activated in order to account for the coupling between velocity, pressure, density and temperature, consistent with the use of a compressible ideal-gas formulation. The air was modelled as an ideal gas, so that the density is not imposed as a constant value but is computed from the local pressure and temperature according to

$$\rho = \frac{p}{RT}, \tag{4.3}$$

where p is the static pressure, T is the static temperature and R is the specific gas constant for air.

Within the RANS framework, the instantaneous flow quantities are decomposed into mean and fluctuating components. The solver computes the mean flow field, while the effect of turbulence fluctuations is introduced through a turbulence closure model.

Turbulence is modelled using the Shear Stress Transport k-ω model. The SST k-ω model solves two additional transport equations: one for the turbulent kinetic energy k (representing the intensity of velocity fluctuations) and one for the specific dissipation rate ω (related to the rate at which turbulent energy is dissipated). The resulting turbulent viscosity is then used to close the Reynolds stresses appearing in the averaged momentum equations.

The SST formulation combines the advantages of the k-ω model in the inner part of the boundary layer with the more robust free-stream behaviour of a k-ε-type formulation away from the wall, making the model particularly appropriate for external aerodynamic flows in which both near wall resolution and pressure gradient behaviour, possible flow separation and three dimensional vortical structures are involved.

The pressure–velocity coupling was handled through the algorithms available in the pressure-based formulation of Fluent. For steady-state RANS calculations, this coupling is required to ensure that the velocity field satisfies mass conservation while the pressure field is updated consistently with the momentum equations. Spatial discretization schemes were chosen in order to obtain a stable and sufficiently accurate solution for all the cases in the simulation matrix. The same numerical settings were maintained throughout the parametric campaign.

The main solver settings adopted in the numerical campaign are summarized in Table 4.5.

Table 4.5: Main solver settings adopted for the CFD simulations.

Setting	**Adopted option**
CFD solver	ANSYS Fluent.
Flow formulation	Steady-state RANS.
Solver type	Pressure-based solver.
Energy equation	Enabled.
Fluid model	Air modelled as ideal gas.
Turbulence model	SST k-ω.
Varied parameters	Angle of attack α and AMT deflection angle δ_{AMT}.
Fixed parameters	Mach number, reference geometry, thermodynamic free-stream conditions and numerical setup.

4.3.5 Reference quantities and aerodynamic coefficients

The aerodynamic forces and moments obtained from the CFD simulations are expressed in non-dimensional form by using a fixed set of reference quantities. The dynamic pressure is defined as

$$q_\infty = \frac{1}{2}\rho_\infty V_\infty^2, \tag{4.4}$$

where ρ_∞ and V_∞ are respectively the free-stream density and velocity. The force coefficients are then defined as

$$C_L = \frac{L}{q_\infty S_{\text{ref}}}, \qquad C_D = \frac{D}{q_\infty S_{\text{ref}}}, \tag{4.5}$$

where L and D are the lift and drag forces referred to the adopted aerodynamic reference frame.

The rolling, pitching and yawing moment coefficients are expressed as

$$C_l = \frac{l}{q_\infty S_{\text{ref}} b}\ , \qquad C_m = \frac{m}{q_\infty S_{\text{ref}} \bar{c}}\ , \qquad C_n = \frac{n}{q_\infty S_{\text{ref}} b}\ , \tag{4.6}$$

where l, m and n are the rolling, pitching and yawing moments, while b and c are respectively the reference span and the reference chord used in the CFD solver.

The moments are defined with respect to the center of gravity (CG) of the wing, calculated from the CAD model of assuming that the entire wing is filled with material of constant density. Its coordinates in the Fluent reference frame are $X_{CG} = 8.6\ m$, $Y_{CG} = 0\ m$, $Z_{CG} = 0\ m$ for all the simulated cases.

The hinge moment coefficient of the AMT is also considered because it provides an estimate of the aerodynamic moment that the actuation system must overcome in order to hold the AMT at a prescribed deflection. The hinge moment coefficient can be written as

$$C_h = \frac{M_h}{q_\infty S_{\text{AMT}} \bar{c}_{\text{AMT}}}, \tag{4.7}$$

where M_h is the aerodynamic moment about the AMT hinge axis, S_{AMT} is the AMT planform area and $\bar{c}_{\text{AMT}}$ is the mean aerodynamic chord of the movable surface.

4.3.6 Convergence assessment and post-processing procedure

For each simulated configuration, the solution process was monitored in order to assess whether a sufficiently stable aerodynamic state had been reached before extracting the final force and moment coefficients. In steady RANS simulations, convergence cannot be evaluated only by looking at the residuals of the governing equations, especially when the flow field contains separated regions, vortical structures or mild oscillations in the aerodynamic loads,whose convergence may be slower than that of the global residuals. So the convergence assessment was based on a combined evaluation of the histories of scaled residuals of the continuity, momentum, energy and turbulence-model equations and on of the aerodynamic coefficient histories, monitored as functions of the iteration number.

The stabilization of these coefficients was considered an essential requirement for the extraction of the final aerodynamic data. In practice, a simulation was considered acceptable when the residuals had decreased by a sufficient amount and the monitored coefficients exhibited small oscillations around an approximately constant mean value.

Each case was advanced for a fixed number of iterations (approximately 1200), and the final aerodynamic coefficients were obtained by averaging the stabilized portion of the coefficient histories, canceling the influence of the initial transient part of the solution.

For a generic aerodynamic coefficient C_i, where

$$C_i = C_L, C_D, C_l, C_m, C_n, C_h, \tag{4.8}$$

the averaged value used for the post-processing was computed as

$$\overline{C_i} = \frac{1}{N} \sum_{k=N_{\text{start}}}^{N_{\text{end}}} C_i^{(k)}, \tag{4.9}$$

where $C_i^{(k)}$ is the value of the coefficient at iteration k, N_{end} is the final iteration, N_{start} is the first iteration included in the averaging interval and N is the number of samples used to compute the mean value.

The aerodynamic coefficients extracted from Fluent were then organized according to the simulation matrix, with each case identified by the corresponding angle of attack α and AMT deflection angle δ_{AMT}.

For each angle of attack, the aerodynamic effect of the AMT is evaluated by comparing the deflected configuration with the corresponding baseline case at $\delta_{\text{AMT}} = 0°$ (clean configuration). The incremental coefficient associated with the AMT deflection is therefore defined as

$$\Delta C_i(\alpha, \delta_{\text{AMT}}) = C_i(\alpha, \delta_{\text{AMT}}) - C_i(\alpha, 0), \qquad i = L, D, l, m, n, h. \tag{4.10}$$

This definition makes it possible to distinguish the aerodynamic behaviour of the clean semi-wing from the additional contribution generated by the movable tip, and it also provides a direct way to compare the control effectiveness of different AMT deflections.

In addition to the integral coefficients, selected flow field quantities were post-processed in order to interpret the physical mechanisms responsible for the observed aerodynamic trends. Pressure contours were used to analyse the modification of the surface loading caused by the AMT deflection. Velocity fields were examined to identify acceleration regions, separated zones and wake development. Vorticity contours were used to visualize the tip vortex and the vortical structures generated or modified by the deflected AMT.

All the post-processing operations were performed using a consistent set of reference quantities for all the simulated cases. The reference area, reference chord, reference span, moment reference point and free-stream quantities were kept fixed within each condition, so that the resulting coefficients could be compared directly across different values of α and δ_{AMT}.

4.4 Simulation matrix

The CFD campaign was organized through a simulation matrix in order to evaluate the aerodynamic effect of the All-Moving Tip (AMT) over a prescribed range of angles of attack and control-surface deflections. The objectives were:

- to allow the aerodynamic behaviour of the baseline semi-wing to be characterized as the incidence angle increases.
- to make it possible to quantify the incremental contribution of the AMT by comparing each deflected configuration with the corresponding undeflected case at the same flight condition.

The independent parameters selected for the numerical campaign are the angle of attack α and the AMT deflection angle δ_{AMT}, while the free-stream Mach number was kept fixed at

$$M_\infty = 0.3, \tag{4.11}$$

which corresponds to a subsonic condition in which compressibility effects are limited, thus providing a suitable reference condition for the preliminary aerodynamic assessment of the AMT concept.

The sideslip angle was kept equal to zero in all the simulations, so that the analysis is focused on the effect of incidence and AMT deflection without introducing an additional lateral flow component. The reference geometry, computational domain, boundary condition strategy, mesh generation approach and solver settings were kept unchanged throughout the whole simulation matrix. Therefore, the differences observed in the aerodynamic coefficients can be directly attributed to the variation of α and δ_{AMT}.

The angle of attack range was selected to cover both low incidence and high incidence conditions, with a thickening approaching the stall incidence (maximum lift condition). Low values of α are useful to assess the nearly linear aerodynamic response of the semi-wing and the initial control effectiveness of the AMT. Conversely, moderate and high values of α are required to investigate the nonlinear post-stall behaviour. For this reason, the incidence sweep includes closely spaced values in the intermediate range, where changes in the aerodynamic trends may occur.

The AMT deflection range was chosen in order to evaluate both the baseline configuration and several deflected configurations. The undeflected case, $\delta_{\text{AMT}} = 0°$, is used as reference condition for the computation of the incremental aerodynamic coefficients. Positive and negative AMT deflections are then considered to assess the sensitivity of the aerodynamic loads and moments to the rotation of the movable tip.

The complete set of independent parameters adopted in the simulation matrix is summarized in Table 4.6.

Table 4.6: Independent parameters adopted in the CFD simulation matrix.

Parameter	**Symbol**	**Values**
AMT deflection angle	δ_{AMT}	$-30°,\ -20°,\ -10°,\ -5°,\ 0°,\ 5°,\ 10°,\ 20°,\ 30°,\ 40°,\ 50°,\ 60°$
Angle of attack	α	$0°,\ 5°,\ 10°,\ 15°,\ 20°,\ 22.5°,\ 24°,\ 30°,\ 35°,\ 40°,\ 45°$

The matrix is obtained by combining every angle of attack with every AMT deflection angle. Therefore, the total number of simulations is

$$N_{\text{cases}} = N_\alpha \times N_\delta = 11 \times 12 = 132, \tag{4.12}$$

where $N_\alpha = 11$ is the number of incidence angles and $N_\delta = 12$ is the number of AMT deflections.

The simulation matrix was designed as a compromise between aerodynamic completeness and computational cost and time. A denser sampling of α and δ_{AMT} would provide a more detailed description of the aerodynamic database, but it would also require a significantly larger number of CFD simulations. The adopted set of cases was therefore selected to capture the main aerodynamic trends while remaining compatible with the available computational resources and with the preliminary nature of the present investigation.

4.5 Results

4.5.1 Aerodynamic coefficients as a function of angle of attack

The following section presents the main aerodynamic coefficients obtained from the CFD campaign as a function of the angle of attack. The analysis is carried out for different AMT deflection angles in order to evaluate both the global aerodynamic behaviour of the wing half-model and the influence of the all-moving tip on the resulting aerodynamic forces and moments.

The results are first discussed in terms of lift and drag coefficients, which describe the overall force response of the configuration. The drag polar is then introduced to assess the aerodynamic efficiency of the wing. Finally, the rolling, pitching and yawing moment coefficients are analysed in order to evaluate the control authority provided by the AMT.

Lift coefficient

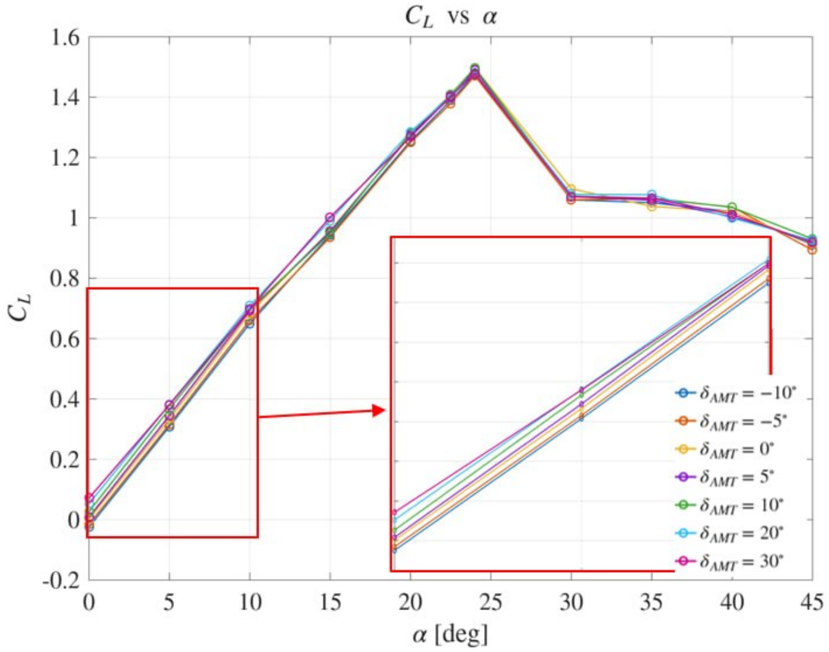

Figure 4.7: Lift coefficient as a function of the angle of attack for different AMT deflection angles.

Figure 4.7 shows the variation of the lift coefficient C_L as a function of the angle of attack α for the different AMT deflection angles considered in the CFD campaign.

For all the analysed AMT deflections, the lift coefficient exhibits an almost linear increase at low and moderate angles of attack. This behaviour is observed up to approximately $\alpha = 24°$, where the maximum lift condition is reached. The corresponding value of C_L is close to 1.5, indicating that the highly swept configuration is able to sustain a significant lift level before the occurrence of the main lift breakdown.

Beyond this incidence, a clear reduction in C_L is observed. This lift drop indicates the onset of stall, associated with the progressive deterioration of the organized vortical flow over the upper surface. Nevertheless, the stall behaviour is not abrupt. After the initial lift decrease, the configuration maintains a relatively high residual lift level over the post-stall range. In particular, between approximately $\alpha = 30°$ and $\alpha = 40°$, the lift coefficient remains almost constant, before decreasing further at the highest angle of attack considered.

This soft-stall behaviour is mainly related to the vortex-dominated aerodynamics of the highly swept wing. The leading-edge vortex provides an additional suction contribution on the upper surface and represents one of the main lift-generating mechanisms of the configuration. As a consequence, even after the onset of extensive flow separation and vortex degradation, the complete loss of lift is delayed and the wing preserves a significant post-stall lift capability.

The effect of the AMT deflection on the global lift coefficient is highlighted by the magnified views included in Figure 4.7. Since the AMT involves only a limited portion of the semi-wing planform, its influence on the total lift coefficient is relatively small. However, a systematic and appreciable effect can still be observed. As the AMT deflection increases, the lift coefficient tends to increase over the analysed range of angles of attack. This trend can be interpreted as a consequence of the local increase in effective incidence at the movable wing tip, which produces a local lift increment on the outboard portion of the wing.

Therefore, although the AMT does not significantly modify the overall lift curve of the configuration, it introduces a measurable lift contribution. This result confirms that the movable tip affects the local aerodynamic loading while preserving the global vortex-dominated lift behaviour of the baseline highly swept wing.

Drag coefficient

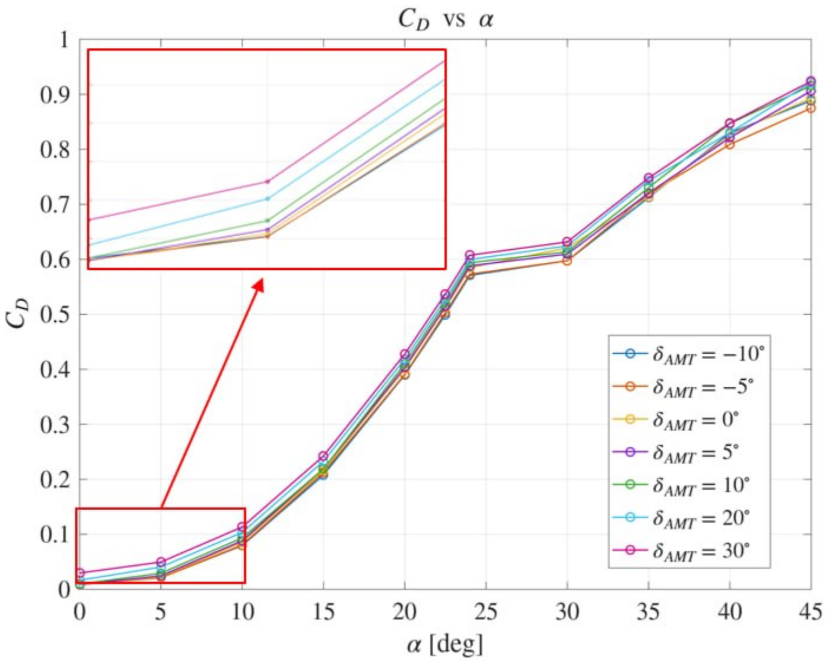

Figure 4.8: Drag coefficient as a function of the angle of attack for different AMT deflection angles.

Figure 4.8 shows the variation of the drag coefficient C_D as a function of the angle of attack α for the different AMT deflection angles considered in the CFD campaign.

The drag coefficient increases over the whole range of incidence, due to the progressive growth of pressure drag and separated-flow regions, although the slope of the curve changes significantly as the angle of attack increases. At low and moderate angles of attack, C_D exhibits a smooth and approximately quadratic growth. This trend is consistent with the increase of lift-induced drag component, which scales approximately with C_L^2, with the lift coefficient increases almost linearly with α.

A change in the behaviour of the curve is observed around the stall region, consistently with the lift-coefficient trend discussed previously. Once the maximum-lift condition is reached and the organized vortical structure starts to degrade, the lift coefficient no longer increases with the same slope. As a consequence, the lift-dependent part of the drag tends to saturate. At the same time, the separated-flow regions continue to expand over the upper surface, increasing the pressure-drag contribution. The balance between these two opposite effects explains the presence of a plateau, or of a less pronounced drag increase, in the post-stall range.

The effect of the AMT deflection on the drag coefficient is highlighted by the magnified view included in Figure 4.8. Since the AMT affects only a limited portion of the semi-wing planform, its influence on the global drag coefficient is relatively small. Nevertheless, a systematic effect can be observed. As the AMT deflection increases, the drag coefficient tends to increase. This is caused by the local increase in effective incidence at the movable wing tip, which generates a higher local aerodynamic loading and, consequently, a larger local contribution to pressure drag and induced drag.

Therefore, the AMT does not substantially alter the global drag build-up of the configuration, which remains governed by the highly swept wing and by its vortex-dominated high-angle-of-attack aerodynamics. However, it introduces a measurable drag penalty associated with the local modification of the flow field near the tip. This penalty is limited in magnitude, but it must be considered when assessing the overall effectiveness of the AMT, since the same deflection that produces useful control moments can also increase the aerodynamic resistance of the configuration.

Drag polar

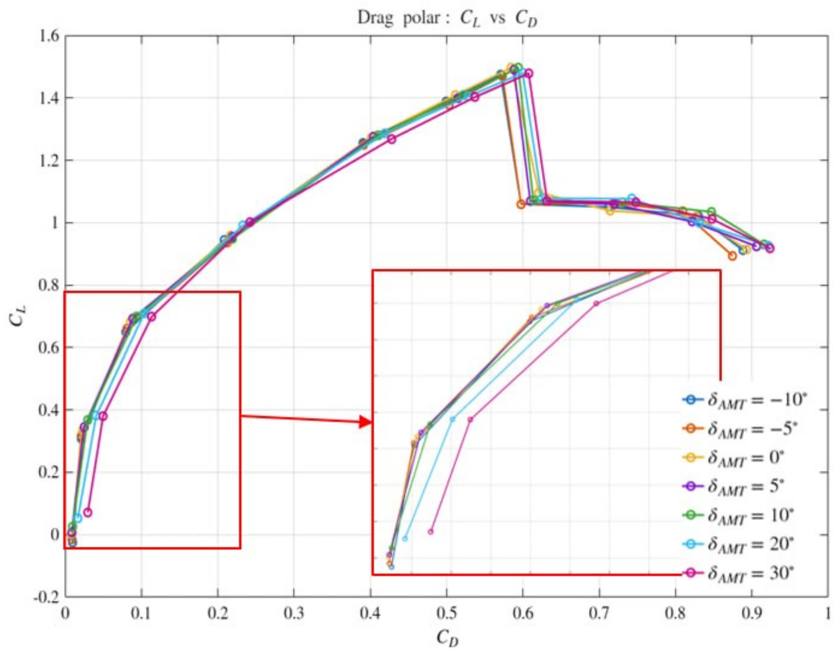

Figure 4.9: Drag polar of the wing half-model for different AMT deflection angles.

Figure 4.9 shows the drag polar of the configuration, obtained by plotting the drag coefficient C_D as a function of the lift coefficient C_L for the different AMT deflection angles considered in the CFD campaign.

This representation allows the aerodynamic efficiency of the wing half-model to be assessed over the investigated range of incidence angles, making it possible to identify the operating regions in which the configuration produces lift more efficiently and those in which the drag rise becomes more significant.

At low and moderate lift coefficients, the drag polar exhibits the expected smooth increase of C_D with C_L. In this range, the flow is still mainly governed by an organized aerodynamic loading, and the drag growth is consistent with the classical lift-dependent contribution to drag. Since the induced-drag component scales approximately with C_L^2, the initial part of the polar assumes an approximately parabolic shape. This region corresponds to the pre-stall range of the lift curve, where an increase in angle of attack produces a simultaneous increase in lift and drag. The drag polar confirms that the most efficient operating region of the configuration is located before the onset of stall, where lift increases with a relatively moderate drag penalty

As the maximum-lift condition is approached, the polar departs from this simple parabolic behaviour. This is a direct consequence of the vortex-dominated aerodynamics of the highly swept wing: the leading-edge vortex provides an important suction contribution on the upper surface, increasing the lift but also introducing an additional pressure-drag contribution. In the post-stall region, the drag polar shows a less efficient behaviour. After the maximum value of C_L is reached, the lift coefficient no longer increases and even decreases, while the drag coefficient remains high and continues to increase. This produces a partially folded portion of the polar. Physically, this behaviour is associated with the degradation and breakdown of the leading-edge vortex and with the growth of separated-flow regions over the upper surface.

The magnified view included in Figure 4.9 highlights the effect of the AMT deflection on the drag polar. Since the AMT affects only a limited portion of the semi-wing planform, the displacement of the polar is relatively small. However, the effect is systematic and appreciable. As the AMT deflection increases, both the local effective incidence and the local aerodynamic loading at the movable tip increase. This produces a local lift increment, but also a local drag increment, associated with higher pressure drag and lift-dependent drag at the tip.

Globally, as the deflection increases, the efficiency drops slightly. The AMT-deflected configurations tend to move slightly towards higher values of C_D for comparable values of C_L. This indicates that the AMT introduces a limited but measurable aerodynamic penalty. The penalty is small because the moving surface occupies only a reduced fraction of the semi-wing, but it is relevant when assessing the overall effectiveness of the device. The AMT is therefore not intended to improve the aerodynamic efficiency of the wing; rather, it modifies the local loading near the tip in order to generate control moments, with a modest associated drag cost.

Rolling moment coefficient

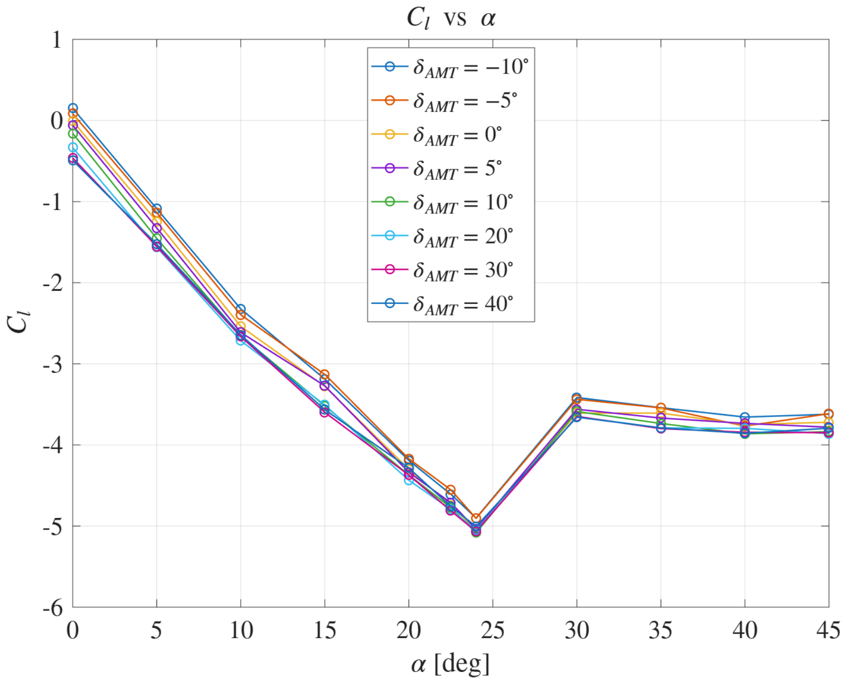

Figure 4.10: Rolling moment coefficient as a function of the angle of attack for different AMT deflection angles.

Figure 4.10 shows the variation of the rolling moment coefficient C_l as a function of the angle of attack α for the different AMT deflection angles considered in the CFD campaign.

Before analysing the effect of the AMT deflection, it is important to recall that the CFD model corresponds to a single semi-wing, while the aerodynamic moments are evaluated with respect to the reference point of the complete wing configuration. As a consequence, even the undeflected case, $\delta_{\text{AMT}} = 0°$, produces a non-zero rolling moment coefficient. This does not represent a roll imbalance of the complete aircraft, but is a direct consequence of the half-model approach. In a complete symmetric wing, under zero sideslip and with symmetric AMT deflection, the rolling moment generated by one semi-wing would be balanced by the opposite contribution generated by the other semi-wing. In the present half-model, instead, the aerodynamic load acts on only one side of the reference plane and therefore produces a rolling moment due to its lateral lever arm with respect to the longitudinal axis.

In first approximation, the rolling moment generated by the semi-wing can be interpreted as the spanwise moment of the vertical aerodynamic load distribution:

$$L_x \simeq \int y \, dF_z,$$

where y is the local spanwise distance from the reference plane and dF_z is the local vertical aerodynamic force. Therefore, the rolling moment coefficient is strongly linked to the lift generated by the semi-wing and to the spanwise location of the corresponding aerodynamic loading. For this reason, the overall trend of C_l closely follows the trend previously observed for the lift coefficient C_L.

The effect of the AMT deflection is visible but limited in magnitude. Nevertheless, the effect is systematic. As the AMT deflection increases, the local effective incidence of the movable tip increases, generating a local increment of aerodynamic loading near the wing tip. Since this load acts at a large spanwise distance from the reference axis, even a relatively small force increment at the tip can produce a measurable variation of the rolling moment.

With the present sign convention, positive AMT deflections generally make C_l more negative, whereas negative AMT deflections tend to reduce its absolute value. This confirms that the AMT is able to modify the spanwise load distribution and therefore to generate a rolling-moment increment. However, the curves remain close to each other when plotted as absolute C_l values as a function of α, because the dominant contribution is still the baseline lift of the semi-wing. For this reason, the present figure is mainly useful to describe the global rolling-moment behaviour, while the actual roll control authority of the AMT is more clearly assessed through the incremental rolling moment coefficient, obtained by subtracting the corresponding undeflected case, as will be done later.

Pitching moment coefficient

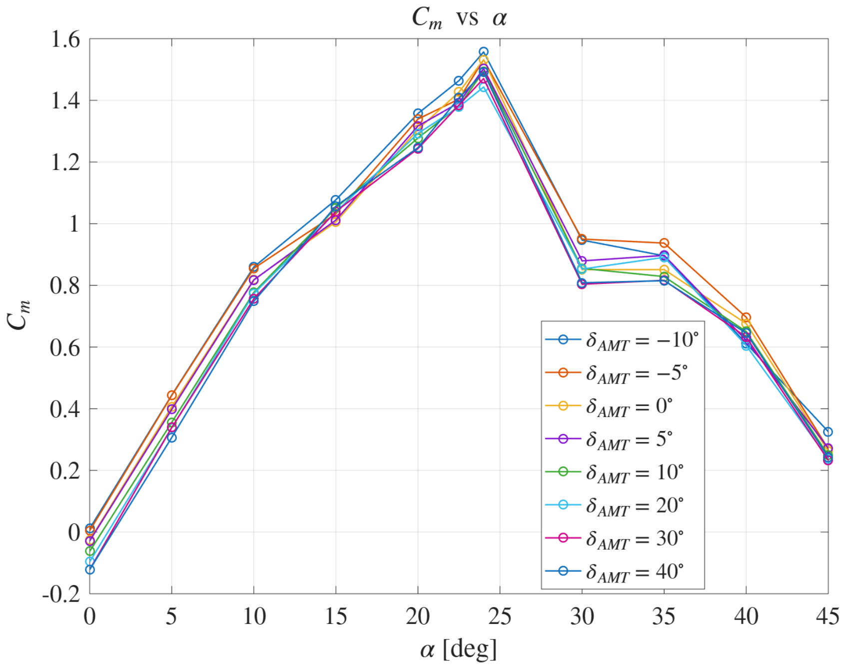

Figure 4.11: Pitching moment coefficient as a function of the angle of attack for different AMT deflection angles.

Figure 4.11 shows the variation of the pitching moment coefficient C_m as a function of the angle of attack α for the different AMT deflection angles considered in the CFD campaign.

The trend of the pitching moment coefficient is closely related to the evolution of the aerodynamic load distribution over the wing as the angle of attack increases. In fact, the pitching moment about the reference point depends not only on the magnitude of the resultant aerodynamic force, but also on its longitudinal position. In first approximation, the pitching moment can be interpreted as

$$M_y \sim L\,(x_{\text{ref}} - x_{\text{cp}})\,,$$

where x_{ref} is the longitudinal coordinate of the moment reference point and x_{cp} is the effective centre of pressure of the aerodynamic load. Therefore, variations of C_m with α reflect both the increase or decrease of lift and the forward or rearward displacement of the aerodynamic resultant.

At low and moderate angles of attack, the leading-edge vortex progressively strengthens and produces an increasing suction contribution on the upper surface of the highly swept wing. This modifies the pressure distribution and moves the effective aerodynamic resultant forward. As a consequence, the pitching moment coefficient varies systematically with α up to the maximum-lift condition. This behaviour is consistent with the pressure-field evolution later shown for the undeflected AMT configuration in Figures 4.13, 4.14, 4.15 and 4.16. In particular, as the incidence increases, the suction region associated with the leading-edge vortex becomes more intense and affects the longitudinal position of the resultant aerodynamic load.

At moderate incidences, the aerodynamic resultant tends to move forward as the vortical suction contribution becomes stronger. Beyond the maximum-lift condition, the organized vortical structure starts to degrade and vortex breakdown becomes more relevant. The suction distribution over the upper surface is consequently modified and the effective centre of pressure moves rearward. This rearward displacement explains the change in the pitching-moment trend observed after stall.

The influence of the AMT deflection on the pitching moment coefficient is limited but visible. This is expected, since the AMT affects only a relatively small portion of the semi-wing planform and is located mainly in the outboard region. Its deflection modifies the local aerodynamic loading at the wing tip, but the corresponding longitudinal lever arm with respect to the pitching-moment reference point is limited. As a result, the AMT does not strongly alter the global pitching-moment curve of the configuration.

Yawing moment coefficient

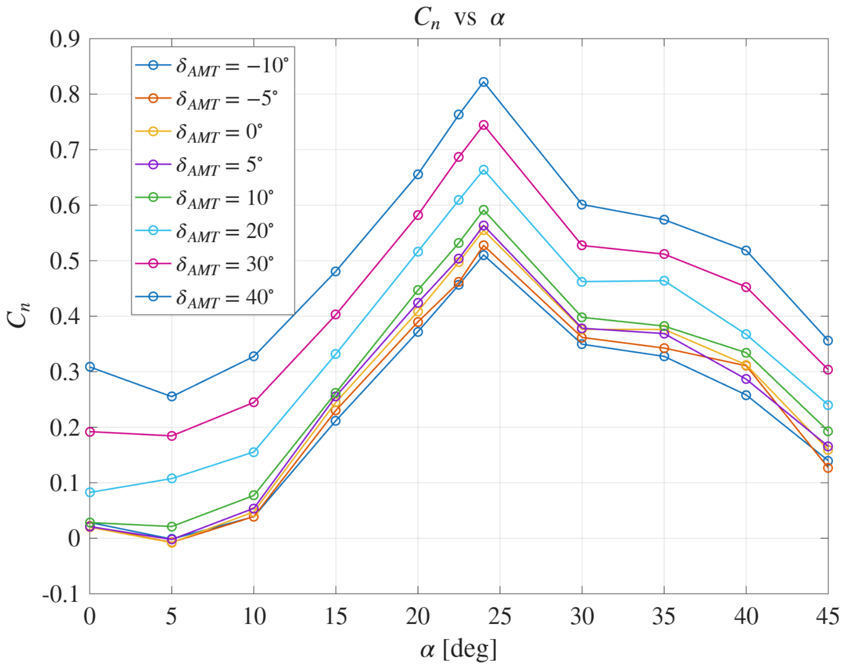

Figure 4.12: Yawing moment coefficient as a function of the angle of attack for different AMT deflection angles.

Figure 4.12 shows the variation of the yawing moment coefficient C_n as a function of the angle of attack α for the different AMT deflection angles considered in the CFD campaign.

As for the rolling moment, it should be recalled that the numerical model consists of a single semi-wing, while the moments are evaluated with respect to the reference point of the complete wing configuration. Therefore, also the undeflected case produces a non-zero yawing moment. This contribution does not represent an intrinsic yaw imbalance of the complete aircraft, but is a consequence of the half-model approach. In a complete symmetric configuration, under zero sideslip and symmetric flow conditions, the yawing moment generated by one semi-wing would be balanced by the opposite contribution of the other semi-wing.

In first approximation, the yawing moment about the vertical axis can be written as

$$N_z \simeq \int (x\, dF_y - y\, dF_x)\,,$$

where dF_x and dF_y are the local axial and side-force components, respectively. Since the present simulations are performed at zero sideslip, the yawing moment is mainly associated with the axial-force distribution acting at a finite spanwise distance from the reference axis. Thus, the aerodynamic force generated by the semi-wing produces a yawing moment simply because it acts on only one side of the aircraft reference plane.

The global trend of C_n is closely connected with the evolution of the aerodynamic loading over the wing. Although the yawing moment is more directly related to the axial-force and side-force distributions than to the lift itself, these quantities are strongly coupled in high angle of attack regimes. For this reason, the overall variation of C_n with α follows a trend similar to that observed for the lift coefficient.

Up to the maximum-lift region, the increase in aerodynamic loading produces a progressive increase in the magnitude of the yawing moment. After stall, the degradation of the organized vortical structure and the onset of vortex breakdown modify the pressure and drag distributions over the wing. Consequently, the yawing moment also changes its trend and tends to reach a post-stall level, consistently with the behaviour already observed for the lift and rolling moment coefficients.

Overall, Figure 4.12 shows that the AMT has a clear influence on the yawing moment of the configuration. The absolute values of C_n are affected by the half-wing modelling approach and therefore include the baseline yawing contribution of the isolated semi-wing. However, the systematic variation with AMT deflection confirms that the movable tip is able to modify the asymmetric drag and load distribution and can therefore provide a measurable yaw-control contribution. As for the other moment coefficients, the actual yaw-control authority of the AMT is more clearly assessed through the incremental yawing moment coefficient with respect to the undeflected case.

4.5.2 Pressure field

$\delta_{\mathbf{AMT}} = 0°$

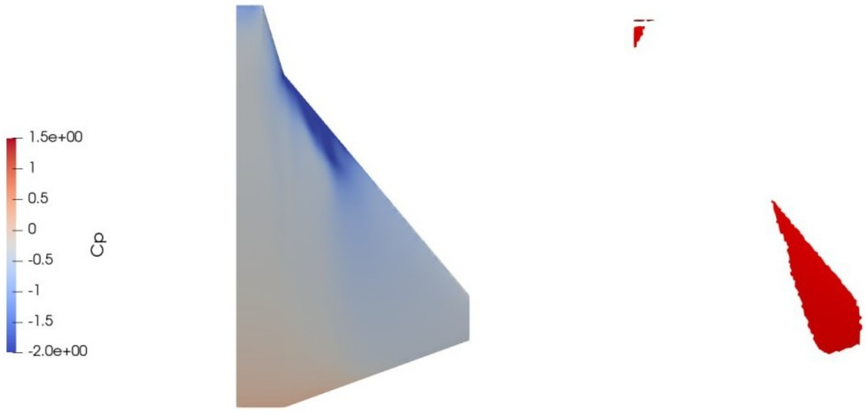

Figure 4.13: Pressure coefficient C_p field (left) and separated-flow regions identified by $\tau_x \leq 0$ (right) on the upper surface for $\delta_{\mathrm{AMT}} = 0°$ and $\alpha = 15°$.

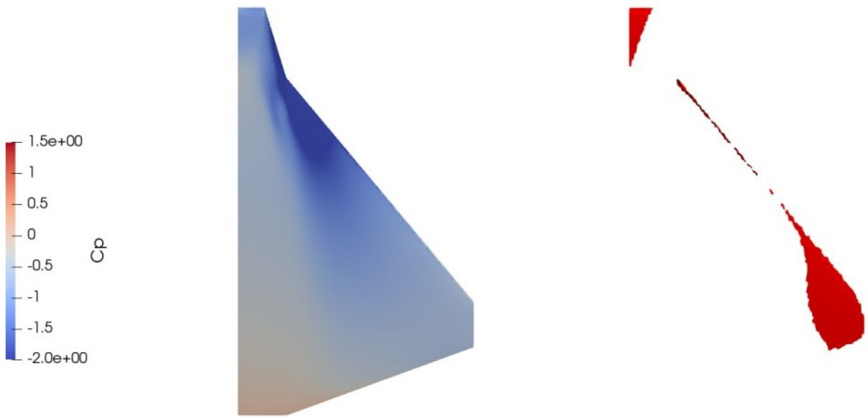

Figure 4.14: Pressure coefficient C_p field (left) and separated-flow regions identified by $\tau_x \leq 0$ (right) on the upper surface for $\delta_{\mathrm{AMT}} = 0°$ and $\alpha = 24°$.

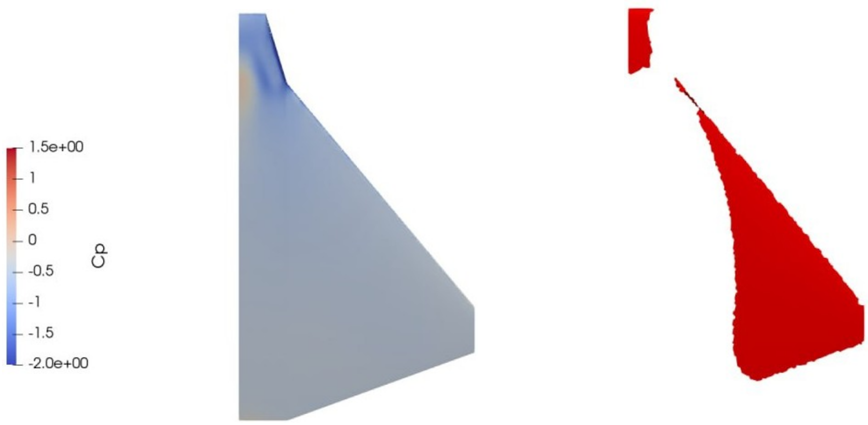

Figure 4.15: Pressure coefficient C_p field (left) and separated-flow regions identified by $\tau_x \leq 0$ (right) on the upper surface for $\delta_{\mathrm{AMT}} = 0°$ and $\alpha = 30°$.

Figure 4.16: Pressure coefficient C_p field (left) and separated-flow regions identified by $\tau_x \leq 0$ (right) on the upper surface for $\delta_{\mathrm{AMT}} = 0°$ and $\alpha = 45°$.

Figures 4.13–4.16 show the upper-surface pressure-coefficient distributions and the corresponding separated-flow regions for the undeflected configuration, $\delta_{\mathrm{AMT}} = 0°$, at four representative angles of attack: $\alpha = 15°$, $24°$, $30°$ and $45°$. The pressure field is used to identify the main suction regions on the wing, while the maps based on $\tau_x \leq 0$ provide an indication of the areas where the near-wall streamwise shear stress becomes negative, which is here used as a marker of local flow separation.

At moderate angles of attack, namely $\alpha = 15°$ and $\alpha = 24°$, the pressure distribution is still relatively organized. The most intense suction region, associated with the lowest values of C_p, is located close to the leading-edge region and extends over a significant portion of the upper surface. This behaviour is consistent with the vortex-dominated aerodynamics of a highly swept wing, where the leading-edge vortex generates a low-pressure region on the suction side and provides an important additional contribution to lift.

At $\alpha = 15°$, the separated-flow map shows that most of the inner and central part of the wing is still characterized by an attached or only mildly separated flow. However, the outboard region close to the tip already exhibits signs of separation. This suggests that, even before the maximum-lift condition is reached, the external part of the semi-wing is more prone to flow detachment, due to the combined effect of the local three-dimensional flow, the tip vortex and the reduced chord in the outer region.

At $\alpha = 24°$, which corresponds approximately to the maximum-lift condition observed in the global aerodynamic coefficients, the suction level over the upper surface is more pronounced. The leading-edge vortex appears to be highly effective in maintaining a strong low-pressure region over the wing. At the same time, the separated-flow region becomes more extended, especially toward the outboard portion of the semi-wing. This indicates that the configuration is operating close to the limit of the pre-stall regime: the vortex still provides a significant lift contribution, but the separated region is already growing.

When the angle of attack is increased to $\alpha = 30°$, the pressure field becomes less regular and the separated-flow region spreads over a larger portion of the upper surface. The suction peak associated with the leading-edge vortex is still present, but it is weakened and redistributed. This condition is representative of the early post-stall regime: the flow is no longer predominantly attached, but the vortex system still allows the wing to retain a relatively high residual lift level.

At the highest investigated incidence, $\alpha = 45°$, the separated-flow region covers most of the upper surface. The pressure distribution is therefore dominated by a large-scale separated flow, and the suction pattern becomes significantly less coherent than at lower angles of attack. In this condition, the leading-edge vortex is no longer able to maintain the same level of organized suction over the wing, and the aerodynamic loading is strongly affected by the extensive separation.

Overall, the clean configuration shows a progressive transition from a vortex-dominated pre-stall behaviour to a largely separated post-stall regime. At intermediate incidence, the leading-edge vortex produces a strong suction region and supports lift generation, whereas the outboard part of the wing is the first region to exhibit separation. As the angle of attack increases, the separated area propagates inboard and covers most of the upper surface, explaining the reduction in lift observed beyond the maximum-lift condition.

4.5.3 Spanwise distribution of the lift coefficient

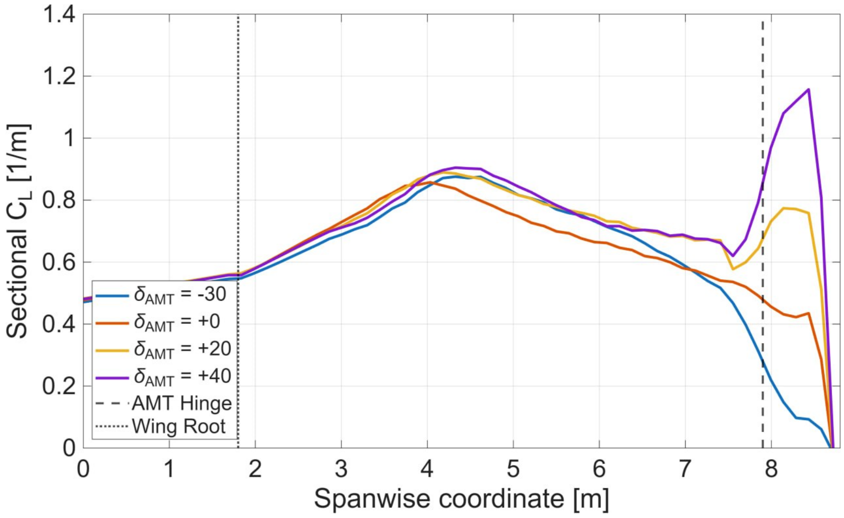

Figure 4.17: Spanwise distribution of the sectional lift coefficient for different AMT deflection angles, at $\alpha = 15°$.

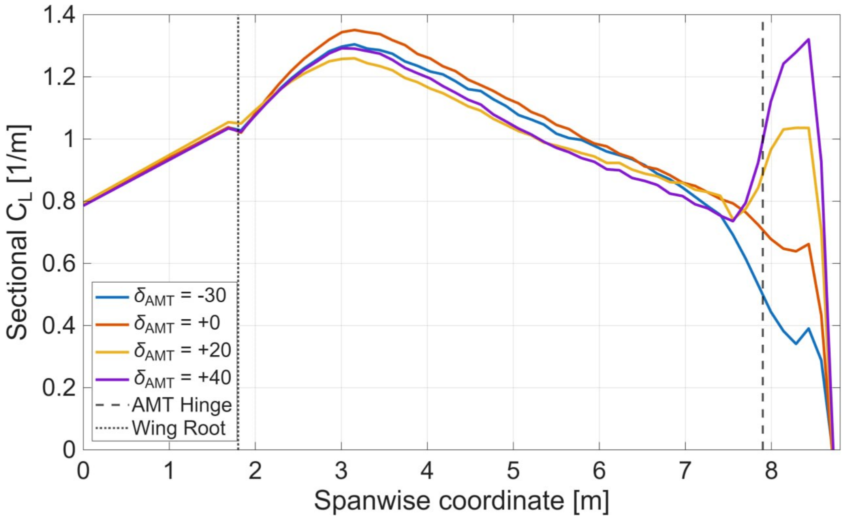

Figure 4.18: Spanwise distribution of the sectional lift coefficient for different AMT deflection angles, at $\alpha = 24°$.

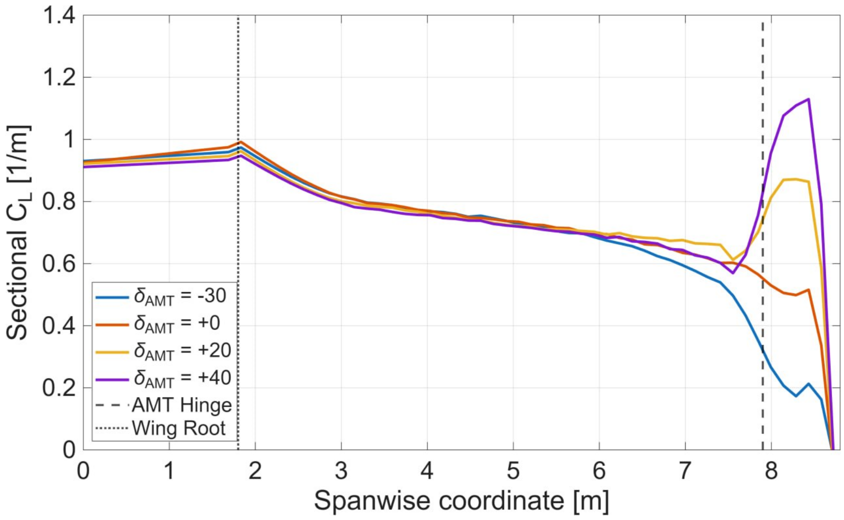

Figure 4.19: Spanwise distribution of the sectional lift coefficient for different AMT deflection angles, at $\alpha = 30°$.

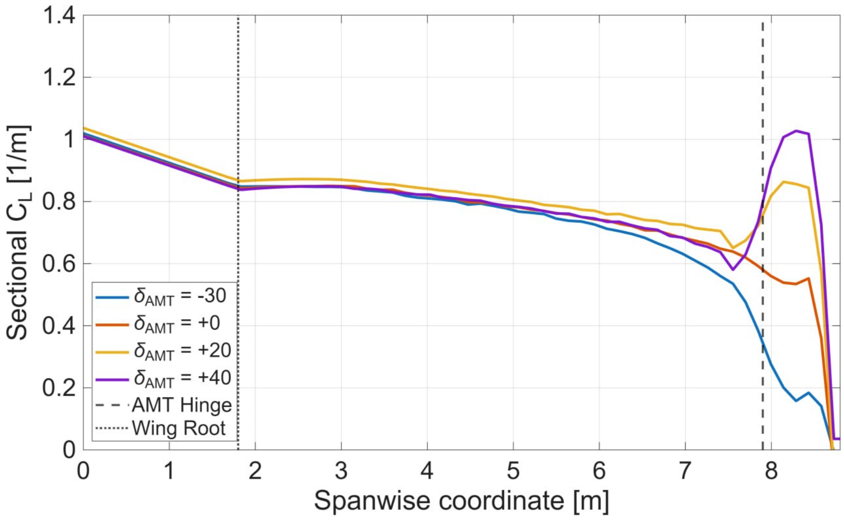

Figure 4.20: Spanwise distribution of the sectional lift coefficient for different AMT deflection angles, at $\alpha = 45°$.

Figures 4.17–4.20 show the spanwise distribution of the sectional lift coefficient, reported as $|C_{L,\text{sec}}|$, for four representative angles of attack and for different AMT deflection angles. The vertical dotted line identifies the wing-root station, whereas the dashed line marks the AMT hinge location.

At $\alpha = 15°$, Figure 4.17, the distribution is characterized by a pronounced lift peak on the fixed part of the wing, located approximately around $y \simeq 3.0$–3.3 m. This behaviour is consistent with the presence of a coherent leading-edge vortex over the highly swept wing. The vortex induces a strong suction region on the upper surface and produces an additional vortex-lift contribution, so that the maximum sectional loading is not located at the tip, but in the inner/intermediate span region where the vortex is still energetic and close to the surface. Downstream and outboard of this peak, the sectional lift coefficient decreases progressively up to the AMT hinge, as the vortex becomes more diffused and its suction effect on the wing surface is reduced.

At $\alpha = 24°$, Figure 4.18, the lift distribution shows a clear evolution: the main loading peak is shifted toward the semi-wing root. This behaviour suggests that the leading-edge vortex system has changed its position and strength as the incidence increases: the vortex still contributes to lift generation, but its strongest suction effect is now more concentrated in the inboard part of the wing. From this region outwards, $|C_{L,\text{sec}}|$ decreases progressively along the fixed wing up to the AMT hinge station.

At $\alpha = 30°$, Figure 4.19, the peak is reached right at the wing root. The sectional lift coefficient over the fixed wing remains relatively high near the inner part of the semi-wing, but then decreases progressively along the span. The absence of a strong mid-span peak suggests that the primary vortex has either moved farther away from the surface and become more diffuse. In this incidence range, the aerodynamic loading of the fixed wing is therefore less dominated by a concentrated vortex-lift peak and more by a gradual spanwise decay of the local lift contribution.

At $\alpha = 45°$, Figure 4.20, the distribution changes more significantly. The peak is on the centerline of the body and, near the wing root, the values of $|C_{L,\text{sec}}|$ are much lower than in the previous cases, indicating a substantial reduction of the local lift capability in the inner part of the wing. Moving outboard, the sectional lift coefficient progressively decreases toward the hinge. This behaviour is representative of a very high-incidence condition, where the flow field is strongly three-dimensional and largely separated.

Overall, the spanwise distributions show that the aerodynamic loading of the fixed wing changes substantially with the angle of attack. At moderate incidence, the lift is strongly influenced by a coherent leading-edge vortex, which produces a distinct sectional lift peak on the inner/intermediate portion of the wing. As the angle of attack increases, this peak becomes less pronounced, the loading distribution becomes smoother, and the lift contribution progressively shifts and weakens due to the evolution, diffusion and possible breakdown of the vortex system. At very high incidence, the distribution is broader and less intense, indicating a more separated and strongly three-dimensional flow field.

A common feature of all the distributions is that the AMT deflection has a limited effect on the most inboard part of the configuration. From the symmetry plane up to the wing-root station, the curves are almost coincident for all AMT deflections. This is expected, since the movable tip is located in the outer portion of the semi-wing and therefore produces only a weak upstream influence on the inner aerodynamic loading. The main differences between the configurations appear instead close to the hinge station and, more evidently, on the movable tip itself.

For positive deflections, especially for $\delta_{\text{AMT}} = +20°$ and $\delta_{\text{AMT}} = +40°$, the sectional lift coefficient increases in the movable-tip region. This local amplification is particularly evident for $\delta_{\text{AMT}} = +40°$, which produces a strong outboard loading peak at all the angles of attack considered. The positive AMT deflection increases the local effective incidence of the tip and modifies the interaction between the movable surface, the tip flow and the leading-edge vortex system, thereby enhancing the local suction and the sectional lift contribution.

The opposite behaviour is observed for the negative deflection. For $\delta_{\text{AMT}} = -30°$, the sectional lift coefficient decreases rapidly after the hinge, showing a clear unloading of the external portion of the semi-wing. This indicates that the negative AMT deflection reduces the local effective incidence of the tip and weakens the suction on the movable surface. As a result, the outboard loading becomes much lower than in the undeflected and positively deflected configurations. This unloading becomes particularly marked at high incidence, where the combination of negative AMT deflection and separated flow produces very low values of $|C_{L,\text{sec}}|$ near the outer tip.

It is also worth noting that all the curves exhibit a sharp decrease at the very last spanwise stations. This behaviour is mainly related to the finite tip geometry and to the rapid reduction of the local lifting surface near the outer boundary.

The spanwise lift distribution therefore confirms that the AMT can act as an effective local load-control device, capable of modifying the aerodynamic moments mainly through the redistribution of lift in the tip region.

4.5.4 Velocity field

$\delta_{AMT} = 20°$

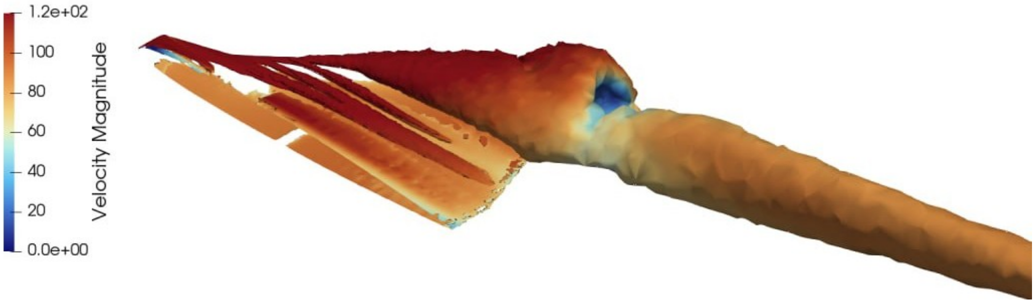

Figure 4.21: Velocity field around the semi wing, $\alpha = 15°$.

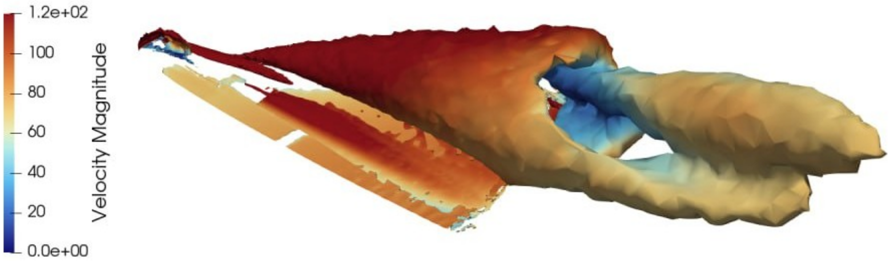

Figure 4.22: Velocity field around the semi wing, $\alpha = 24°$.

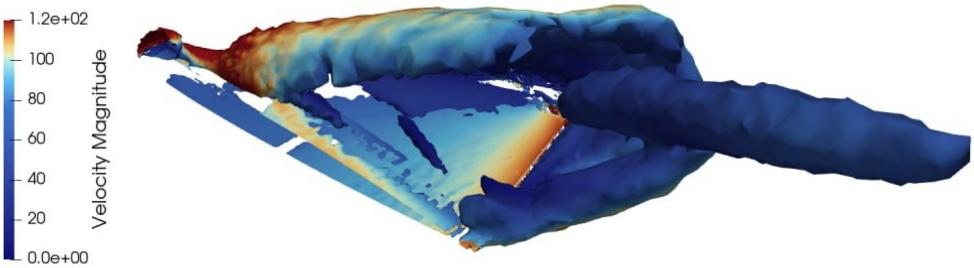

Figure 4.23: Velocity field around the semi wing, $\alpha = 30°$.

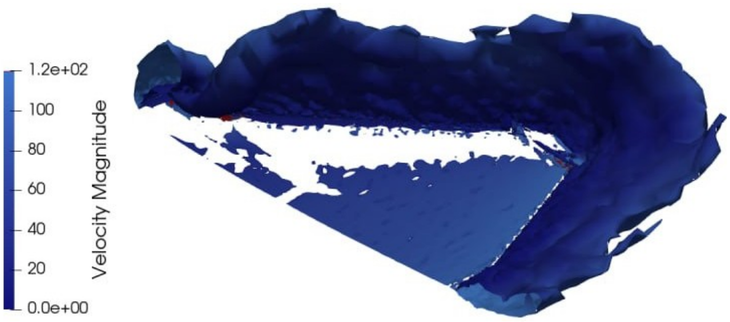

Figure 4.24: Velocity field around the semi wing, $\alpha = 45°$.

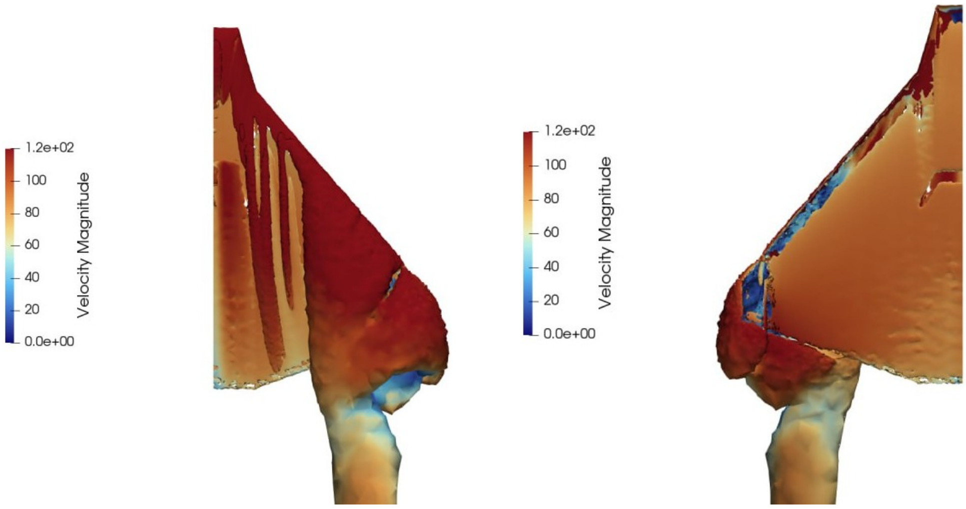

Figure 4.25: Velocity field over the upper (left) and lower (right) surfaces, $\alpha = 15°$.

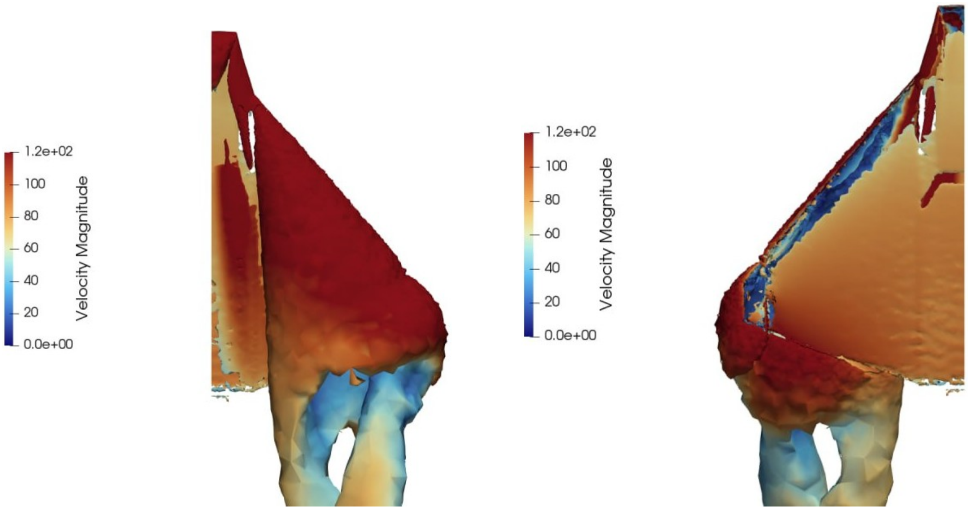

Figure 4.26: Velocity field over the upper (left) and lower (right) surfaces, $\alpha = 24°$.

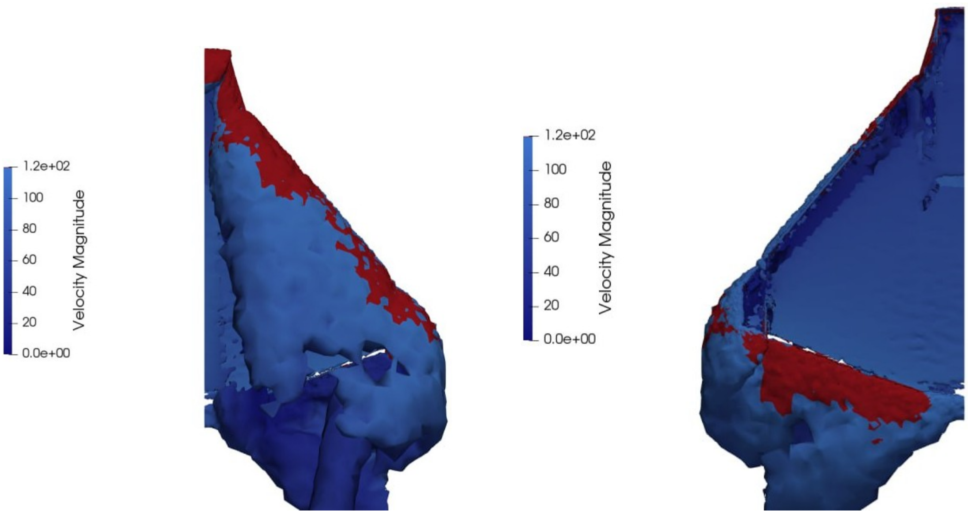

Figure 4.27: Velocity field over the upper (left) and lower (right) surfaces, $\alpha = 30°$.

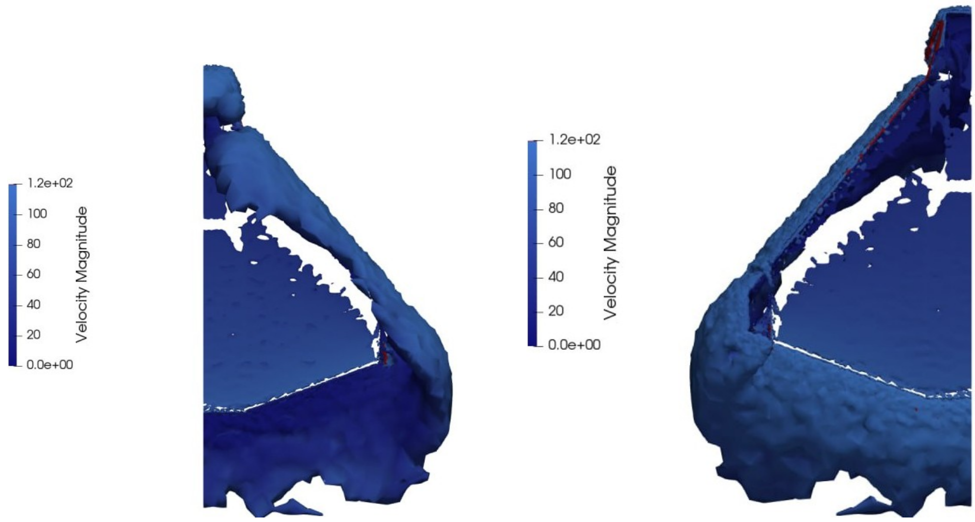

Figure 4.28: Velocity field over the upper (left) and lower (right) surfaces, $\alpha = 45°$.

The velocity-magnitude visualizations provide a qualitative description of the development of the vortical structures over the upper surface of the wing as the angle of attack is increased. At moderate incidence, the leading-edge vortex is still relatively coherent and remains close to the upper surface, promoting a local acceleration of the flow and contributing to the suction field generated on the wing.

As the angle of attack increases, the vortical structure grows in size and moves progressively away from the surface. The velocity field becomes less uniform, with the appearance of extended low-velocity regions associated with flow separation and vortex breakdown. This indicates a gradual loss of the organized leading-edge vortex system that characterizes the pre-stall aerodynamic regime.

At the highest angles of attack, the flow over the upper surface is largely separated. The vortex structure is no longer compact and well defined, and the velocity magnitude is significantly reduced over a large portion of the wing and in the wake region. This behaviour is consistent with the post-stall condition, in which the loss of coherent vortical suction leads to a reduction of the aerodynamic effectiveness of the configuration.

4.5.5 Yaw-control effectiveness

The yaw-control effectiveness of the AMT configuration was assessed by comparing the yawing-moment increment generated by a single all-moving tip with the corresponding directional-control authority of two conventional fighter configurations, namely the F-16 and the F/A-18. The comparison was carried out for three representative angles of attack, $\alpha = 10°$, $30°$ and $45°$, and for increasing values of the control-surface deflection δ.

Since the three configurations are characterized by significantly different control-surface sizes and moment arms, the comparison was performed in terms of yaw-control effectiveness normalized by the control-surface volume ratio. This choice allows the yawing-moment increment to be interpreted relative to the available geometric control volume of each effector, rather than only in terms of absolute control authority. In this way, the comparison accounts not only for the movable area of the control surface, but also for its effective lever arm with respect to the aircraft centre of gravity.

For the AMT configuration, the yawing-moment increment was obtained from the CFD results by comparing each deflected case with the corresponding undeflected configuration at the same angle of attack:

$$\Delta C_{n,\mathrm{body}}(\alpha, \delta_{\mathrm{AMT}}) = C_n(\alpha, \delta_{\mathrm{AMT}} = 0°) - C_n(\alpha, \delta_{\mathrm{AMT}}). \tag{4.13}$$

The AMT data refer to the deflection of a single all-moving tip installed on one semi-wing, while the opposite semi-wing is assumed to remain in clean configuration. The resulting yawing moment is therefore generated by an asymmetric modification of the aerodynamic loads, pressure distribution, separated-flow structure and drag contribution between the two sides of the aircraft.

The F-16 reference data were derived from the aerodynamic database reported by Nguyen et al. [15]. In this configuration, directional control is provided by a conventional rudder installed on the vertical tail. The rudder contribution is available as an aerodynamic increment associated with a full rudder deflection of $\delta_r = 30°$. Therefore, the yaw-control increment at full rudder deflection was evaluated as

$$\Delta C_{n,\mathrm{F16}}(\alpha, 30°) = C_n(\alpha, \beta = 0°, \delta_r = 0°) - C_n(\alpha, \beta = 0°, \delta_r = 30°). \tag{4.14}$$

The intermediate values of rudder deflection were then obtained by assuming a linear variation of the increment with rudder deflection:

$$\Delta C_{n,\mathrm{F16}}(\alpha, \delta_r) = \Delta C_{n,\mathrm{F16}}(\alpha, 30°)\frac{\delta_r}{30°}. \tag{4.15}$$

The F-16 reference quantities used in the present analysis are

$$S_{\mathrm{ref,F16}} = 27.87\ \mathrm{m}^2, \qquad b_{\mathrm{ref,F16}} = 9.144\ \mathrm{m}, \qquad \bar{c}_{\mathrm{F16}} = 3.45\ \mathrm{m}. \tag{4.16}$$

The F/A-18 reference data were obtained from the lateral-directional control derivatives extracted from flight data by Iliff and Wang [16]. The F/A-18 performs directional control through the rudders installed on the two canted vertical tails. For the F/A-18, the available quantity is the rudder yaw-control derivative $C_{n_{\delta_r}}$ as a function of angle of attack. Since this derivative is expressed per degree of rudder deflection, the incremental yawing-moment coefficient was estimated as

$$\Delta C_{n,\mathrm{F18}}(\alpha, \delta_r) \simeq C_{n_{\delta_r}}(\alpha)\,\delta_r. \tag{4.17}$$

The F/A-18 reference quantities used in the present comparison are

$$S_{\mathrm{ref,F18}} = 37.16\ \mathrm{m}^2, \qquad b_{\mathrm{ref,F18}} = 11.40\ \mathrm{m}, \qquad \bar{c}_{\mathrm{F18}} = 3.51\ \mathrm{m}. \tag{4.18}$$

The control-surface volume ratio was defined as

$$\bar{V} = \frac{S_{\mathrm{mov}}\, l_{\mathrm{ctrl}}}{S_{\mathrm{ref}}\, \bar{c}} = \frac{S_{\mathrm{mov}}}{S_{\mathrm{ref}}} \frac{l_{\mathrm{ctrl}}}{\bar{c}}, \tag{4.19}$$

where S_{mov} is the movable area of the control surface, S_{ref} is the reference wing area of the corresponding aircraft, l_{ctrl} is the effective moment arm of the effector with respect to the aircraft centre of gravity, and $\bar{c}$ is the mean aerodynamic chord. The ratio $\bar{V}$ therefore combines two relevant geometric effects: the relative size of the movable control surface and its relative lever arm. Normalizing the yawing-moment increment by $\bar{V}$ makes it possible to compare the different effectors in terms of yaw-control authority generated per unit geometric control volume.

The geometric quantities required for the volume-normalized comparison were extracted from the available reference data and from the three-view sketches of the two reference aircraft. The F-16 three-view sketch used for the estimation of the rudder movable area and effective moment arm is reported in Fig. 4.29. The corresponding F/A-18 geometry is reported in Fig. 4.30. For the F/A-18, the yaw-control data refer to symmetric double-rudder deflection; therefore, the movable area used in the normalization is the total area of the two rudders.

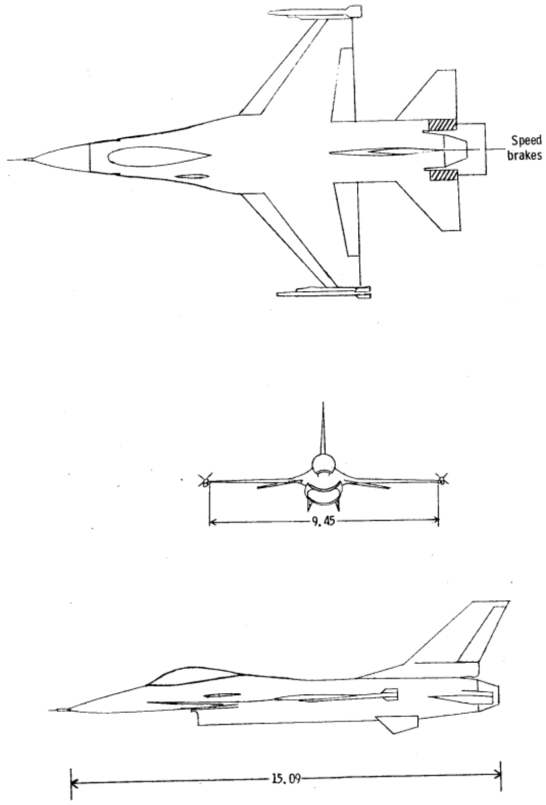

Figure 4.29: Three-view sketch of the F-16-based reference configuration [15].

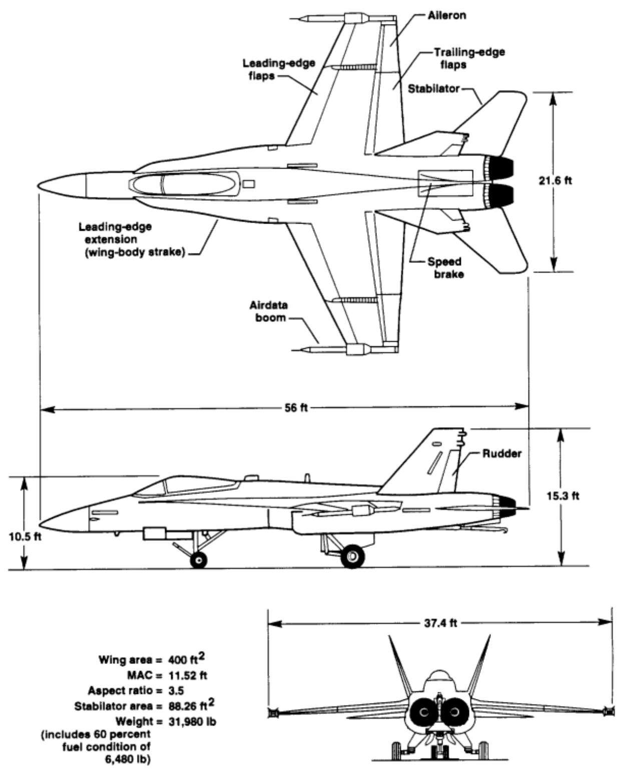

Figure 4.30: Three-view sketch of the F/A-18 reference configuration [16].

The geometric quantities used for the volume-normalized comparison are summarized in Table 4.7.

Table 4.7: Geometric quantities used for the yaw-control volume-normalized comparison.

Configuration	S_{mov} **[m^2]**	S_{ref} **[m^2]**	$\bar{S}$	l_{ctrl} **[m]**	$\bar{c}$ **[m]**	$\bar{V}$
Single AMT	2.154	100.00	0.0215	8.80	5.68	0.0334
F-16 rudder [15]	1.64	27.87	0.0588	6.65	3.45	0.1134
F/A-18 double rudder [16]	3.80	37.16	0.1023	7.80	3.51	0.2272

Figure 4.31 shows the yaw-control effectiveness comparison normalized by the control-surface volume ratio $\bar{V}$. The curves report the variation of the normalized yawing-moment increment with control-surface deflection for the AMT, the F-16 rudder and the F/A-18 double rudder at $\alpha = 10°$, $30°$ and $45°$. The quantity plotted in the figure is

$$\frac{\Delta C_{n,\mathrm{body}}}{\bar{V}} = \frac{C_n(\delta = 0°) - C_n(\delta)}{\bar{V}}. \tag{4.20}$$

This parameter represents the yaw-control effectiveness relative to the available geometric control volume of each effector. Therefore, the comparison does not only reflect the absolute yawing-moment increment, but also accounts for the different movable areas and moment arms of the considered control surfaces.

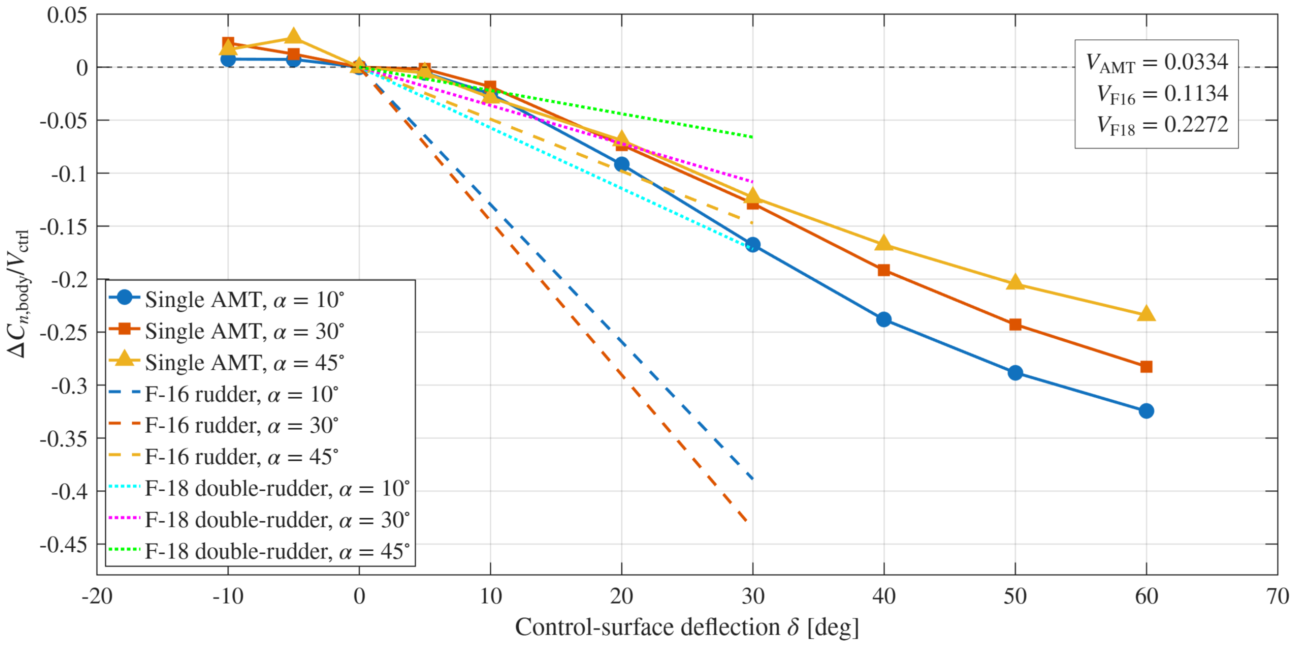

Figure 4.31: Yaw-control effectiveness comparison normalized by the control-surface volume ratio $\bar{V}$ [15] [16].

The AMT curves show that the yaw-control contribution increases with the deflection angle in a fairly regular way. This behaviour indicates that the AMT produces a consistent and progressive control response, in agreement with the expected design logic of a yaw-control effector based on aerodynamic asymmetry. Although the normalized increment remains limited at small deflections, the curves do not exhibit an early saturation and continue to grow up to the largest deflections investigated.

In the low-deflection range and at low angles of attack, the conventional rudders still provide a higher yaw-control effectiveness than the AMT. This is expected, since both the F-16 and the F/A-18 use dedicated directional-control surfaces specifically designed to generate side force on the vertical tail. In this operating range, the conventional rudder mechanism is still efficient: the flow over the vertical tail is sufficiently energetic and the rudder deflection produces a direct increase in side force, and therefore in yawing moment.

However, the effectiveness of the conventional rudders progressively decreases as the angle of attack increases. At high incidence, where the local flow over the vertical tails can be affected by separated and vortical structures generated by the forebody, wing and upstream airframe components. Under these conditions, the dynamic pressure available at the vertical tails may decrease and the rudder may become partially immersed in a degraded flow field, reducing its ability to generate an effective side-force increment.

It is also important to observe that the F-16 and F/A-18 reference curves are limited to rudder deflections of about $\delta_r = 30°$. This range is representative of the useful operating domain of conventional hinged rudders. For larger deflections, the aerodynamic response is no longer directly predictable from a linear or quasi-linear trend. The flow over the rudder and the aft portion of the vertical tail may separate, the rudder may approach a stalled condition, and the incremental side force may saturate or even decrease. Therefore, for conventional rudders, large deflections do not necessarily correspond to a further increase in yaw-control authority.

The AMT exhibits a different behaviour because its yaw-control mechanism is not based on the generation of attached-flow side force on a vertical surface. Instead, the AMT acts mainly as an asymmetric-drag yaw effector. Large AMT deflections modify the pressure distribution and separated flow structure over one wing tip, producing an asymmetric drag contribution with respect to the aircraft centreline. This asymmetric drag generates a yawing moment and becomes more relevant as the deflection angle increases.

For this reason, flow separation has a different role for the AMT than for a conventional rudder. In the case of a rudder, separation generally reduces the effectiveness of the control surface because it limits the side force that can be generated by the vertical tail. In the case of the AMT, instead, separated flow can contribute to the desired control mechanism by increasing the aerodynamic asymmetry between the two semi-wings. The AMT can therefore operate at much larger deflections because it does not rely on maintaining an attached flow over a conventional control surface. On the contrary, at high deflection it exploits a separated-flow, drag-based mechanism to generate yawing moment.

This explains why the AMT curves continue to increase up to $\delta_{\mathrm{AMT}} = 60°$, whereas the reference rudder curves are limited to $\delta_r = 30°$. At large AMT deflections, the volume-normalized AMT curves exceed the F/A-18 double-rudder curves and also exceed the F-16 rudder curve at $\alpha = 45°$. This does not imply that the AMT is globally more effective than a conventional rudder in terms of absolute directional-control authority. Rather, it shows that, when the generated yawing-moment increment is evaluated relative to the available geometric control volume, the AMT becomes particularly competitive in the large-deflection and high-angle-of-attack regime.

The key point is therefore that the AMT is able to preserve, and even enhance, its yaw-control effectiveness in conditions where conventional rudders tend to lose efficiency. This is a direct consequence of its physical operating mechanism: the AMT does not lose effectiveness simply because the local flow stalls, but can exploit the separated flow condition itself to increase the asymmetric drag contribution. In this sense, the AMT does not merely tolerate stall-like conditions at the wing tip; it uses them as part of its yaw control mechanism.

For this reason, the AMT appears to be a potentially valuable yaw-control effector for tailless or low-observability configurations, especially when vertical tails are reduced, shielded or removed. Its main interest lies in the ability to provide additional yaw authority through asymmetric drag using a relatively small movable surface and a compact geometric control volume.

4.5.6 Roll-control effectiveness

The roll-control effectiveness of the AMT configuration was assessed by analyzing the rolling-moment increment generated by the differential actuation of the two wing-tip effectors. The analysis is divided into two steps. First, the intrinsic roll-control authority of the AMT is examined by considering separately the two opposite effective-deflection branches, in order to identify the main aerodynamic trends and the relative effectiveness of the two wing-tip rotations. Then, the combined AMT contribution is compared with the corresponding roll-control authority of three reference fighter configurations, namely the F-16, the F/A-18 and the X-29A [15, 16, 17]. The comparison was carried out for three representative angles of attack, $\alpha = 10°$, $20°$ and $30°$, and for increasing values of the control-surface deflection.

Since the AMT is an all-moving surface, its aerodynamic effect is more properly interpreted in terms of orientation with respect to the incident flow, rather than only in terms of geometric deflection with respect to the aircraft body axes. For this reason, the AMT deflection used in the present analysis is defined as a prescribed offset with respect to a flow-aligned condition. In particular, for a given aircraft angle of attack, the AMT is assumed to be aligned with the undisturbed upstream flow when its geometric deflection is equal to $\delta_{\text{AMT},0} = -\alpha$. Starting from this reference condition, the two wing tips are then deflected asymmetrically in order to generate a rolling moment. According to the adopted sign convention, the geometric deflections of the left and right AMTs are defined as

$$\delta_{\text{AMT},L} = -\alpha + \delta_{\text{plot}}, \qquad \delta_{\text{AMT},R} = -\alpha - \delta_{\text{plot}}. \tag{4.21}$$

Therefore, δ_{plot} represents the AMT deflection with respect to the flow-aligned configuration, while the actual geometric setting of each tip depends on the aircraft angle of attack. In this way, the two AMTs operate with opposite effective incidences with respect to the incident flow, consistently with the differential actuation required for roll control.

This formulation tries to highlight one of the main advantages of the AMT concept. A conventional control surface is generally deflected with respect to the local aircraft geometry and remains constrained by the orientation of the fixed wing or tail surface on which it is installed. Conversely, an all-moving wing tip can be scheduled so as to maintain a more favorable orientation with respect to the incoming flow. This can be particularly relevant at high angles of attack, where a purely body-axis-based deflection would force the surface to operate at very large local incidences, increasing the risk of premature separation and loss of control effectiveness. By defining the AMT command relative to a flow-aligned condition, the movable tip can exploit smaller effective deflections with respect to the incident flow and can therefore retain useful aerodynamic authority over a wider incidence range.

It should be noted that the actual flow approaching the AMT is not perfectly aligned with this direction, because it is affected by the downwash induced by the main wing and by the vortical structures generated at high incidence. So, the most accurate implementation of this concept would require scheduling the AMT deflection with respect to the effective local flow seen by the movable tip. Nevertheless, the present formulation is useful because it illustrates the potential benefit of using the AMT as an all-moving effector, rather than as a conventional control surface simply deflected with respect to the aircraft body axes.

The AMT rolling-moment coefficient was obtained from the CFD simulations. For each angle of attack and plotted AMT deflection, the incremental rolling-moment coefficient was computed with respect to the corresponding flow-aligned AMT configuration:

$$\Delta C_{l,L}(\alpha, \delta_{\text{plot}}) = C_l(\alpha, -\alpha + \delta_{\text{plot}}) - C_l(\alpha, -\alpha), \tag{4.22}$$

$$\Delta C_{l,R}(\alpha, \delta_{\text{plot}}) = C_l(\alpha, -\alpha - \delta_{\text{plot}}) - C_l(\alpha, -\alpha). \tag{4.23}$$

This subtraction removes the baseline rolling-moment contribution associated with the AMT aligned with the incident flow and isolates the aerodynamic effect directly produced by the effective AMT deflection.

Since roll control is obtained by an asymmetric actuation of the two wing tips, the total AMT roll authority was evaluated by combining the contributions of the two opposite effective-deflection branches. The combined AMT roll authority was therefore computed as

$$\Delta C_{l,\text{AMT,comb}}(\alpha, \delta_{\text{plot}}) = \Delta C_{l,L}(\alpha, \delta_{\text{plot}}) - \Delta C_{l,R}(\alpha, \delta_{\text{plot}}). \tag{4.24}$$

This expression represents the equivalent rolling-moment increment produced by the two wing tips deflected asymmetrically with respect to the incident flow.

The F-16 data were derived from the NASA Technical Paper by Nguyen et al. [15], which describes a fighter configuration based on F-16 wind-tunnel data and uses nonlinear aerodynamic tables for the simulation of stall and post-stall characteristics. The primary roll-control effectors of the configuration are the conventional wing-mounted ailerons and the differential deflection of the horizontal stabilators. In the aerodynamic model, the rolling-moment coefficient is referenced to the aircraft body axes and is defined using the original F-16 reference area and span. The extracted F-16 rolling-control effectiveness was treated as a local linear control derivative over the considered deflection range. Therefore, the coefficient increment for a generic deflection was evaluated as

$$\Delta C_{l,\mathrm{F16}}(\alpha, \delta) = C_{l_\delta,\mathrm{F16}}(\alpha)\ \delta, \tag{4.25}$$

where $C_{l_\delta,\mathrm{F16}}$ is the rolling-control derivative extracted from the source data.

The F/A-18 data were taken from the lateral-directional stability and control derivatives reported by Iliff and Wang [16]. The source provides lateral-directional control derivatives extracted from flight tests of the basic F-18 aircraft over a high-angle-of-attack range. The derivatives were obtained through parameter identification from dynamic flight data using a maximum-likelihood estimator, with state noise included to account for uncommanded motions caused by separated and vortical flows at high incidence. The F/A-18 roll-control system uses a combination of ailerons, differential horizontal stabilators and, through the flight-control system, other scheduled lateral-directional control contributions.

Because the aileron and differential-stabilator deflections are strongly correlated in the flight data, Iliff and Wang define an equivalent lateral-control derivative. Above $\alpha = 15°$, the rolling-moment derivative due to this equivalent lateral control is given by

$$C_{l_{\delta_L}} = C_{l_{\delta_a}} + 0.42\ C_{l_{\delta_{dh}}}, \tag{4.26}$$

where δ_L denotes the equivalent lateral-control deflection, δ_a the aileron deflection and δ_{dh} the differential horizontal-stabilator deflection. For the comparison, the fairing of $C_{l_{\delta_L}}$ as a function of angle of attack was read from the published derivative plot and converted into rolling-moment increments through

$$\Delta C_{l,\mathrm{F18}}(\alpha, \delta) = C_{l_{\delta_L},\mathrm{F18}}(\alpha)\ \delta\ . \tag{4.27}$$

The value at $\alpha = 10°$ should be interpreted with some care, since the original source notes that below $\alpha = 15°$ the control-surface correlations and scheduling make the definition of a purely linear equivalent lateral control more complex.

The X-29A data were obtained from the lateral-directional stability and control derivatives reported by Iliff and Wang [17]. The X-29A is a useful reference configuration because it is an unconventional forward-swept wing aircraft specifically investigated at high angle of attack. Unlike conventional configurations with separate ailerons, spoilers or rolling tails, the X-29A uses its full-span wing flaperons differentially to provide roll control. A X-29A three-view sketch is reported in Fig. 4.32.

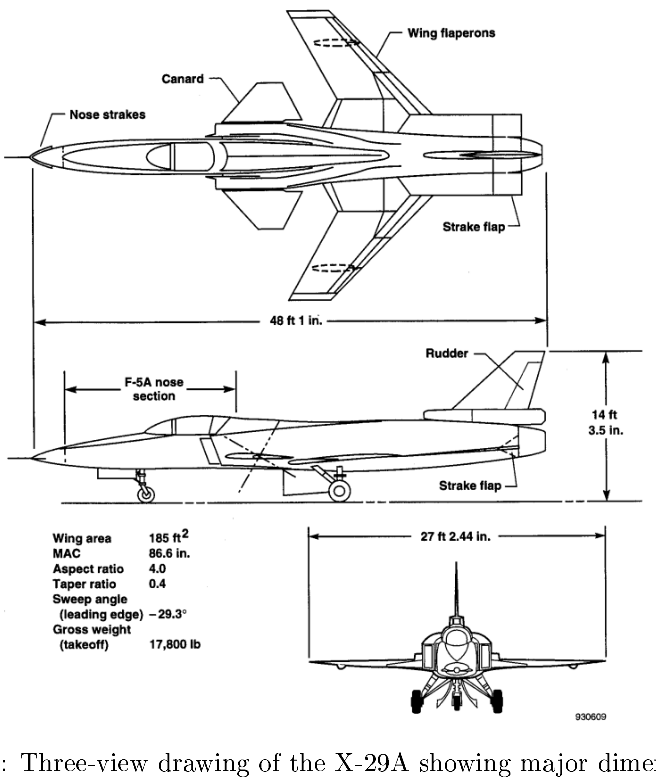

Figure 4.32: Three-view drawing of the X-29A showing major dimensions [19].

The cited report extracts the lateral-directional derivatives from flight data over a wide angle-of-attack range using a maximum-likelihood parameter-identification approach with state noise, similarly to the F/A-18 case.

For the present comparison, the X-29A rolling-control effectiveness was taken from the published derivative of rolling moment with respect to differential aileron, $C_{l_{\delta_a}}$, where the aileron variable represents the differential flaperon control input. The incremental rolling-moment coefficient was then evaluated as

$$\Delta C_{l,\mathrm{X29}}(\alpha, \delta) = C_{l_{\delta_a},\mathrm{X29}}(\alpha), \delta. \tag{4.28}$$

Figure 4.33 reports the absolute AMT rolling-control authority obtained by separating the two opposite effective-deflection branches. For each angle of attack, the plotted quantity is the absolute value of the incremental rolling-moment coefficient, $|\Delta C_l|$, evaluated with respect to the AMT configuration aligned with the incident flow. The abscissa reports the plotted deflection $|\delta_{\mathrm{plot}}|$, while the actual geometric AMT settings used on the two semi-wings are shifted by the aircraft angle of attack according to Eq. (4.21).

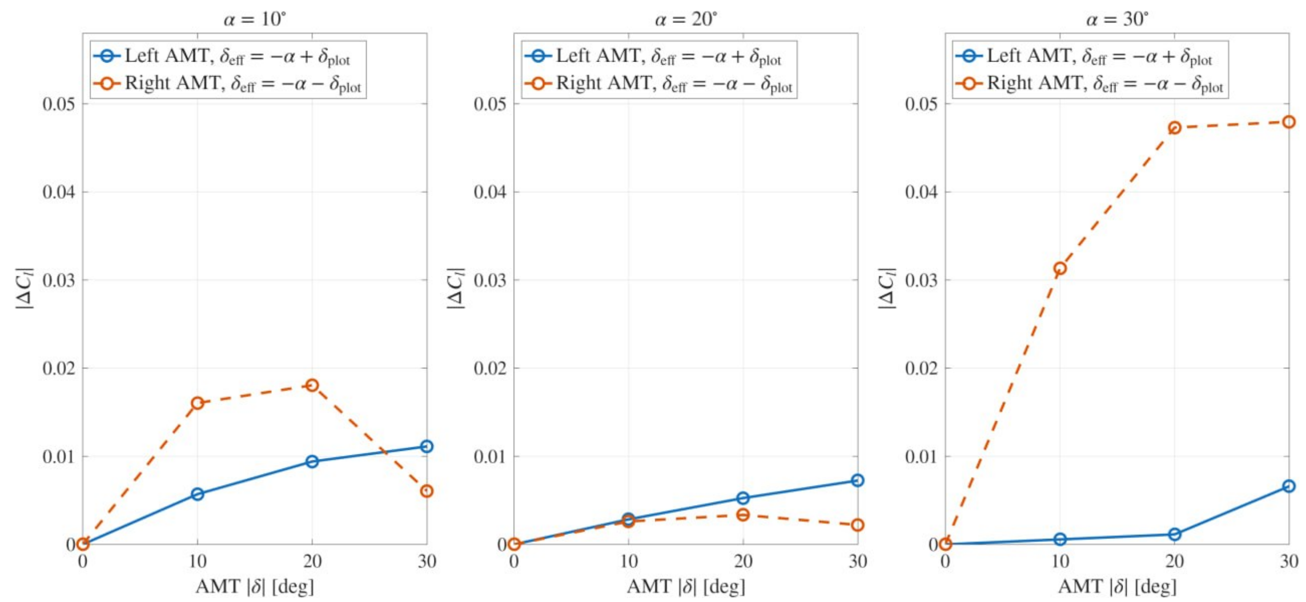

Figure 4.33: Absolute AMT rolling-control authority for opposite effective AMT deflections at $\alpha = 10°$, $20°$ and $30°$.

The first relevant result is the strong dependence of the AMT response on the sign of the effective deflection. At $\alpha = 10°$, the branch associated with $\delta_{\mathrm{eff}} = -\alpha - \delta_{\mathrm{plot}}$ (right AMT) produces the largest rolling-moment increment at low and moderate deflections. This indicates that, in this incidence range, rotating one tip in the negative effective-deflection direction produces a more pronounced redistribution of the outer-wing aerodynamic loading than the opposite rotation. However, the response is not purely monotonic: at the largest plotted deflection, the effectiveness of this branch decreases, suggesting that the local flow over the movable tip is approaching a saturated or partially separated condition. The opposite branch, associated with $\delta_{\mathrm{eff}} = -\alpha + \delta_{\mathrm{plot}}$ (left AMT), increases more gradually and provides a smaller but more regular contribution.

At $\alpha = 20°$, both branches produce more limited increments of $|\Delta C_l|$. The two curves are close to each other at small deflection, while the positive deflection branch (left AMT) becomes slightly more effective as $|\delta|$ increases. This behaviour suggests that, at this intermediate incidence, the AMT is still able to modify the local pressure distribution over the tip region, but the additional rolling-moment increment remains moderate. The main wing and tip flow are already affected by stronger three-dimensional and separated-flow effects, which reduce the sensitivity of the rolling moment to further AMT rotation.

At $\alpha = 30°$, the response changes significantly. The branch corresponding to $\delta_{\mathrm{eff}} = -\alpha - \delta_{\mathrm{plot}}$ dominates the roll-control contribution and produces a much larger rolling-moment increment than the opposite branch. Physically, this result shows that, at high incidence, using the AMT as an all-moving surface with respect to the incident flow allows the wing tip to strongly alter the outer-wing loading when one tip is rotated further in the negative effective-deflection direction. The resulting change in local pressure distribution and separated-flow topology generates a large differential aerodynamic loading between the two semi-wings. The positive deflection branch, instead, remains much weaker, meaning that the opposite rotation is less capable of producing an additional organized load increment under these high-incidence flow conditions.

Overall, Fig. 4.33 highlights that the AMT roll-control mechanism is highly asymmetric. The most effective branch depends on the incidence condition, but at high angle of attack the negative deflection branch becomes the dominant contributor to the rolling moment.

A second level of analysis was carried out by normalizing the roll-control authority with respect to the roll-control volume ratio. While the absolute increment of rolling-moment coefficient provides a direct measure of the control authority generated by each configuration, it does not account for the different geometric characteristics of the corresponding control effectors. In particular, the AMT, the F-16, the F/A-18 and the X-29A differ significantly in terms of movable surface area and lateral moment arm. Therefore, a direct comparison of $|\Delta C_l|$ alone would not distinguish between a configuration that produces a large rolling moment because of a large available control volume and one that uses a smaller effector more efficiently.

For this reason, the comparison was performed in terms of roll-control effectiveness normalized by the roll-control volume ratio. This normalization makes it possible to interpret the rolling-moment increment relative to the available geometric control volume of each effector, rather than only in terms of absolute control authority. In this way, the comparison accounts not only for the movable area of the control surface, but also for its effective lateral lever arm with respect to the aircraft centreline.

The roll-control volume ratio was defined as $\bar{V}_l = \sum_i (S_{\mathrm{mov},i} \cdot y_{\mathrm{ctrl},i})/(S_{\mathrm{ref}} \cdot b_{\mathrm{ref}})$,

where $S_{\mathrm{mov},i}$ is the movable area of the i-th roll-control surface, $y_{\mathrm{ctrl},i}$ is its effective lateral moment arm with respect to the aircraft centreline, S_{ref} is the aircraft reference wing area and b_{ref} is the reference span. The summation accounts for the fact that roll control is generally produced by differential or combined actuation of more than one surface. Therefore, $\bar{V}_l$ combines the relative movable area of the roll-control system and the lateral lever arm through which the generated aerodynamic force produces rolling moment.

For the AMT, the roll-control volume ratio was computed by considering the two wing tips acting differentially. For the reference aircraft, the same definition was applied to the equivalent roll-control systems considered in the comparison. The geometric quantities used for the volume-normalized roll-control comparison are summarized in Table 4.8.

Table 4.8: Geometric quantities used for the roll-control volume-normalized comparison.

Configuration	S_{ref} **[m^2]**	b_{ref} **[m]**	$\sum_i S_{\mathrm{mov},i}$ **[m^2]**	$\bar{V}_l$
AMT, combined	100.00	17.60	4.31	0.0215
F-16 [15]	27.87	9.144	5.92	0.0678
F/A-18 [16]	37.16	11.40	8.03	0.0456
X-29A [19]	17.187	8.292	3.44	0.0536

Figure 4.34 shows the roll-control effectiveness comparison normalized by the roll-control volume ratio $\bar{V}_l$. The curves report the variation of the normalized rolling-moment increment with the plotted AMT deflection for the combined AMT, the F-16, the F/A-18 and the X-29A at $\alpha = 10°$, 20° and 30°.

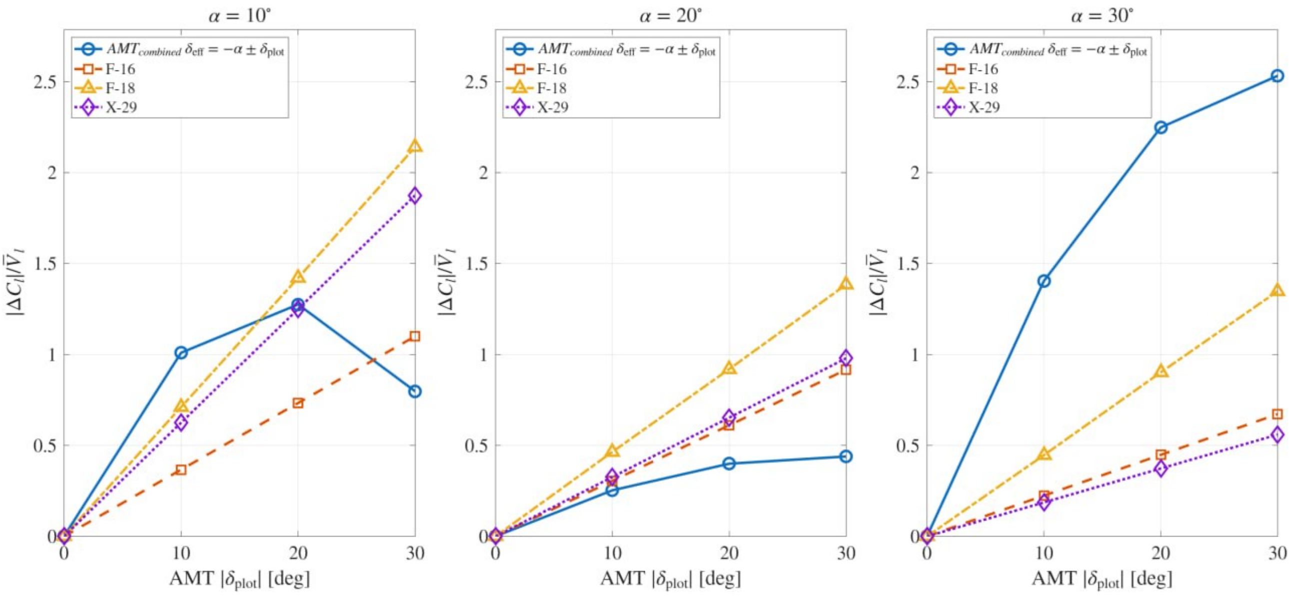

Figure 4.34: Rolling-control authority normalized by the control-surface volume ratio $\bar{V}_l$ for the AMT effective-deflection formulation [15] [16] [17].

Overall, the AMT curves show that the all-moving tip is able to generate a consistent roll-control contribution when it is actuated with respect to the incident-flow direction. The response is not simply proportional to the imposed deflection, because the AMT operates in a highly three-dimensional flow field where separation, downwash and vortical structures strongly affect the local aerodynamic loading of the tip region. Nevertheless, the results indicate that the AMT can produce a meaningful differential aerodynamic load between the two semi-wings. At moderate deflections, the rolling-moment increment generally increases with the AMT deflection, while at larger deflections local saturation or partial separation may limit the additional control authority.

At $\alpha = 10°$, the AMT provides a relevant roll control contribution over the low and moderate deflection range. In this condition, the combined AMT curve is higher than the F-16 curve and reaches a level comparable with the X-29A at intermediate deflections, while the F/A-18 remains one of the most effective reference configurations. At the largest plotted deflection, however, the AMT curve decreases. This reduction is consistent with the behaviour observed in Fig. 4.33: the dominant deflection branch (negative deflections) loses part of its incremental authority at large rotation, most likely because the local tip flow approaches a saturated or partially separated condition. Therefore, at low incidence the AMT is effective when used within a suitable deflection range, but its roll authority does not increase indefinitely with the commanded tip rotation.

At $\alpha = 20°$, the AMT curve becomes flatter and remains below the reference configurations over most of the deflection range. The normalized increment is still positive, but its slope is limited. This indicates that, at intermediate incidence, the all-moving tip is still able to generate a differential aerodynamic loading, although the local flow conditions over the outboard wing reduce the sensitivity of the rolling moment to additional AMT rotation. In this case, the CFD data show a relatively weak variation of C_l around the flow-aligned reference condition, which results in a smaller incremental rolling-moment coefficient. Physically, this suggests that the tip region is operating in a flow regime where the pressure redistribution induced by the AMT is less effective in producing additional roll authority. In the same incidence range, the F/A-18 and the X-29A benefit from roll-control systems distributed over larger portions of the lifting surface, while the AMT acts only on the compact tip region and is more sensitive to local separation and vortex interaction.

At $\alpha = 30°$, the AMT shows the strongest performance among the configurations considered. The combined AMT curve rises rapidly and remains above the F-16, F/A-18 and X-29A curves throughout the investigated range. This result shows a direct advantage of treating the AMT as an all-moving surface: at high angle of attack, when the two AMTs are then deflected asymmetrically with respect to the incident flow, the negative effective-deflection branch produces a strong change in the outer-wing loading. The resulting differential pressure field between the two semi-wings generates a large rolling-moment increment relative to the compact AMT control volume.

This behaviour shows that the AMT can exploit high-incidence flow physics in a way that differs from conventional roll-control surfaces. Ailerons, flaperons and differential stabilators are generally interpreted as surfaces that generate roll through incremental lift changes over predefined lifting surfaces. The AMT, instead, modifies the orientation of the entire wing-tip region with respect to the incoming flow. Consequently, its effectiveness is not governed only by a local control derivative, but also by the interaction between the movable tip, the separated flow over the main wing and the vortical structures developing at high angle of attack. This explains why the AMT response is strongly dependent on both angle of attack and sign of the effective deflection.

The comparison with the reference configurations also clarifies the different nature of the AMT roll-control mechanism. The F-16 combines conventional wing-mounted ailerons and differential horizontal-tail deflection; the F/A-18 uses an equivalent lateral-control system involving ailerons, differential stabilators and scheduled lateral-directional control contributions; while the X-29A uses full-span differential flaperons. These systems are specifically designed to provide robust roll authority over a broad operating envelope. The AMT, on the other hand, is a compact outboard effector whose authority is more localized and more sensitive to the local flow regime. Nevertheless, when its deflection is defined with respect to the incident flow, the AMT can provide a competitive volume-normalized roll contribution, especially at high incidence.

Overall, the roll-control analysis shows that the AMT is a promising auxiliary or complementary roll-control effector. Its compact geometry, outboard location and compatibility with low-observability layouts make it attractive as part of a broader control allocation strategy. The present effective-deflection formulation also shows that the AMT should not be evaluated only as a conventional surface deflected with respect to the aircraft body axes: when it is used as an all-moving surface relative to the incoming flow, it can generate a significant rolling-moment increment, with particularly strong effectiveness at high angle of attack. At the same time, the marked asymmetry between the two effective-deflection branches indicates that its use should be carefully scheduled as a function of incidence and deflection sign, in order to exploit the most favorable aerodynamic branch while avoiding ineffective or saturated operating conditions.

4.5.7 Pitch-control effectiveness

The pitch-control effectiveness of the AMT configuration was assessed by comparing the pitching-moment increment generated by the symmetric actuation of the two all-moving tips with the corresponding pitch-control authority of three reference fighter configurations, namely the F-16, the F/A-18 HARV and the X-29A. The comparison was carried out for three representative angles of attack, $\alpha = 10°$, $20°$ and $30°$, and for increasing values of the control-surface deflection.

Since the considered configurations are characterized by significantly different movable-surface areas and longitudinal moment arms, the comparison was performed in terms of pitch-control effectiveness normalized by the control-surface volume ratio. This choice allows the pitching-moment increment to be interpreted relative to the available geometric control volume of each effector, rather than only in terms of absolute control authority. In this way, the comparison accounts not only for the movable area of the control surface, but also for its effective longitudinal lever arm with respect to the aircraft centre of gravity.

For the AMT configuration, the two all-moving tips are assumed to be deflected symmetrically, namely $\delta_{\mathrm{AMT,L}} = \delta_{\mathrm{AMT,R}}$. The resulting pitching moment is therefore generated by a symmetric modification of the aerodynamic loads on the two wing tips.

Unlike a conventional hinged control surface, however, the AMT is treated as an all-moving surface whose orientation can be prescribed independently from the fixed part of the aircraft. For this reason, in the present comparison the AMT deflection plotted in the figure (δ_{plot}) is defined with respect to the undisturbed upstream flow direction.

Starting from the CFD database, in which the AMT deflection is defined with respect to the aircraft body-fixed reference, the corresponding effective AMT deflection used to sample the numerical data is $\delta_{\mathrm{eff}} = \delta_{\mathrm{plot}} - \alpha$. Therefore, for each prescribed value of δ_{plot}, the AMT pitching-moment coefficient is evaluated at the body-referenced deflection δ_{eff}. The same transformation is applied to the zero-command reference condition. Consequently, the incremental AMT pitching-moment coefficient is computed as

$$\Delta C_{m,\mathrm{AMT}}(\alpha, \delta_{\mathrm{plot}}) = C_m\left(\alpha, \delta_{\mathrm{eff}} = \delta_{\mathrm{plot}} - \alpha\right) - C_m\left(\alpha, \delta_{\mathrm{eff}} = -\alpha\right). \tag{4.29}$$

This formulation makes the AMT increment equal to zero for $\delta_{\mathrm{plot}} = 0°$, namely when the all-moving tip is aligned with the undisturbed upstream flow.

This choice is intended to exploit the specific nature of the AMT as an all-moving surface. A conventional control surface, such as an elevator, stabilator or canard, is generally deflected with respect to the aircraft body or to the parent lifting surface. The AMT, instead, can in principle be oriented independently, allowing the control command to be defined relative to an external aerodynamic reference. In the present analysis, the undisturbed upstream flow direction is used as a first reference direction in order to highlight the possible benefit of using the AMT as an independently oriented all-moving surface, rather than as a conventional body-referenced control surface.

It should be noted that the most effective implementation would require the AMT deflection to be prescribed with respect to the actual local flow incident on the tip surface. This local flow is not generally aligned with the freestream, because it is affected by the downwash induced by the wing and by the vortical structures generated at high angle of attack. Therefore, a more refined control law should account for the local flow-angle deviation at the AMT location and should tune the AMT orientation accordingly. The present analysis does not introduce this additional local-flow correction, but uses the upstream freestream direction as a simplified reference to investigate the potential advantages of an AMT application different from that of conventional control effectors.

For the F-16, the pitch-control data were taken from the aerodynamic database reported by Nguyen et al. [15], which refers to a relaxed-static-stability fighter configuration based on the F-16. In this configuration, the primary longitudinal control is provided by the symmetric deflection of the horizontal stabilator δ_h (with positive δ_h corresponding to airplane nose-down control). The published curves of C_m as a function of angle of attack for different stabilator deflections were digitized and interpolated. The F-16 pitching-moment increment was then computed as

$$\Delta C_{m,\mathrm{F16}}(\alpha, \delta_h) = C_{m,\mathrm{F16}}(\alpha, \delta_h) - C_{m,\mathrm{F16}}(\alpha, \delta_h = 0°). \tag{4.30}$$

Intermediate deflection values were obtained through interpolation between the available stabilator curves.

For the F/A-18 HARV, the comparison was based on the flight-determined subsonic longitudinal stability and control derivatives reported by Iliff and Wang [18]. The reference aircraft is the NASA F-18 High Angle of Attack Research Vehicle (HARV), for which conventional aerodynamic pitch control is provided by the collective deflection of the all-moving horizontal stabilators, together with the scheduled symmetric leading- and trailing-edge flap contributions. The relevant quantity extracted from the reference data is the pitching-moment derivative with respect to stabilator deflection, $C_{m_{\delta_e}}$, reported as a function of angle of attack. Therefore, the incremental pitching-moment coefficient was estimated as

$$\Delta C_{m,\mathrm{F18}}(\alpha, \delta_e) \simeq C_{m_{\delta_e}}(\alpha)\,\delta_e. \tag{4.31}$$

For the X-29A, the reference data were obtained from the predicted pitching moment characteristics reported by Budd [20]. The X-29A is characterized by a close-coupled canard and a three-surface longitudinal control system. In the present comparison, the canard was selected as the reference pitch-control effector, since it represents the dominant longitudinal-control surface. The reference report provides the pitching-moment coefficient C_M as a function of lift coefficient C_L for different canard deflections DC (with positive DC corresponding to trailing-edge-down canard rotation). For each AMT angle of attack considered in the comparison, the corresponding clean AMT lift coefficient was used to define an equivalent C_L, and the X-29A pitching moment was interpolated at that value. The incremental coefficient was then computed as

$$\Delta C_{m,\mathrm{X29}}(C_L, DC) = C_{m,\mathrm{X29}}(C_L, DC) - C_{m,\mathrm{X29}}(C_L, DC = 0°). \tag{4.32}$$

The pitch-control volume ratio was defined as

$$\bar{V}_m = \frac{S_{\mathrm{mov}}\, l_{\mathrm{ctrl}}}{S_{\mathrm{ref}}\, \bar{c}} = \frac{S_{\mathrm{mov}}}{S_{\mathrm{ref}}} \frac{l_{\mathrm{ctrl}}}{\bar{c}}, \tag{4.33}$$

where S_{mov} is the movable area of the pitch-control surface, S_{ref} is the reference wing area of the corresponding aircraft, l_{ctrl} is the longitudinal moment arm of the effector with respect to the aircraft centre of gravity, and $\bar{c}$ is the mean aerodynamic chord.

For the AMT, the longitudinal moment arm used in the pitch-volume ratio was obtained from the reference geometry as the distance between the centre of gravity and the AMT hinge-axis reference point:

$$l_{\mathrm{ctrl,AMT}} = |x_{\mathrm{hinge,AMT}} - x_{\mathrm{CG}}| = |10.900 - 8.600| = 2.300 \text{ m}, \tag{4.34}$$

and, since pitch control is obtained through symmetric actuation, the movable area used for the AMT normalization is the total area of the two all-moving tips.

The geometric quantities used for the pitch-control volume-normalized comparison are summarized in Table 4.9.

Table 4.9: Geometric quantities used for the pitch-control volume-normalized comparison.

Configuration	**Pitch surface**	S_{mov} **[m²]**	S_{ref} **[m²]**	$\bar{c}$ **[m]**	l_{ctrl} **[m]**	$\bar{V}_m$
AMT	symmetric AMT	4.308	100.00	5.68	2.30	0.0174
F-16 [15]	total stabilator	5.92	27.87	3.45	6.40	0.394
F/A-18 HARV [16]	total stabilator	8.03	37.16	3.51	6.90	0.425
X-29A [19]	canard, DC	3.44	17.187	2.20	4.50	0.409

Figure 4.35 shows the pitch-control effectiveness comparison normalized by the pitch-control volume ratio $\bar{V}_m$. The curves report the variation of the normalized pitching-moment increment with control-surface deflection for the AMT, the F-16 stabilator, the F/A-18 HARV stabilator and the X-29A canard at $\alpha = 10°$, $20°$ and $30°$. For the AMT, the plotted deflection is δ_{plot}, namely the AMT orientation with respect to the undisturbed upstream flow. The quantity reported in the figure is

$$\frac{|\Delta C_m|}{\bar{V}_m} = \frac{|C_m(\delta) - C_m(\delta = 0°)|}{\bar{V}_m}, \tag{4.35}$$

where, for the AMT, the increment is evaluated according to Eq. (4.29). This parameter represents the pitch-control effectiveness relative to the available geometric control volume of each effector. Therefore, the comparison does not only reflect the absolute pitching-moment increment, but also accounts for the different movable areas and longitudinal moment arms of the considered control surfaces.

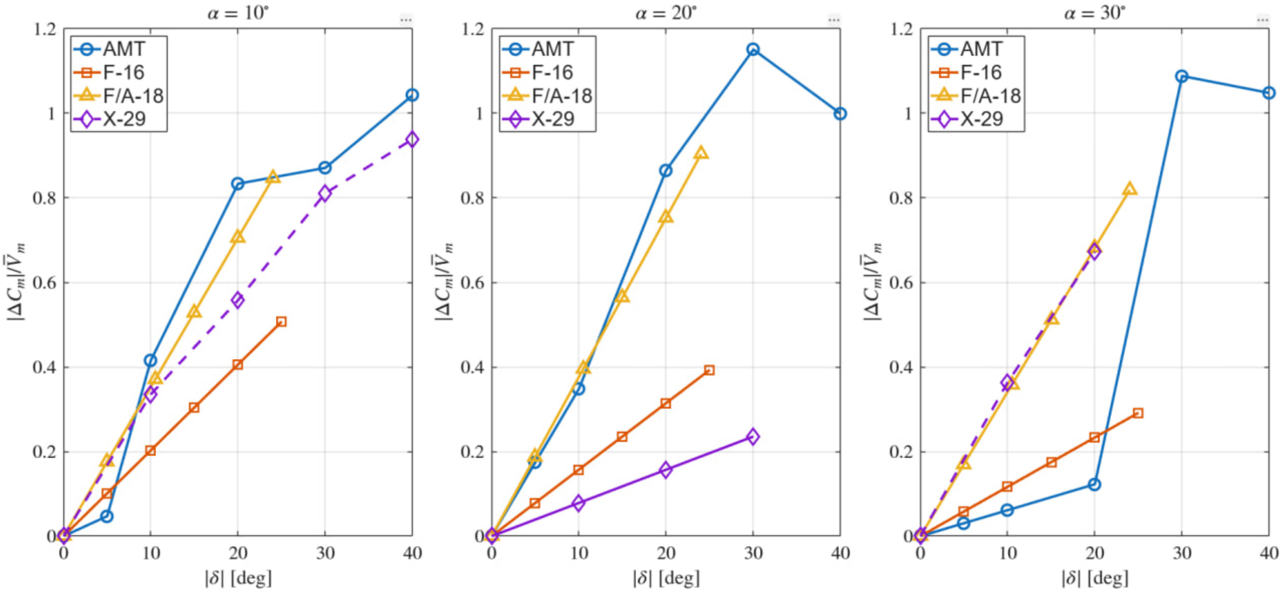

Figure 4.35: Pitch-control effectiveness comparison normalized by the pitch-control volume ratio $\bar{V}_m$. For the AMT, the plotted deflection is referred to the undisturbed upstream flow direction [15] [16] [19].

The results show that the AMT produces a clear and physically consistent pitch-control response. For the three angles of attack considered, the volume-normalized AMT effectiveness generally increases with the prescribed deflection, indicating that the symmetric rotation of the two all-moving tips generates a progressive pitching-moment increment. The response is not purely linear, especially at the highest angle of attack, but it remains predictable in the sense that larger AMT deflections generally produce larger control effects.

In absolute terms, the AMT pitch authority remains penalized by the present geometric installation. The two movable tips have a relatively small movable area and, more importantly, a limited longitudinal moment arm with respect to the pitch axis passing through the aircraft centre of gravity. In the present configuration, this arm is much shorter than that of dedicated longitudinal-control surfaces such as stabilators or canards. As a consequence, even a significant local aerodynamic-load variation on the AMT produces only a limited absolute pitching-moment increment at aircraft level.

The volume-normalized comparison provides a different interpretation. By dividing the pitching-moment increment by the pitch-control volume ratio $\bar{V}_m$, the direct dependence on the movable area and on the longitudinal control arm is removed, at least to first order. Under this interpretation, when the generated moment is evaluated per unit geometric control volume, the AMT reaches levels of effectiveness that are comparable with, and in several regions higher than, those of the conventional reference effectors.

At $\alpha = 10°$, the AMT curve increases rapidly between $|\delta| = 5°$ and $20°$, reaching values comparable with the F/A-18 HARV stabilator and higher than the F-16 stabilator. At larger deflections, the AMT remains among the most effective configurations in the volume-normalized comparison and exceeds the X-29A canard at the largest deflection shown. This indicates that, once the small AMT control volume is accounted for, the all-moving tip can provide a competitive pitch-control contribution even though its absolute moment authority remains limited.

At $\alpha = 20°$, the AMT becomes even more competitive. At low deflections, its normalized effectiveness is close to that of the F/A-18 HARV, while for $|\delta| \gtrsim 20°$ it becomes the largest among the configurations considered. The curve reaches its maximum around $|\delta| = 30°$ and then slightly decreases at $|\delta| = 40°$. This mild reduction suggests the onset of nonlinear aerodynamic effects at large deflection, but the AMT still maintains a high normalized effectiveness.

At $\alpha = 30°$, the AMT behaviour is markedly nonlinear. For small and moderate deflections, up to approximately $|\delta| = 20°$, the AMT normalized contribution remains lower than that of the F/A-18 HARV and X-29A. However, between $|\delta| = 20°$ and $30°$ the AMT effectiveness increases sharply and becomes higher than all the reference configurations. This sudden growth is consistent with a strong reorganization of the local flow field at the wing tip, where downwash, vortex-induced flow deviation and possible separated-flow regions can significantly modify the aerodynamic response of the all-moving surface.

The comparison should therefore be interpreted carefully. The F-16 stabilator, the F/A-18 HARV stabilator and the X-29A canard are dedicated longitudinal-control surfaces, placed at favorable longitudinal distances from the centre of gravity and specifically designed to generate pitching moment. Their large absolute authority is therefore the result of both favorable aerodynamic loading and favorable geometric placement. The AMT, instead, acts on a small outboard portion of the wing and is geometrically more suited to roll control and, through asymmetric drag, to yaw control. Its lower absolute pitch authority is therefore mainly a consequence of the installation geometry, rather than of a poor aerodynamic response of the all-moving tip itself.

Overall, the volume-normalized pitch-control comparison leads to a more balanced interpretation than a purely absolute comparison. In the present configuration, the AMT should not be considered a direct substitute for a conventional primary pitch-control surface, because its absolute pitching moment remains limited by the short longitudinal arm and by the small movable area. However, once these geometric limitations are accounted for through the volume-ratio normalization, the AMT shows a good and physically consistent pitch-control effectiveness. This suggests that the concept can provide a useful secondary pitch contribution within a broader multi-axis control-allocation strategy, especially for compact, tailless or low-observability configurations where the integration of large conventional control surfaces may be constrained.

The second part of the analysis focuses on the ability of the AMT to trim the configuration in pitch. The trim condition is defined by

$$C_m(\alpha, \delta_{\mathrm{AMT}}) = 0. \tag{4.36}$$

Figure 4.36 shows a zoom of the pitching-moment coefficient in the region where the AMT curves intersect the line $C_m = 0$. The shaded region highlights the range of trim incidences obtained with the positive AMT deflections considered in the analysis.

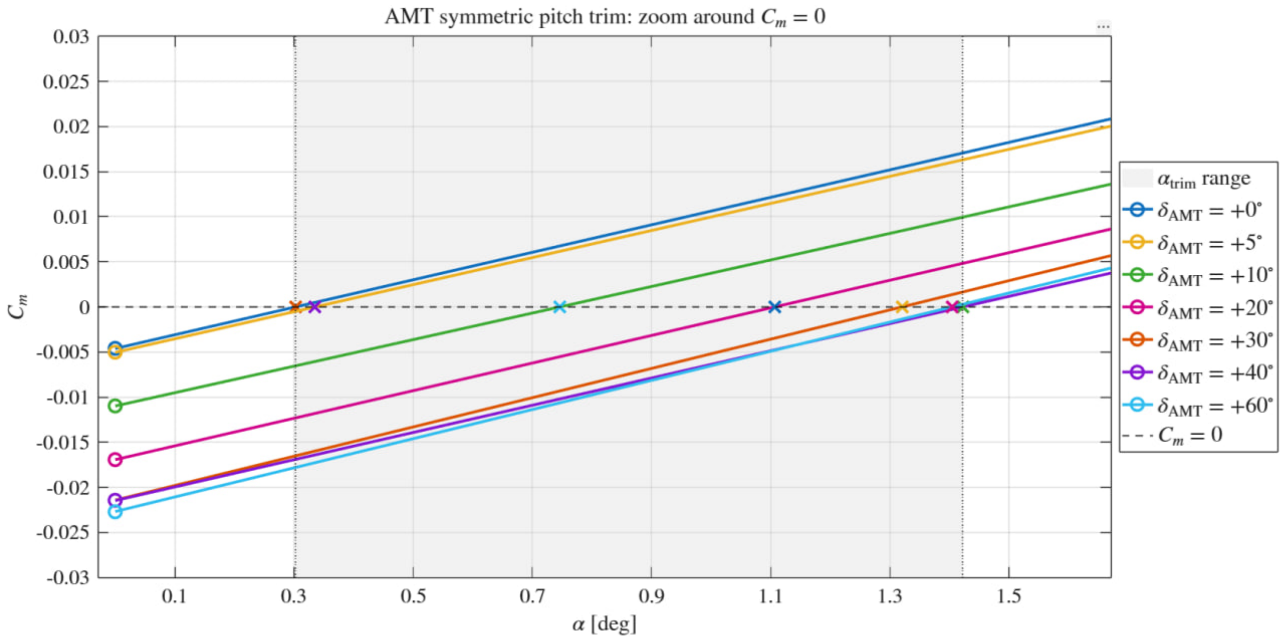

Figure 4.36: Zoom of the AMT pitching-moment coefficient around the $C_m = 0$ trim condition for positive AMT deflections. The shaded area highlights the resulting trim-incidence interval.

The result shows that the configuration is trimmable only over a very narrow range of angle of attack, close to $\alpha = 0°$. In particular, the positive AMT deflections considered in the zoom provide trim only between approximately

$$\alpha_{\mathrm{trim},1} \simeq 0.30° \quad \text{and} \quad \alpha_{\mathrm{trim},2} \simeq 1.42°. \tag{4.37}$$

This trend is consistent with the fact that, in the present installation, the AMT produces only a weak pitch contribution.

The trim condition is obtained through positive AMT deflections, namely through a trailing-edge-down rotation according to the adopted sign convention.

For each AMT deflection, the trim angle of attack was obtained by linearly interpolating the $C_m(\alpha)$ curve in the neighbourhood of the zero crossing.

Figure 4.37 summarizes the trim command required by the AMT. The upper plot reports the trim angle of attack α_{trim} as a function of the AMT deflection, whereas the lower plot reports the corresponding drag coefficient evaluated at the trim condition:

$$C_{D,\text{trim}}(\delta_{\text{AMT}}) = C_D\left(\alpha_{\text{trim}}, \delta_{\text{AMT}}\right). \tag{4.38}$$

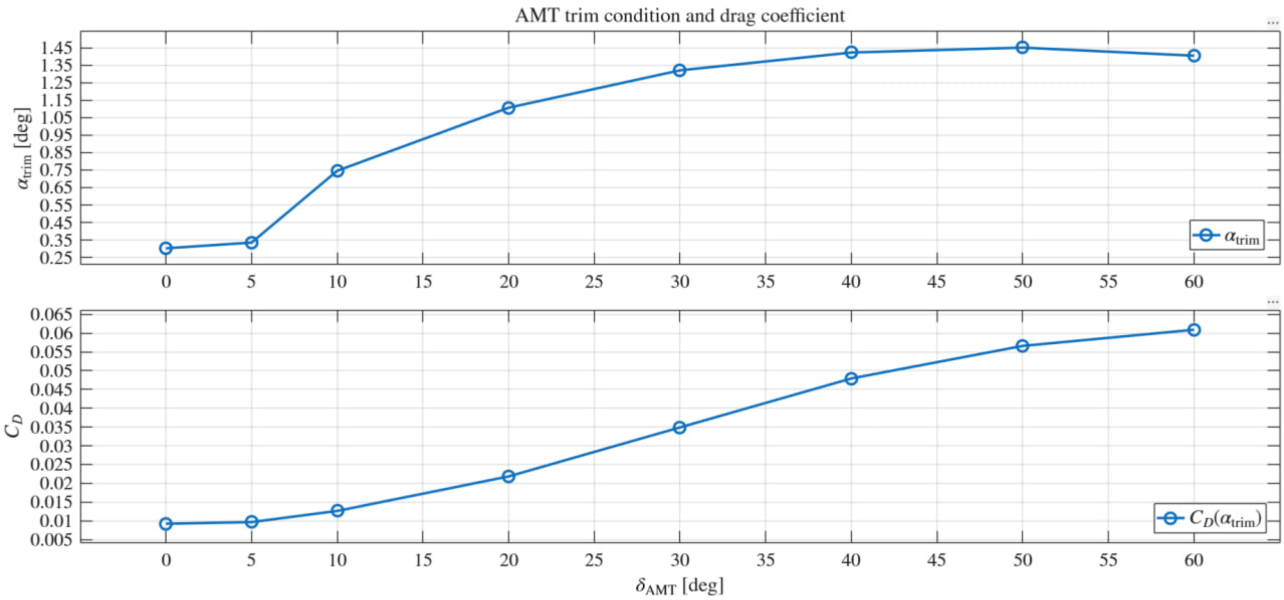

Figure 4.37: AMT trim angle of attack and drag coefficient at trim as a function of AMT deflection. The point at $\delta_{\text{AMT}} = 50°$ is obtained through local quadratic interpolation, while all the other points are CFD-based.

The upper plot shows that, as the trimmed angle of attack increases, a larger positive AMT deflection is required to keep the pitching-moment coefficient at zero. However, the achievable trim envelope remains extremely limited.

The trim incidence increases rapidly as the AMT deflection is increased from 0° to approximately 30°. Beyond this value, the curve tends to flatten: the trim angle reaches about 1.42° at $\delta_{\text{AMT}} = 40°$, about 1.45° at $\delta_{\text{AMT}} = 50°$, and then slightly decreases to about 1.40° at $\delta_{\text{AMT}} = 60°$. This behaviour indicates that the AMT trim capability approaches a saturation condition at large positive deflections.

The lower plot shows how the drag coefficient at trim increases with the AMT deflection. In the analysed range, $C_{D,\text{trim}}$ increases from approximately 9×10^{-3} at $\delta_{\text{AMT}} = 0°$ to approximately 6.1×10^{-2} at $\delta_{\text{AMT}} = 60°$. Therefore, large positive AMT deflections produce a considerable drag penalty while providing only a marginal increase in trim angle of attack.

This result further confirms that, in the present configuration, the AMT is not an efficient device for longitudinal trim. The physical reason is the same identified in the control-effectiveness comparison: the AMT acts on a localized outboard portion of the wing, with a very limited longitudinal moment arm with respect to the aircraft centre of gravity. So, large deflections are required to generate even small pitching-moment corrections, and these deflections are accompanied by a noticeable drag increase.

4.5.8 Hinge moment

The hinge-moment coefficient was analysed in order to evaluate the aerodynamic torque acting on the All-Moving Tip about its rotation axis, which must be balanced by the actuation system. So, from an integration point of view, the hinge moment provides a direct indication of the actuation effort required to hold the AMT at a prescribed deflection angle. In the present work, the hinge-moment coefficient is denoted as C_h and was non-dimensionalized using the AMT planform area and the mean aerodynamic chord of the movable tip:

$$C_h = \frac{M_h}{q_\infty S_{\mathrm{AMT}} \bar{c}_{\mathrm{AMT}}},$$

where M_h is the aerodynamic moment about the AMT hinge axis, q_∞ is the free-stream dynamic pressure, S_{AMT} is the AMT planform area and $\bar{c}_{\mathrm{AMT}}$ is the AMT mean aerodynamic chord.

The analysis was conducted by considering two complementary representations. First, C_h was plotted as a function of the AMT deflection angle for selected values of angle of attack. Then, C_h was plotted as a function of the angle of attack for selected AMT deflections. In this way, it is possible to separate the effect of the commanded AMT rotation from the effect of the global aerodynamic state of the wing.

According to the reference frame and sign convention adopted in the present study, a negative value of C_h corresponds to an aerodynamic hinge moment tending to rotate the AMT leading edge downward. Since a positive AMT deflection is defined as an upward rotation of the AMT leading edge, a negative C_h generally acts in the direction of reducing a positive AMT deflection. Conversely, positive values of C_h indicate an aerodynamic moment tending to rotate the AMT leading edge upward.

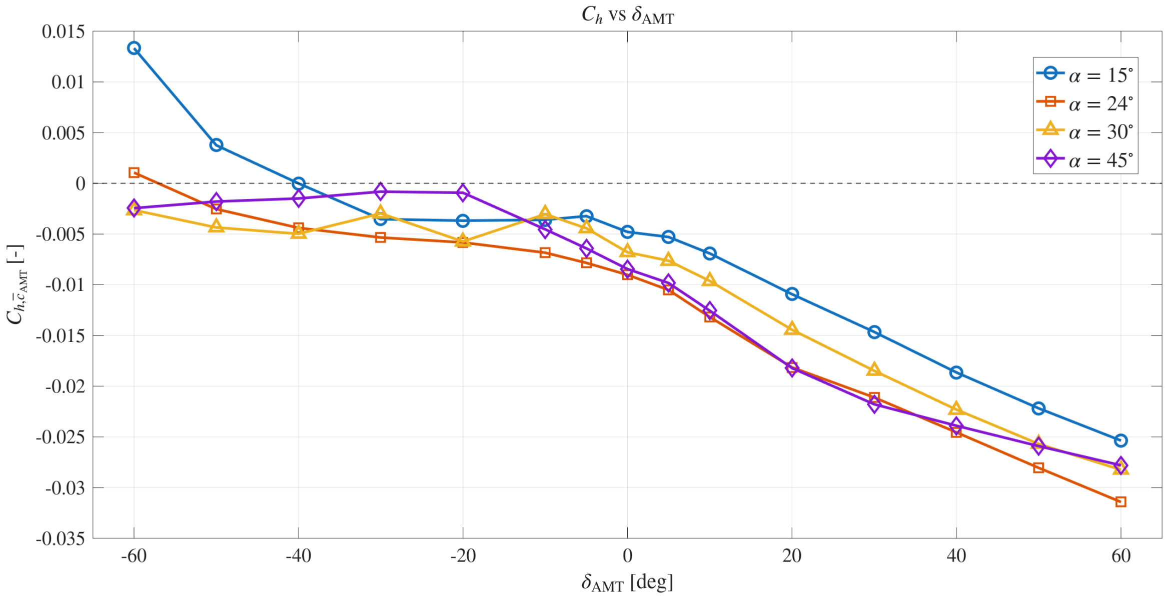

Figure 4.38: Renormalized hinge-moment coefficient as a function of AMT deflection for selected angles of attack.

Figure 4.38 shows the variation of C_h with AMT deflection for four angles of attack, namely $\alpha = 15°$, $24°$, $30°$ and $45°$.

For most of the deflection range, the hinge-moment coefficient is negative, so, in the adopted convention, it tends to rotate the AMT leading edge downward. This indicates that, for most of the deflection range, when the AMT generates a positive lift, the AMT centre of pressure is located downstream of the hinge axis, while when the AMT generates downforce, the AMT centre of pressure is located upstream of the hinge axis.

However, for large negative deflections, especially at $\alpha = 15°$, an inversion of the hinge-moment sign is observed. In this region, C_h becomes positive, indicating that the aerodynamic load tends to rotate the AMT leading edge upward. This sign reversal is associated with the redistribution of the local pressure field over the movable tip and with the change in the relative position between the resultant aerodynamic force and the hinge axis.

The general trend of the curves indicates that, as the AMT deflection increases from negative to positive values, the hinge-moment coefficient becomes progressively more negative. This behaviour is physically consistent with the increase of the aerodynamic loading on the movable tip: larger positive deflections modify the local incidence of the outer wing more strongly, producing a larger pressure imbalance over the AMT and, consequently, a larger aerodynamic torque about the hinge axis.

The curves also show that the hinge-moment response is not linear over the whole deflection range. In the negative-deflection region, approximately between $\delta_{\mathrm{AMT}} = -40°$ and $-20°$, the curves tend to be relatively flat, especially at the larger angles of attack. This suggests that the aerodynamic load acting on the AMT, or its effective moment arm with respect to the hinge axis, is limited in this range.

A clearer and more monotonic behaviour is observed for positive AMT deflections. Starting from $\delta_{\mathrm{AMT}} \simeq 0°$, all curves show an almost linear decrease of C_h with increasing deflection. This indicates that, for positive deflections, the AMT progressively generates a stronger aerodynamic torque about the hinge axis: in this range, the movable tip behaves more regularly.

From an integration point of view, the most relevant quantity for preliminary actuator sizing is not only the sign and behavior of C_h, but mainly the maximum absolute hinge moment over the operational envelope:

$$|M_h|_{\max} = \max\left(|C_h| q_\infty S_{\mathrm{AMT}} \bar{c}_{\mathrm{AMT}}\right).$$

The position of the hinge axis plays a central role in this behaviour. The hinge moment can be interpreted, in first approximation, as the product of the aerodynamic resultant acting on the AMT and its effective lever arm with respect to the hinge axis:

$$M_h \sim F_{\mathrm{AMT}} d_H,$$

where d_H is the distance between the local centre of pressure of the movable tip and the hinge axis. If the hinge axis is located close to the aerodynamic centre of the AMT over the relevant operating range, the resulting hinge moment is reduced. Conversely, if the pressure resultant moves far from the hinge line, the aerodynamic torque increases. The sign reversal observed at large negative deflections can therefore be interpreted as a consequence of a change in the relative position of the resultant aerodynamic force with respect to the hinge axis. This also suggests that future optimization of the AMT concept should not consider only control effectiveness, but also the hinge-axis location, since a suitable hinge placement can reduce actuator requirements without necessarily compromising control authority.

On the basis of the present results, the current hinge-axis location appears to provide an aerodynamically stable behaviour over most of the investigated range, since positive AMT deflections are generally associated with a negative hinge moment, i.e. with a restoring tendency. However, the hinge-moment magnitude increases significantly for positive deflections and for the pre-stall high-lift conditions. A slight aft displacement of the hinge axis could therefore be beneficial, since it would move the rotation axis closer to the average pressure-resultant location associated with the most demanding operating conditions, reducing the aerodynamic torque that must be balanced by the actuator.

Such an aft shift should remain moderate. Moving the hinge axis too far rearwards could overbalance the movable tip, leading to a reduction or even a reversal of the restoring hinge moment in portions of the flight envelope, and this would be undesirable because it could produce a surface that tends to amplify, rather than oppose, the imposed deflection. Therefore, the most suitable hinge-axis location would be slightly aft of the present one, but still ahead of the effective centre of pressure in the main operating range, so as to reduce the actuator torque while preserving a restoring hinge-moment characteristic.

Figure 4.39 shows the variation of C_h with angle of attack for four selected AMT deflections: $\delta_{\mathrm{AMT}} = -30°$, $0°$, $20°$ and $40°$. As expected, the curves are shifted towards larger hinge-moment magnitudes as the AMT deflection increases. In particular, the curves corresponding to positive deflections are characterized by more negative values of C_h, indicating a larger aerodynamic torque acting on the movable tip. This confirms that the actuation demand increases with AMT deflection.

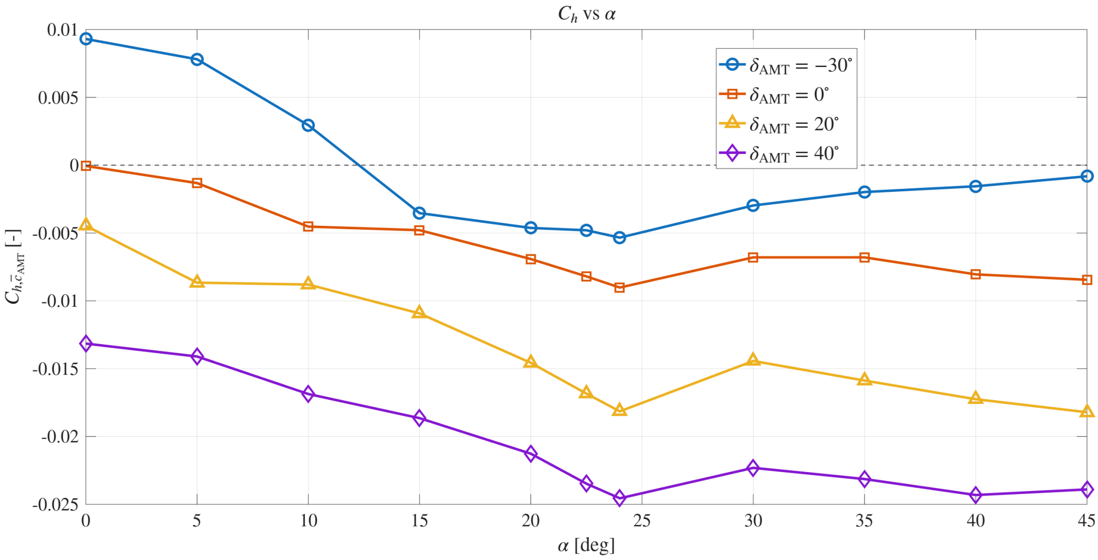

Figure 4.39: Renormalized hinge-moment coefficient as a function of angle of attack for selected AMT deflections.

For the positive-deflection cases ($\delta_{\mathrm{AMT}} = 0°$, $20°$ and $40°$), the hinge moment remains negative over the entire angle-of-attack range. Its magnitude increases from low incidence up to approximately $\alpha = 24°$, where the largest negative value is reached. This condition corresponds to the pre-stall high-lift regime of the wing, where the global aerodynamic loading is close to its maximum. The increase in $|C_h|$ up to this incidence is therefore consistent with the growth of the aerodynamic forces acting on the outer wing and on the movable tip. After this pre-stall peak, a decrease in $|C_h|$ is observed around $\alpha = 30°$, associated with the post-stall redistribution of the pressure field and the reduction of the effective aerodynamic loading on the AMT. This condition is followed by a new tendency to settle on relatively high negative values at larger incidences: the separated and vortical flow structures still maintain a significant aerodynamic torque on the movable surface.

The curve for $\delta_{\mathrm{AMT}} = -30°$ exhibits a distinctive behaviour. At low angles of attack, C_h is positive, meaning that the aerodynamic moment tends to rotate the AMT leading edge upward. As the angle of attack increases, the coefficient decreases and changes sign between $\alpha = 10°$ and $15°$; this transition indicates that the pressure field over the AMT changes significantly with incidence, causing the resultant aerodynamic force to move across the hinge axis. At higher angles of attack, the hinge moment remains slightly negative but its magnitude decreases after the pre-stall region, suggesting a reduction or redistribution of the aerodynamic loading over the movable tip.

The AMT can be advantageous because a balanced all-moving arrangement may reduce hinge-moment requirements, compared for example with drag-based control devices, allowing the surface to be used over a wider flight envelope. Nevertheless, the hinge moment remains a key driver for actuator sizing, structural integration and pivot-shaft design. Consequently, a complete assessment of the AMT concept should combine the control authority analysis with the corresponding hinge-moment demand. The most favorable configuration is not necessarily the one producing the largest control moment, but the one providing the best compromise between generated aerodynamic control and required actuation torque.

4.6 Limitations

4.6.1 Limitations of the numerical model

The numerical campaign presented in this chapter provides a first aerodynamic assessment of the All-Moving Tip (AMT) concept and allows the main trends associated with AMT deflection to be identified. Nevertheless, the results must be interpreted in light of the assumptions and limitations of the numerical model adopted. These limitations do not invalidate the comparative value of the analysis, since the same numerical setup was used consistently for all the simulated cases, but they define the level of confidence and the range of applicability of the conclusions.

A first limitation concerns the geometric representation of the aircraft. The simulations were performed on an isolated semi-wing equipped with an AMT, rather than on a complete aircraft configuration. Therefore, the aerodynamic interaction with the fuselage, forebody, opposite wing, propulsion system, vertical or horizontal tails, and other possible control effectors was not included. This simplification is appropriate for isolating the local aerodynamic contribution of the AMT, but it does not reproduce the complete flow topology of a real fighter aircraft. In particular, the pitching, rolling and yawing moments obtained in the present work depend on the adopted moment reference point and on the simplified layout of the semi-wing. Consequently, the absolute control authority predicted by the simulations should not be interpreted as the final control capability of a complete aircraft, but as the isolated aerodynamic contribution of the selected AMT arrangement.

The use of a semi-wing model also implies a limitation in the representation of lateral-directional effects. The root plane was treated as a symmetry plane, so that the opposite half-wing was not explicitly modelled. As a consequence, the simulations do not directly reproduce a full-aircraft condition with simultaneous or differential deflection of the two AMTs. The rolling and yawing control effectiveness discussed in the previous sections is therefore inferred from the moment generated by one semi-wing and from suitable re-normalization procedures. This approach is useful for a first comparison between different deflections and angles of attack, but it cannot capture possible left-right aerodynamic interactions, asymmetric vortex development, or control-coupling effects that may arise on a complete configuration.

Another limitation is related to the flight condition. All simulations were performed at zero sideslip angle and at a fixed free-stream Mach number. The absence of sideslip allows the effect of incidence and AMT deflection to be isolated, but it prevents the direct evaluation of directional stability derivatives and of the AMT response in asymmetric incoming-flow conditions. This is particularly relevant at high angle of attack, where small sideslip perturbations may strongly affect the position, strength and breakdown of vortical structures. Moreover, the fixed Mach-number condition does not allow the Mach sensitivity of the AMT to be assessed. Since the project is motivated by high-speed aircraft applications, the present results should be considered as a subsonic reference assessment. A complete characterization of the AMT concept would require additional simulations in transonic and supersonic regimes, where shock waves, expansion waves, shock-induced separation and wave drag may significantly modify the control effectiveness and the hinge-moment demand.

The AMT was also treated as a fixed geometry for each prescribed deflection angle. The simulations therefore reproduce the steady aerodynamic loads associated with a given AMT position, but not the transient motion of the movable tip. As a result, the present model does not include deflection-rate effects, actuator dynamics, control-surface acceleration, dynamic hinge moments or possible aeroelastic interaction during the motion. The hinge moment evaluated in this work is therefore an aerodynamic holding moment for a fixed deflection, not a complete actuator-sizing load case. In a real application, actuator sizing would also require inertial loads, dynamic aerodynamic loads, structural margins, rate requirements and failure-case considerations.

The geometry of the AMT was idealized. The movable tip was modelled as a rigid surface with a prescribed angular position, without representing hinge gaps, seals, actuator fairings, structural clearances or local manufacturing details. These features may affect the local pressure distribution, the hinge-moment characteristics and the radar-signature compatibility of the concept. Moreover, the wing and AMT were assumed to be rigid, so aeroelastic effects were not considered. For a thin, highly swept wing, structural deformation could modify the local incidence, twist distribution and AMT alignment, leading to changes in both aerodynamic loads and control effectiveness.

The turbulence modelling strategy represents a further source of uncertainty. The computations were performed using a steady Reynolds-Averaged Navier–Stokes approach with the SST $(k-\omega)$ turbulence model. This choice provides a reasonable compromise between computational cost and aerodynamic fidelity for a parametric study, but it cannot fully resolve the unsteady features that are typical of separated and vortex-dominated flows. At moderate and high angles of attack, swept low-aspect-ratio wings may exhibit vortex wandering, vortex breakdown, shear-layer instabilities, buffet-like oscillations and hysteresis effects. In a steady RANS simulation, these phenomena are represented only through a time-averaged solution and through the turbulence closure model. Therefore, the computed aerodynamic coefficients should be interpreted mainly as mean-load estimates, while the detailed unsteady evolution of the vortex system is not captured.

This aspect is especially important for the highest angles of attack investigated. In this range, the flow field is strongly separated and the aerodynamic loads can become sensitive to small changes in mesh resolution, numerical schemes, convergence criteria and initial conditions. The steady solution may converge to an averaged state that is useful for identifying global trends, but it may not represent the instantaneous aerodynamic loads experienced by a real aircraft. For this reason, phenomena such as unsteady rolling or yawing moments, dynamic stall, vortex-induced load oscillations and buffet cannot be assessed with the present model. A more detailed investigation would require unsteady RANS simulations or higher-fidelity scale-resolving approaches, such as Detached Eddy Simulation or Large Eddy Simulation.

The mesh resolution represents another limitation of the present numerical campaign. The mesh was generated with local refinements around the wing, the AMT, the hinge region and the wake, but the total number of cells was constrained by the computational resources and by the maximum size allowed by the available ANSYS Fluent Student license: about a million cells, which for a 3D flow simulation is a rather limited number. Consequently, a formal grid-convergence study was not performed. The same meshing strategy was used for all configurations, which supports the relative comparison among the different AMT deflections, but the absolute values of the aerodynamic coefficients may still be affected by discretization error. This is particularly relevant for the prediction of drag, hinge moment, separated-flow regions and local pressure peaks near the leading edge, tip and hinge line.

The near-wall resolution should also be considered when interpreting the results. The inflation layers were introduced to improve the description of the viscous region close to the solid surfaces, but the boundary-layer resolution was limited by the global mesh-size constraint. Since separation, reattachment, wall shear stress and pressure recovery strongly depend on the near-wall treatment, local quantities such as the separated-flow footprint and the hinge-moment coefficient may be more sensitive to mesh resolution than the global lift and moment trends. A higher-fidelity campaign would require a systematic assessment of wall resolution, near-wall modelling and grid sensitivity.

4.6.2 Limitations of the results comparison

No experimental validation was available for the specific AMT configuration analysed in this work. The numerical results were checked in terms of residual behaviour and stabilization of aerodynamic coefficient histories, but this procedure represents a convergence assessment rather than a validation against physical data. Wind-tunnel tests or higher-fidelity numerical simulations would be required to quantify the predictive accuracy of the model, especially in the nonlinear high-angle-of-attack range.

The comparison with reference fighter configurations must be interpreted with caution. The F-16, F/A-18 and X-29 data used for comparison refer to different aircraft, control surfaces, reference geometries, flow conditions and experimental or flight-test contexts. Re-normalization allows the order of magnitude of the AMT control authority to be compared with conventional or experimental effectors, but it does not remove all configuration-dependent effects. Therefore, these comparisons are useful to understand whether the AMT produces a small, moderate or large control contribution, but they should not be interpreted as a direct replacement assessment between different aircraft control architectures.

In summary, the present CFD model should be regarded as a preliminary, steady, isolated-surface assessment of the AMT concept. Its main strength is the consistent parametric comparison between different AMT deflections and angles of attack, which allows the dominant aerodynamic trends and control-coupling mechanisms to be identified. Its main limitations are associated with the isolated semi-wing geometry, the steady RANS formulation, the fixed subsonic Mach number, the absence of sideslip and dynamic effects, the mesh-size constraint and the lack of experimental validation. Future work should therefore include grid- and domain-independence studies, unsteady simulations, Mach- and Reynolds-number sensitivity analyses, full-aircraft modelling, differential AMT deflections, aeroelastic effects and experimental validation. These additional steps would be necessary to move from the present conceptual assessment toward a complete evaluation of the AMT as a practical control effector for advanced high-speed fighter configurations.

Conclusions

The present thesis investigated the aerodynamic potential of innovative control effectors for future high-speed fighter aircraft, with specific focus on the All-Moving Tip (AMT) concept. The work was motivated by one of the central design challenges of advanced combat aircraft: preserving manoeuvrability and control authority while reducing the aerodynamic and low-observability penalties associated with conventional tails and large hinged control surfaces.

The preliminary part of the thesis showed that this problem becomes particularly demanding at high angles of attack, where the aerodynamic response is governed by separation, leading-edge vortices, vortex breakdown and strong lateral-directional coupling. In this regime, conventional control surfaces may lose effectiveness because they operate in separated or highly distorted flow regions. This makes non-conventional aerodynamic effectors and active/passive flow-control solutions a relevant design option for future aircraft architectures.

Within this framework, the AMT was selected as a compact wing-tip control effector capable of modifying the local aerodynamic loading at the outer portion of the wing. The solution validation was carried out through a CFD campaign on a highly swept and low aspect-ratio semi-wing, equipped with a movable tip, considering different angles of attack and AMT deflections. The purpose was to isolate the aerodynamic contribution of the AMT and assess whether this device can generate meaningful force and moment increments.

The AMT does not radically alter the global lift behaviour of the wing, because it occupies only a limited portion of the planform. However, its effect is systematic and measurable. By changing the local incidence of the outer wing tip, the AMT modifies the pressure distribution and the aerodynamic loading in a region characterized by strong three-dimensional effects, tip-vortex interaction and increasing separation sensitivity. This confirms that the AMT acts primarily as a local load control device.

From the drag point of view, AMT deflection introduces a limited but clear aerodynamic penalty: larger deflections increase the local loading and pressure drag at the movable tip. This result is consistent with the physical role of the AMT: it generates control moments through a controlled redistribution of loads at the wing tip.

The yaw-control analysis showed that the AMT produces a consistent and progressive control response. In comparison with conventional rudders, the AMT control authority is lower for moderate deflections and angles of attack, but continues to grow over a larger deflection range, whereas conventional rudders are normally limited by separation and saturation effects at high deflection.
Unlike conventional rudders, which are designed to generate lift on the vertical tail, the AMT yaw-control mechanism acts mainly by increasing the aerodynamic drag asymmetry between the two semi-wings. The AMT can therefore operate at much larger deflections and angles of attack, because it does not rely on maintaining an attached flow on the control surface, but rather can exploit the separated flow condition itself to increase the asymmetric drag contribution. The AMT is therefore able to preserve, and even enhance, its yaw-control effectiveness in conditions where conventional rudders tend to lose efficiency: high deflections and high angles of attack regimes. This indicates that the AMT may be promising as an auxiliary or complementary yaw control effector, particularly in configurations where vertical surfaces are reduced, eliminated, or are losing effectiveness.

The roll-control analysis confirmed the natural suitability of the AMT for lateral control, as the aerodynamic loads generated at the wing tip act with a large spanwise lever arm with respect to the aircraft centreline. When the two wing tips are deflected asymmetrically, the negative-deflection branch is generally more effective than the positive one, because it is less affected by premature local stall of the tip surface. However, the AMT loses part of its incremental authority at large rotations, most likely because the local flow approaches a saturated or partially separated condition.
One of the main advantages of the AMT concept, especially at high angles of attack, is to exploit the device as an all-moving surface, scheduling its deflection as a function of incidence and deflection sign, in order to exploit the most favorable aerodynamic branch while avoiding ineffective or saturated operating conditions.

The pitch-control analysis confirmed that the AMT is naturally more suited to lateral-directional control than to longitudinal control. The comparison with conventional and experimental pitch-control effectors showed that the AMT generates a much smaller pitching-moment increment. This is not primarily caused by a lack of local aerodynamic loading, but by the geometry of the installation: the AMT is located far outboard and has a short longitudinal lever arm with respect to the pitch axis. The trim analysis confirmed that, for the centre of gravity position and moment reference point adopted in the present numerical model, the configuration can be trimmed only in a very narrow range of angles of attack close to zero incidence, and large positive AMT deflections introduce a considerable drag penalty without producing a meaningful extension of the pitch-trim envelope. Therefore, in the analysed layout, the AMT should be regarded only as a secondary pitch-control contributor, while its main aerodynamic value remains in the lateral-directional control domain.

The hinge-moment analysis added an important design constraint. The aerodynamic torque required to hold the AMT increases with deflection and reaches its largest values near the pre-stall high-lift regime, where the aerodynamic loading of the wing is strongest. A slight aft displacement of the hinge axis could therefore be beneficial, since it would move the rotation axis closer to the average pressure resultant location associated with the most demanding operating conditions. However, a practical design must also account for actuator sizing, hinge-axis placement, structural integration and aeroelastic effects.

Overall, the results show that the AMT is a promising control effector. With its outboard location and its multi-axis nature, the most relevant contribution is in the lateral-directional domain, where it can provide additional roll and yaw authority while preserving a compact geometry and wing-integrated architecture. This makes the AMT particularly interesting for advanced low-observable configurations, provided that it is used together with other effectors as part of a broader control allocation strategy.

Future developments

The conclusions must be interpreted in light of the limitations of the numerical model and of the results comparison. Effects such as full-aircraft interference, differential left-right vortex interaction, unsteady vortex breakdown, dynamic control-surface motion, aeroelastic deformation, transonic and supersonic phenomena, and experimental uncertainty were not included.

Future work should therefore focus on extending the analysis toward a complete aircraft-level assessment. The first step should be a numerical verification campaign, including a mesh refinement exploiting more powerful computing resources, grid- and domain-independence studies. The second step should include Mach-number sensitivity, sideslip conditions, unsteady simulations, and dynamic AMT deflection. A full-aircraft model would then be required to evaluate the real contribution of the AMT to trim, stability, control allocation and manoeuvrability. Finally, the AMT geometry should be optimized in terms of spanwise extension, planform area, hinge-axis location and deflection law, with simultaneous consideration of control authority, hinge moment, drag penalty, structural integration and low-observability constraints.

In conclusion, the AMT concept demonstrates a clear aerodynamic capability to modify the local wing-tip loading and generate useful lateral-directional control moments. Its main strength is the possibility of providing compact, wing-integrated, multi-axis control authority compatible with advanced low-observable layouts. The present configuration shows that the AMT should be considered a complementary effector, not a standalone solution. Its effective application to future fighter aircraft will depend on its integration within a coordinated control-effector suite and on the ability to exploit its lateral-directional benefits while mitigating its pitch-control limitations, drag penalty and actuation requirements.

Bibliography

[1] Kim, Chongsup, Giok Koh, Nagsun Choi, and Gi-Bong Hur. "Control Technologies for Tailless Configurations in Sixth-Generation Fighter Aircraft." *International Journal of Aeronautical and Space Sciences*, vol. 27, 2026, pp. 1660–1704. `https://doi.org/10.1007/s42405-025-01059-6`.

[2] NATO Science and Technology Organization. *Innovative Control Effectors for Manoeuvring Air Vehicles.* NATO AVT-239-RTG-082 Technical Activity Proposal, NATO Science and Technology Organization, 2013.

[3] How, Jonathan P. "Aircraft Dynamics." *16.333 Aircraft Stability and Control*, Lecture 4, Massachusetts Institute of Technology, MIT OpenCourseWare, Fall 2004. `https://ocw.mit.edu/courses/16-333-aircraft-stability-and-control-fall-2004/resources/lecture_4/`.

[4] Boys, Stewart, and Walter Wagtendonk. *CPL Principles of Flight and Performance: A Waypoints Aviation PilotBooks Training Manual.* Commercial Pilot Series, vol. 7, revised ed., Waypoints Aviation Ltd., 2011.

[5] Bertin, John J., and Russell M. Cummings. *Aerodynamics for Engineers.* 6th ed., Cambridge University Press, 2022. `https://doi.org/10.1017/9781009105842`.

[6] Gudmundsson, Snorri. *General Aviation Aircraft Design: Applied Methods and Procedures.* 2nd ed., Butterworth-Heinemann, Elsevier, 2022. ISBN: 978-0-12-818465-3.

[7] Ray, Edward J., Linwood W. McKinney, and Julian G. Carmichael. *Maneuver and Buffet Characteristics of Fighter Aircraft.* NASA Technical Note NASA-TN-D-7131, National Aeronautics and Space Administration, July 1973. `https://ntrs.nasa.gov/api/citations/19730017272/downloads/19730017272.pdf`.

[8] Busquet, Denis. *Study of a High Reynolds Number Flow around a Two-Dimensional Airfoil at Stall: An Approach Coupling a RANS Framework and Bifurcation Theory.* Ph.D. thesis, Institut Polytechnique de Paris, 2020. HAL, `https://hal.science/tel-02971622`.

[9] Polhamus, Edward C. "Predictions of Vortex-Lift Characteristics by a Leading-Edge Suction Analogy." *Journal of Aircraft*, vol. 8, no. 4, 1971, pp. 193–199. `https://doi.org/10.2514/3.44254`.

[10] Rom, Josef. *High Angle of Attack Aerodynamics: Subsonic, Transonic, and Supersonic Flows.* Springer Science & Business Media, 2012.

[11] Advisory Group for Aerospace Research and Development. *High Angle-of-Attack Aerodynamics.* AGARD Lecture Series No. 121, North Atlantic Treaty Organization, AGARD, 1982. ISBN: 92-835-0322-8.

[12] Esfandabadi, Mohammad Hossein Moghimi, Hani Attar, Kamyab Karbasishargh, Mohammad Hasan Javareshakian, Seyed Vahid Ghasemi, and Mohammad Mahdi Moghimi. "A Review of Passive Control Flow Past UAV Wings." *2023 2nd International Engineering Conference on Electrical, Energy, and Artificial Intelligence (EICEEAI)*, IEEE, 2023, pp. 1–5. `https://doi.org/10.1109/EICEEAI60672.2023.10590150`.

[13] Juliet, Victor. "How Does the Use of Leading Edge Root Extension Help in Increasing Stall Angle?" *Aviation Stack Exchange*, Stack Exchange, 10 June 2015, `https://aviation.stackexchange.com/questions/15637/how-does-the-use-of-leading-edge-root-extension-help-in-increasing-stall-angle`. Accessed 15 June 2026.

[14] Harris, Jeffrey J., and G. Thomas Black. "F-22 Control Law Development and Flying Qualities." *21st Atmospheric Flight Mechanics Conference*, American Institute of Aeronautics and Astronautics, 1996. `https://doi.org/10.2514/6.1996-3379`.

[15] Nguyen, Luat T., Marilyn E. Ogburn, William P. Gilbert, Kemper S. Kibler, Phillip W. Brown, and Perry L. Deal. *Simulator Study of Stall/Post-Stall Characteristics of a Fighter Airplane with Relaxed Longitudinal Static Stability.* NASA Technical Paper NASA-TP-1538, National Aeronautics and Space Administration, Dec. 1979.

[16] Iliff, Kenneth W., and Kon-Sheng Charles Wang. *Extraction of Lateral-Directional Stability and Control Derivatives for the Basic F-18 Aircraft at High Angles of Attack.* NASA Technical Memorandum NASA-TM-4786, National Aeronautics and Space Administration, Feb. 1997.

[17] K. W. Iliff and K.-S. C. Wang, *X-29A Lateral-Directional Stability and Control Derivatives Extracted from High-Angle-of-Attack Flight Data.* NASA Technical Paper NASA-TP-3664, 1996.

[18] K. W. Iliff and K.-S. C. Wang, *Flight-Determined Subsonic Longitudinal Stability and Control Derivatives of the F-18 High Angle of Attack Research Vehicle (HARV) with Thrust Vectoring.* NASA Technical Paper NASA/TP-97-206539, 1997.

[19] Chakraborty, Manash. *A Computational Study on Two Horizontally Close Sequential Airfoils to Determine Conjoined Pressure Distribution and Aerodynamic Influences on Each Other.* B.Sc. Engineering thesis, Department of Mechanical Engineering, Chittagong University of Engineering and Technology, 2015. ResearchGate, `https://www.researchgate.net/figure/Schematic-of-X-29-high-speed-aircraft-Courtesy-of-Grumman-Aircraft-Manufacturing_fig1_281824169`. Accessed 15 June 2026.

[20] Budd, Gerald D. *Predicted Pitching Moment Characteristics of X-29A Aircraft.* NASA Technical Memorandum NASA-TM-88284, National Aeronautics and Space Administration, Mar. 1987. `https://ntrs.nasa.gov/citations/19890009047`.

[21] K. M. Dorsett and D. R. Mehl, *Innovative Control Effectors (ICE)*, Wright Laboratory Technical Report WL-TR-96-3043, Wright-Patterson Air Force Base, OH, 1996.

[22] W. J. Gillard and K. M. Dorsett, "Directional Control for Tailless Aircraft Using All-Moving Wing Tips," in *Proceedings of the AIAA Atmospheric Flight Mechanics Conference*, New Orleans, LA, 1997. AIAA Paper 97-3487. doi: 10.2514/6.1997-3487.